LEAST SQUARES INVERSION OF FIELD SEISMIC DATA FOR AN ELASTIC 1-D EARTH

APPROVED BY
DISSERTATION COMMITTEE:

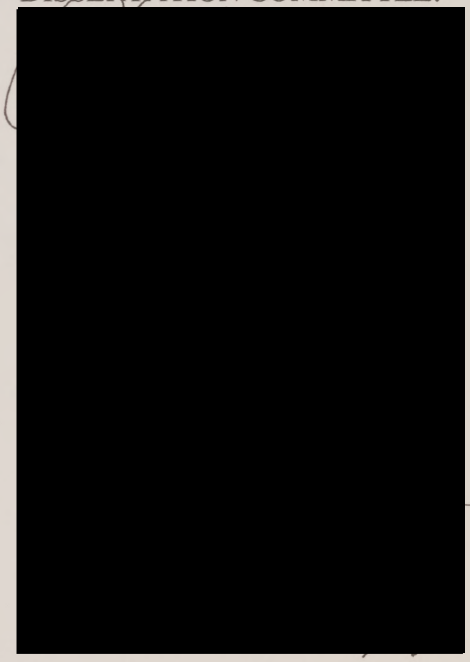

For my family

LEAST SQUARES INVERSION OF FIELD SEISMIC DATA FOR AN ELASTIC 1-D EARTH

by

WARREN THEODORE WOOD, B.S., M.A.

DISSERTATION

Presented to the Faculty of the Graduate School of
The University of Texas at Austin
in Partial Fulfillment
of the Requirements
for the Degree of
DOCTOR OF PHILOSOPHY

THE UNIVERSITY OF TEXAS AT AUSTIN
May 1993

ACKNOWLEDGMENTS

I wish to thank my advisor, Dr. Paul Stoffa for seeing me through this work and having confidence in my ability to complete it. Dr. Mrinal Sen was also very helpful at all stages of my research as was Dr. Milo Backus whose advice and guidance were invaluable. I also wish to thank the research and support staff of the University of Texas Institute of Geophysics who were very helpful in all aspects of my stay at The University of Texas. My research was funded in part by the National Science Foundation grants Number OCE-86-137743 and OCE-9000327, Sea grant A/E545NA89AA-D-56139, by the AMOCO foundation, and by the Phillips Petroleum Foundation Inc.

LEAST SQUARES INVERSION OF FIELD SEISMIC DATA

FOR AN ELASTIC 1-D EARTH

Publication No. _____

Warren Theodore Wood, Ph.D.

The University of Texas at Austin, 1993

Supervisor: Paul L. Stoffa

Elastic 1-D inversion of seismic reflection data is successfully applied to common midpoint field data of varying offset ranges. The inversion, actually iterative forward modeling, operates on plane wave seismic data and yields P-wave velocity, (V_p), density, and S-wave velocity, (V_s) for each of many (typically hundreds) equal time thickness layers. The problem is viewed in terms of a multi-dimensional optimization problem where the error function is defined as the square of model and data misfit. The error is minimized by the Newton method which requires slope (sensitivity of each datum to each model parameter) and curvature (full Hessian) of the error function at each of several iterations. The algorithm is tested on realistic synthetic data, and when applied to conventional common midpoint data is very helpful in determining the nature of a bottom simulating reflector in the Carolina Trough off shore South Carolina. The algorithm is also applied to deep water data acquired in the Nankai Trough offshore Japan as part of a tectonic study of the accretionary prism. Here the waveform inversion results from 8 very wide aperture expanding spread profiles (ESPs), and 610 conventionally acquired common midpoint gathers are used to generate sediment property cross sections across the accretionary wedge deformation front, highlighting the vertical and lateral sediment property changes.

Table of Contents

Chapter 1
Advantages of Full Waveform Inversion

Introduction

The successful application of least squares inversion of seismic waveform data dramatically improves the resolution of sediment properties obtained by the laterally extensive, non-invasive, seismic reflection technique. Since seismic waves are elastic waves, they are affected by changes in the elastic parameters of the earth, and can therefore be used to obtain estimates of these parameters. Previously, much of this information has been used only qualitatively due to the difficulty in extracting it, and the ambiguity in the final result. In this study I show how quantitative estimates of elastic parameters can be objectively obtained from reflection seismic data, effectively extracting all the information available from the data subject to prior constraints.

In particular three types of data are analyzed with this method, a very high quality, conventional common midpoint (CMP) gather acquired in the Carolina Trough off the eastern U.S., a set of wide aperture two ship expanding spread profiles (ESPs) acquired in the Nankai Trough off southern Japan, and conventional, although small aperture CMPs also collected in the Nankai Trough. The goal of inverting the Carolina Trough data is to determining with the highest possible resolution the nature of the bottom simulating reflector (BSR) in this area. The BSR is caused by high velocity methane hydrate above the reflecting interface and non methane hydrated sediment below. Accurate elastic parameter profiles enable quantitative estimates of how much, and in what form methane may be present. The goals of the inversion of the Nankai Trough data include using very high resolution profiles to infer such properties as porosity and shear strength at key locations within the toe of the accretionary wedge. The small aperture CMP data is used to examine the areas between the ESP sites creating a sediment property cross section across the toe of the wedge.

The Role of Seismic Data

Reflection seismology complements drilling or direct sampling by providing information on the large scale sub-surface structural geometry and the sediment physical properties. However, it's full potential has not been reached. In the past the use of seismic data has been limited almost exclusively to producing a subsurface image and providing a background trend for the compressional wave, i.e. P-wave velocity. I define the background trend here as variations of ~5 or fewer cycles in 1.0 s of P-wave travel time, or 5 Hz. More recently Aoki et al. (1986), and Moore et al. (1990) have gone beyond imaging in the Nankai Trough and used the polarity of the seismic wavelet to infer local sediment properties, and Hyndman and Spence (1992) have even performed amplitude vs. offset analyses on data from the Cascadia margin. Some authors have used strictly linear, single iterate methods, (e.g. Smith and Gidlow, 1987) however, little use has been made of iterative full waveform inversion (McAulay, 1985, 1986; Amundsen and Ursin, 1989; Tarantola, 1987; Mora, 1988 and others) on field data anywhere to quantitatively extract all available sediment property information from the data.

The role of seismic data as related to other data sources is shown diagrammatically in Figure 1.1. At the left is depicted the method of measurement and at the right is the information desired. At the top is the direct, *in situ* data followed in order of decreasing resolution by direct, remotely collected data, and finally the indirect data, i.e. inferences from laboratory models and other, geologically similar areas. Solid and hollow arrows represent direct and empirical or heuristic relationships respectively. Sparse but high resolution well data (samples and logs) are used with the areally extensive but lower resolution seismic data to infer geologic conditions but these analyses are qualitative. Analysis of the seismic data through waveform inversion can potentially result in sediment parameter cross sections with resolution approaching that of the well data but with dense, areally extensive coverage.

These cross sections are composed of inversion results from one gather at a time. For each seismic gather analyzed, the earth is assumed to be a stack of locally 1-D homogeneous, isotropic layers each with independently varying elastic parameters. Given this there are 3 independent elastic parameters for each layer. For

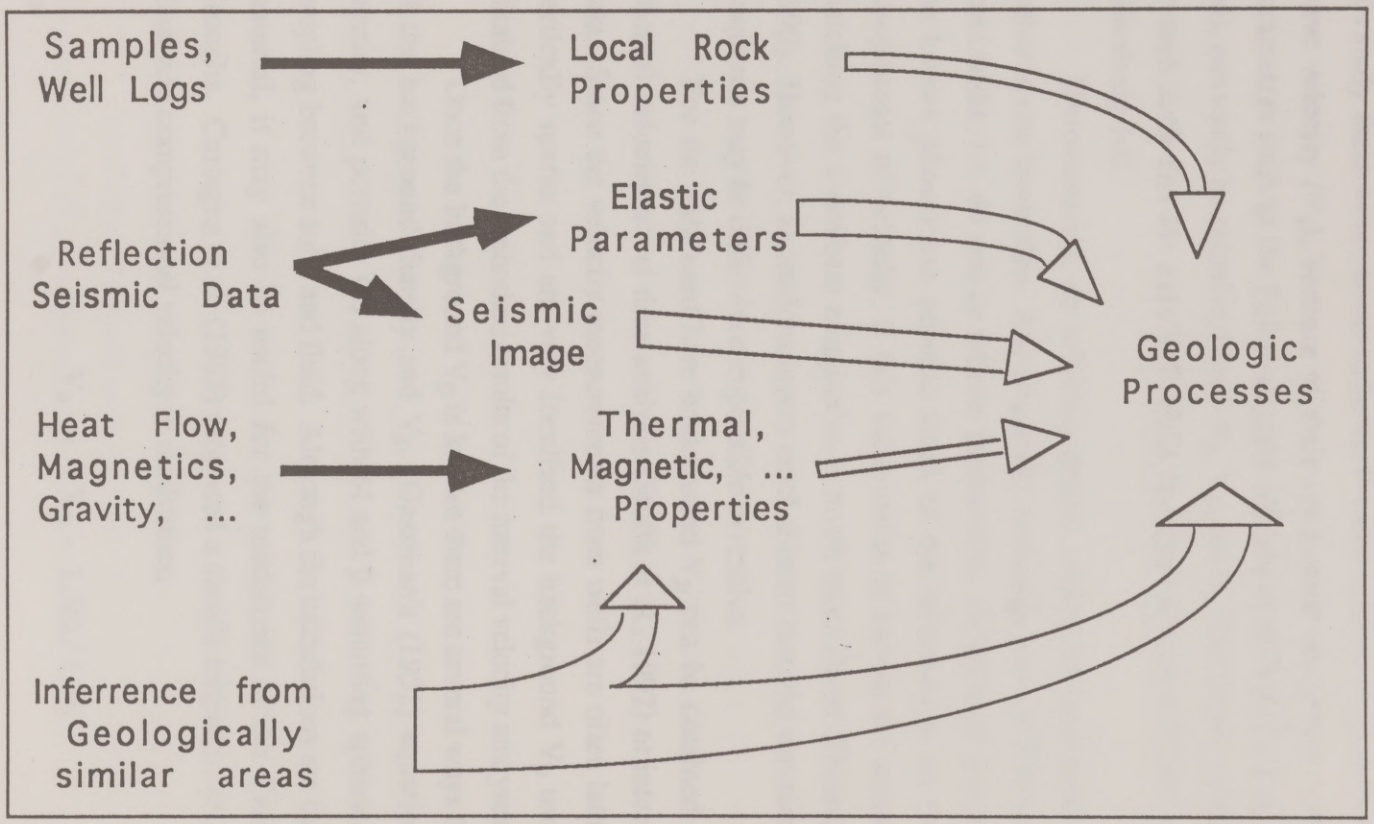

Figure 1.1. Data collected (left) is analyzed and interpreted to yield desired information (Geologic processes). High resolution data (upper paths) tend to be sparse while areally extensive data (lower paths) tend to have low resolution. Seismic data is areally extensive like other forms of non invasive measurement, but also has the potential for much higher resolution.

this study these were chosen to be the P-wave velocity (V_p), bulk density (ρ), and S-wave velocity (V_s), because of their conceptual simplicity. Other useful elastic parameters such as the Poisson's ratio (σ), shear modulus (μ), or the bulk modulus (M), can easily be calculated from V_p, V_s, and ρ. The lateral variability must be mild enough such that for each individual common midpoint (CMP) gather the earth is effectively 1-D.

Unfortunately, an arbitrary model cannot be recovered from the seismic gather in one linear step. Any physically realizable wave will have a finite frequency band width, i.e. no zero or infinite frequencies. Analysis of just the arrival times of the known phases can provide much of the information on the slowly varying components of velocity. If this information is known the remaining problem of matching the waveform amplitudes is much more linear (Dietrich and Kormendi, 1990). However, anomalous layers much thinner than the wavelength of the highest frequency may be difficult or impossible to resolve.

For the data used here background V_p can be obtained either through an interval velocity travel time analysis (Stoffa et al., 1992) or interpolated from well data. Since the velocity measurements from wells are often laterally and perhaps vertically sparse and are very localized the background V_p used in this study is obtained from the smoothed results of the interval velocity analyses.

Once the background V_p is known there are several ways to obtain estimates of the background density and V_s. Gassman's (1951) equation relates V_p, V_s, density, and porosity (ϕ) along with M and μ assuming spherical pores and firm coupling between solid and fluid. Although the calculations are based on a sand like material, it may also be useful for the mudstones of the Carolina and Nankai Troughs. Castagna et al. (1985) proposed a simple empirical relationship between shear and compressional velocity in mudstones;

$$V_s = (V_p - 1.36) / 1.16$$

where the velocities are in km/s. Castagna et al. (1985) and Han et al. (1986) have both experimented with the relation between V_p, V_s, ϕ, and clay content. Other options include regional averages of ρ or V_s vs. depth or travel time for a given

lithology (Hamilton, 1976), the V_p vs. ρ relation of Gardner et al. (1974), or interpolation from nearby well data.

Since seismic data are effectively insensitive to background density, the density trend in the Carolina and Nankai Trough areas was interpolated and extrapolated from nearby DSDP (Deep Sea Drilling Project) and ODP (Ocean Drilling Program) sites to the depths of these wells. Beyond this depth the density is assumed to parallel the curve of Hamilton (1976) down to ~ 1 km, at which point it is made to linearly approach and remain at the grain density by ~2.0 km. Since much of the rock in both of these areas is mudstone, the background V_s is taken directly from the background V_p and the mudrock line of Castagna (1985).

Once the smooth, low frequency model is found the inversion algorithm can generate the high frequency layer to layer changes in each of these parameters which produces the best least squares fit to the data. Knowledge of the final model (low and high frequencies) can then used to map changes in a variety of physical properties including ϕ, μ, σ, and M (Smith and Gidlow, 1987)

Combined with grain (ρ_g) and pore fluid (ρ_f), and bulk densities, porosity estimates can be made using the relation

$$\rho = (1 - \phi)\rho_g + \phi\rho_f \qquad \text{or} \qquad \phi = (\rho_g - \rho) / (\rho_g - \rho_f).$$

The time average equation of Wyllie et al. (1956) can also be used to relate V_p, ϕ, matrix velocity (V_{pm}), and fluid velocity (V_{pf}) by

$$1 / V_p = (1- \phi) / V_{pm} + \phi / V_{pf}$$

with the disadvantage that V_{pm} and V_{pf} must be previously known.

Knowledge of high frequency ρ and V_s is also useful since it can be used to obtain estimates of the sediment shear modulus μ through the defining relation

$$\mu = \rho V_s^2$$

Reasons for using the fully elastic waveform inversion instead of simpler schemes include accurate modeling of interbed multiples and mode converted waves. Ignoring these phenomena may degrade the inversion result.

Applications to Three Disparate Types of Field Data

Least squares linear inversion can be performed on data acquired by very different means. The technique is first demonstrated on very high quality conventionally acquired CMP data from the Blake Ridge area off the eastern U.S. coast, (Figure 1.2). The data were acquired by the *M.V. Geco My* under contract from the University of Texas. The streamer, towed at a depth of 0.0145 km, was 6.0 km in length with a near offset of 0.275 km and recorded 240 channels of data for 16.0 s at a 0.004 s sample rate. The data were filtered with a high cut of 64 Hz falling off at 72 db/octave, and a low cut of 5.3 Hz falling off at 18 db/octave. Shots were fired every 0.05 km based on Starfix navigation supplemented with global positioning system (GPS) satellites and Loran C. The source array consisted of six subarrays of six Bolt 1500 C airguns each towed at a depth of 0.0075 ± 0.001 km, with a total volume of 177 liters.

In this area a bottom simulating reflector (BSR) caused by methane hydrate lies about 0.45 km below the sea floor. The exact nature of this strong, reversed polarity reflection is important in quantitatively determining the amount of methane present in the shallow sediments. Waveform inversion of CMP data is required to obtain the highest resolution possible from these seismic data.

As mentioned earlier knowledge of the background velocity makes possible the linear or near linear inversion for the higher frequency model variations. The background Vp was obtained for the Carolina Trough data and are used to apply a normal move-out (NMO) correction to the data shown in Figure 1.3. If V_p is accurate all precritical, primary, V_p, reflection events (for a 1-D earth) will be made flat and horizontal. McAulay (1985) showed that to some extent the low frequencies can be recovered through the waveform inversion.

The inversion discussed in this study is also performed on wide aperture reflection seismic data. In 1987, a program sponsored by NSF grant no. OCE 86-13774 collected 250 km of multi-channel seismic (MCS) lines, 7 two ship expanding

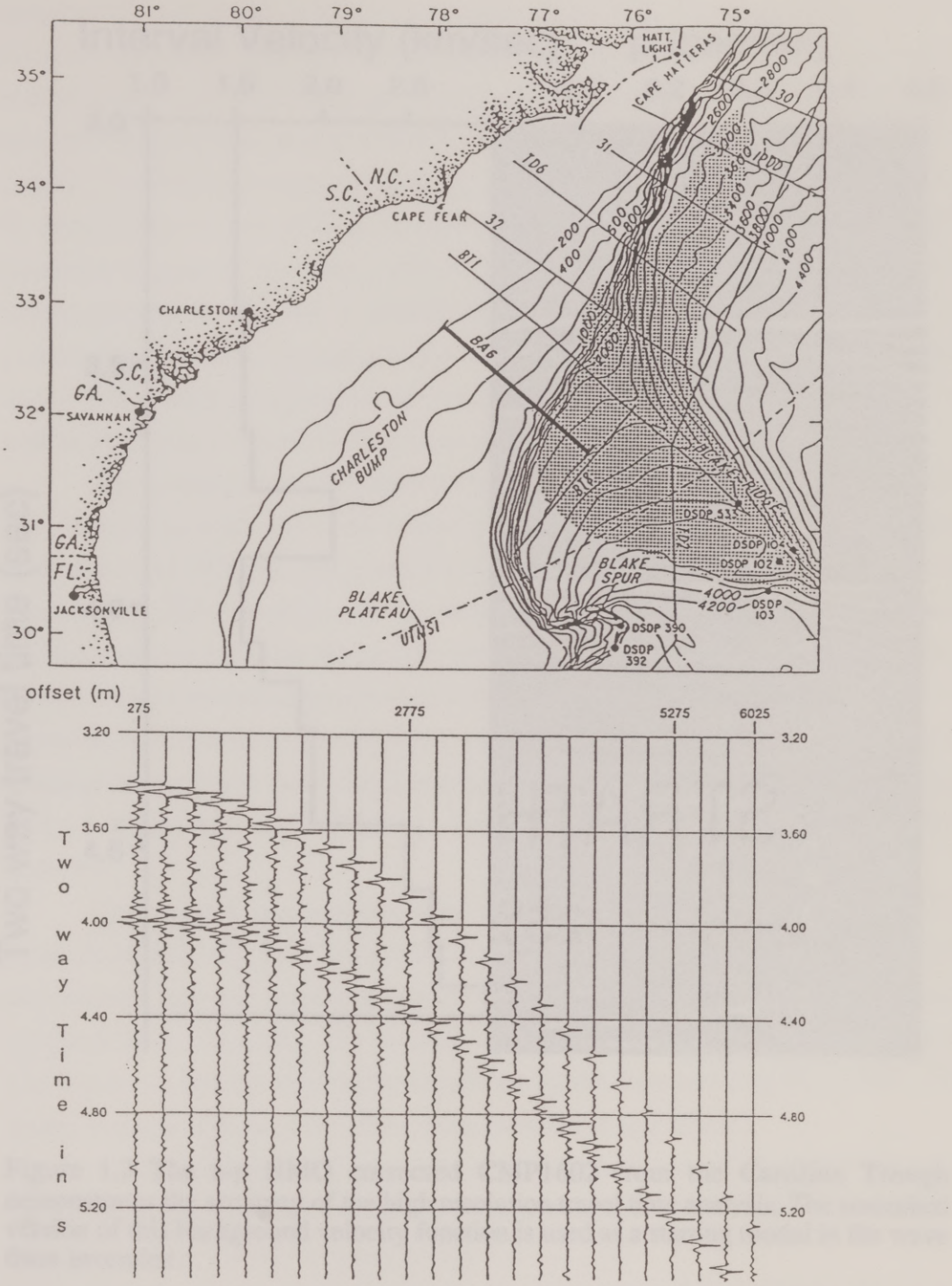

Figure 1.2. The deeper portion of line BA6 (upper,bold) was acquired in an area of the Blake ridge where methane hydrates are known to exist, (stippled). CMP1602 (lower) shows the promeinent water bottom refelction (3.44 s at near offset) and the BSR (4.0 s at near offset).

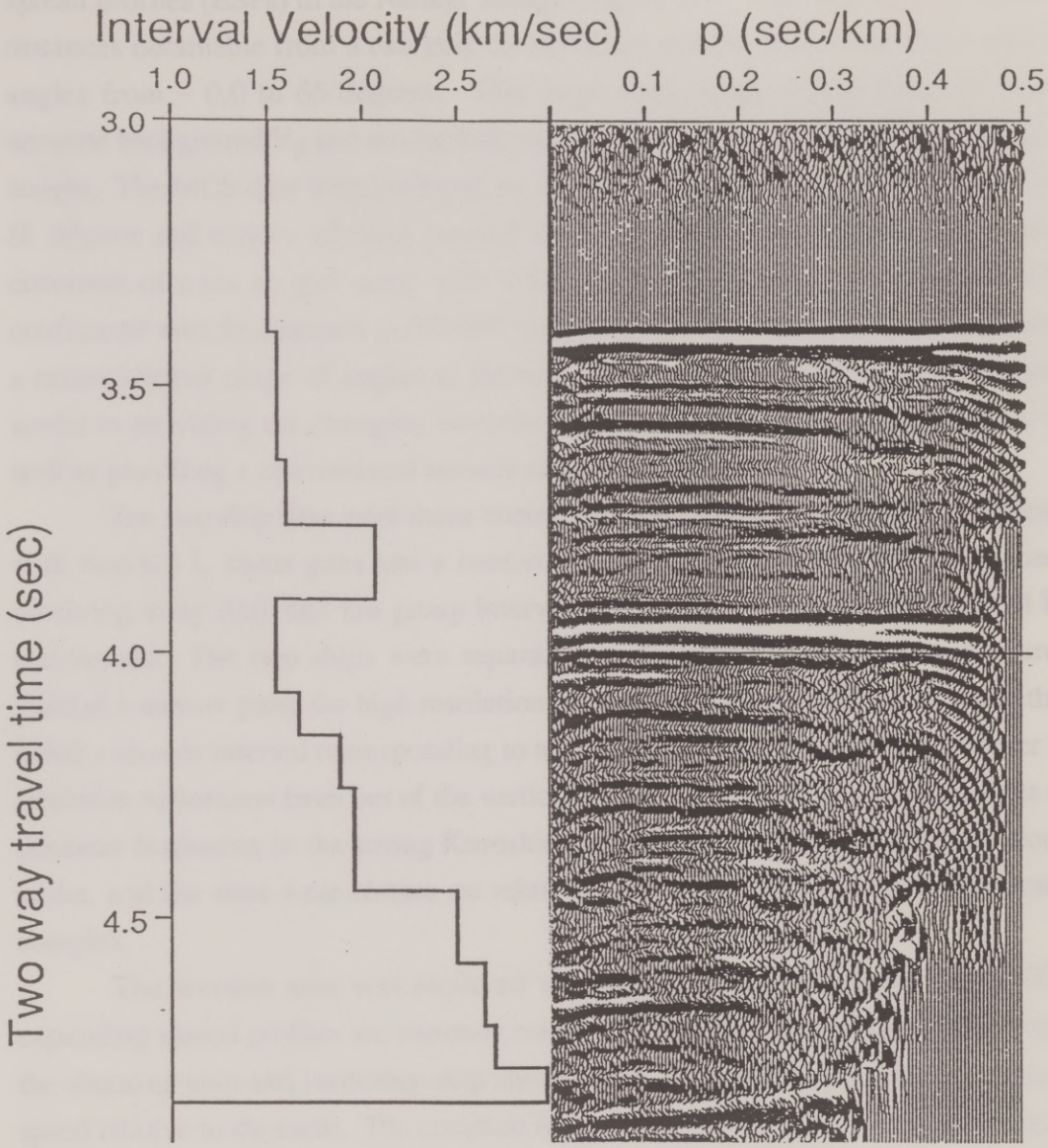

Figure 1.3 The τ-p NMO corrected CMP1602 from the Carolina Trough demonstrates the accuracy of the high resolution travel time analysis. The smoothed version of this background velocity function is used as a starting model in the wave form inversion.

spread profiles (ESPs) in the Nankai Trough (Figure 1.4). The large source receiver distances obtainable from a two ship survey allow sonification of the target area at angles from ~ 0.0 to 65 degrees. This large angle range is necessary to obtain accurate background V_p and also to independently resolve the three elastic parameters sought. The MCS data were collected by the University of Texas with the *R.V. Fred H. Moore* and consist of three parallel dip lines, NT62-1, 2, and 3. The source consisted of a six air gun array with a 16.8 L capacity. The receiving array was configured with 96 channels at 0.01667 km group spacing. Although this represents a rather limited range of angles at the water bottom, the MCS data are still quite useful in providing the changing acoustic impedance between the two-ship sites, as well as providing a conventional seismic subsurface image.

The two ship data were more unconventional. The source ship was equipped with two 6.5 L water guns and a receiving ship was equipped with a 96 channel receiving array (0.01667 km group interval) so that fine offset resolution could be maintained. The two ships were separated up to 25 km. The water gun source yielded a narrow pulse for high resolution in time and the data were recorded with a 0.002 s sample interval corresponding to a Nyquist frequency of 250 Hz. In order to minimize reflections from out of the vertical source receiver plane and any effects of streamer feathering in the strong Kuroshio current the profiles were acquired along strike, and the sites were chosen on relatively horizontal parts of the accretionary complex.

The western area was explored with ESPs, (Figure 1.4, lower left). The expanding spread profiles are common midpoint profiles which were collected while the shooting ship and receiving ship steamed toward a common center at the same speed relative to the earth. The common midpoints are indicated by circles in Figure 1.4, lower left and the ship tracks are shown by the lines trending NE to SW. The source receiver offsets of the ESPs range from 0.038 to 23.0 km.

As for the Carolina Trough data an accurate background V_p is very important for the inversion. An example of a τ-p NMO corrected ESP, (ESP15) is shown in Figure 1.5, verifying the accuracy of V_p.

Thus waveform inversion is performed on very different kinds of seismic data, in different environments and with different geologic goals. The conventionally

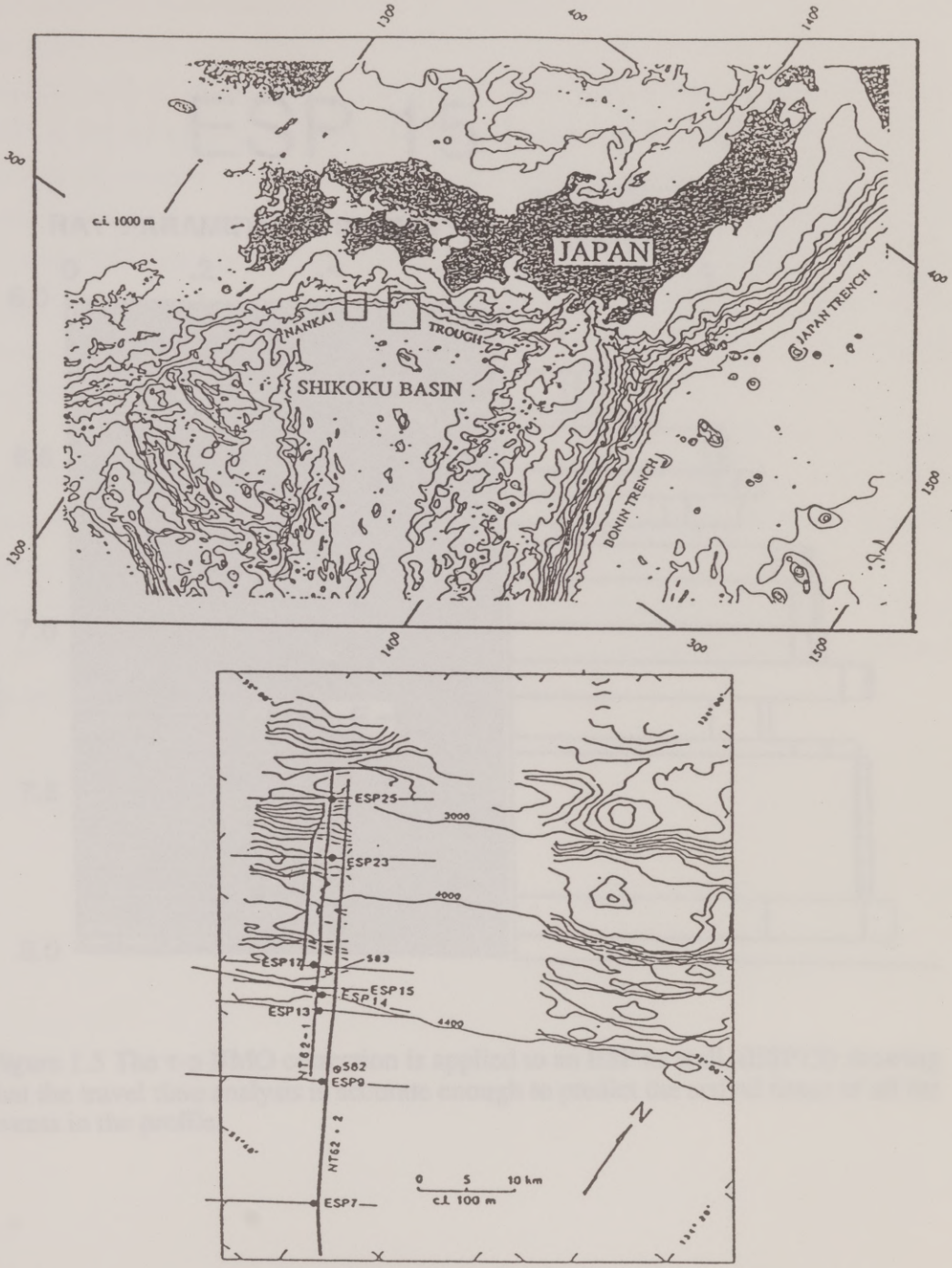

Figure 1.4. The Nankai Trough off the southern coast of Japan is the bathymetric expression of the subduction of the Phillipine sea plate. Ship tracks for the ESP (R/V Fred H. Moore and R/V Tansei Maru) profiles are indicated as are MCS lines NT62-1, NT62-2, and NT62-3, (R/V Fred H. Moore). (From Stoffa et al. 1992.)

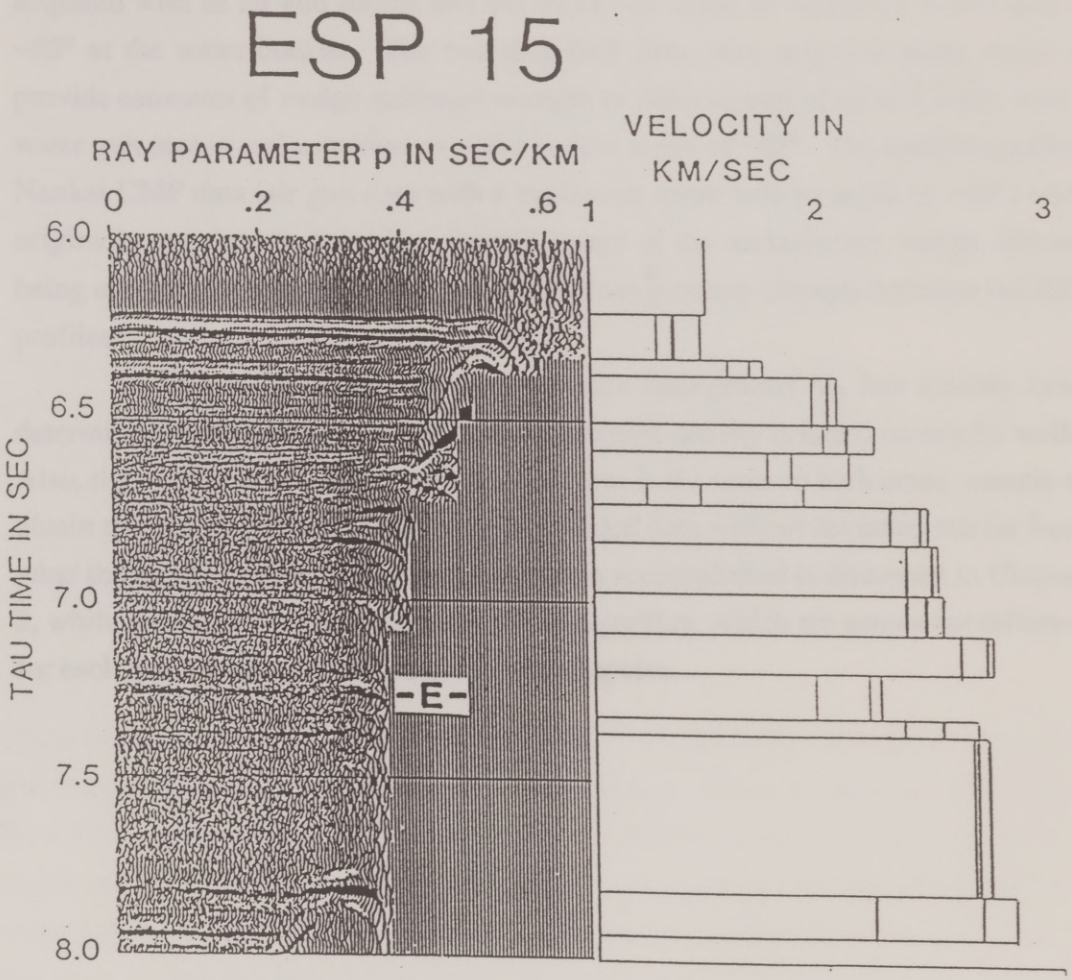

Figure 1.5 The τ-p NMO correction is applied to an ESP as well, (ESP15) showing that the travel time analysis is accurate enough to predict the arrival times of all the events in the profile.

acquired CMP data from the Carolina Trough are used to quantify methane content in the shallow (0.5 km) subsurface sediments in 2.5 km of water. The data were acquired with an air gun source and the maximum angle of incidence in this area is ~55° at the water bottom. The two ship ESP data were acquired along strike to provide estimates of wedge sediment strength in water depths of up to 5.0 km, with a water gun source and a maximum water bottom angle of ~65°. The smaller aperture Nankai CMP data (air gun data with a maximum water bottom angle of ~10°) were originally acquired to provide a seismic image of the accretionary wedge, but are being used here to provide estimates of sediment property changes between the ESP profiles.

In each of these locations an accurate background V_p has already been determined by travel time analysis and background density is based on nearby wells. Also, the geophysical objective of the algorithm is the same in both areas, namely to obtain the best fit between observed and modeled data without deviating too far from what the model is expected to be. How this is accomplished is discussed in Chapter 2, while the details of the application of the algorithm, which are somewhat different for each type of data, are discussed in later chapters.

Chapter 2

Inversion of Seismic Waveform Data

The Linearized Inverse

Quantitative investigation of detailed geologic features using reflection seismology requires the highest possible resolution. Recently several authors (McAulay, 1985, 1986 and Admunsen and Ursin, 1991) have shown the feasibility of obtaining very high resolution V_p and density profiles by iteratively modeling 1-D synthetic acoustic data. Dietrich and Kormendi (1990) and Mora (1986) used a similar approach and to a lesser extent have shown the feasibility of performing a similar analysis for 1-D elastic media. Assous et al. (1989) used another approach and achieved reasonable results on synthetic data. I review inversion theory here as applied to the problem of recovering an earth model from reflection seismic data.

The ground work for the class of problems and solutions used here has been discussed extensively in Menke (1989) and Tarantola (1987). I define the general forward problem as

$$\mathbf{d} = \mathbf{g}(\mathbf{m}) + \mathbf{v}$$

where $\mathbf{m}$ is a vector of n_{mod} model parameters which sufficiently describe the earth, $\mathbf{g}$ is an operator, in this case containing information on elastic wave propagation and the experimental configuration, $\mathbf{v}$ is a vector of additive noise, and $\mathbf{d}$ is a vector of n_{dat} data which would be observed if the earth was perfectly described by $\mathbf{m}$, if $\mathbf{g}$ was a perfect theoretical relation, and if $\mathbf{v}$ was identically zero. (Vectors and vector functions of vectors are cast in lower case bold type while matricies are cast in uppercase bold type). The inverse problem can then be defined as

$$\mathbf{m} = \mathbf{y}(\mathbf{d}-\mathbf{v})$$

where $\mathbf{v}$ can be absorbed into the data vector, and $\mathbf{y}$ is some generalized inverse, the structure of which is the subject of much discussion in the literature.

One convenient way of addressing this problem is to put it in the form of a global optimization where the solution corresponds to the minimum of some

function, (Figure 2.1). This objective function (also called cost or error function) is a function of the observed data, and a model guess, and possibly other parameters. Once the form of the function is chosen, one merely evaluates the function for many different models and assumes that the least value found corresponds to the correct model. Monte Carlo inversion methods use purely random model guesses while more sophisticated methods such as simulated annealing, or genetic algorithms (Stoffa and Sen, 1991) use current attempts to guide the next model estimate. Unfortunately these methods require many (perhaps 10s of thousands) objective function evaluations, each of which may be quite time consuming.

However, if the forward problem is linear, and the objective function is chosen wisely, then the slope and curvature of the function at any evaluation point can be used to generate a very good guess as to where the minimum lies. (If the problem is near linear the slope and curvature may have to be re-evaluated at each model estimate, making the solution iterative). For this study a least squares objective function is used, defined as

$$2S = \sum_{i=1}^{n_{dat}} \sum_{j=1}^{n_{dat}} [g^i(m_n) - d_{obs}{}^i] \; [\, C_D{}^{-1}]^{ij} \; [g^j(m_n) - d_{obs}{}^j]$$

$$+ \sum_{k=1}^{n_{mod}} \sum_{l=1}^{n_{mod}} [m^k - m_o{}^k] \; [\, C_m{}^{-1}]^{kl} \; [m^l - m_o{}^l]$$

(superscripts i, j, k, and l denote vector and matrix elements), or more compactly in vector notation

$$2S = [\; \Delta \mathbf{d}^t \, \mathbf{C}_D{}^{-1} \, \Delta \mathbf{d} + \Delta \mathbf{m}^t \, \mathbf{C}_m{}^{-1} \, \Delta \mathbf{m} \;]$$

with $\Delta \mathbf{d} = [\mathbf{d}_{syn} - \mathbf{d}_{obs}] = [\mathbf{g}(\mathbf{m}_n) - \mathbf{d}_{obs}]$

and $\Delta \mathbf{m} = [\mathbf{m}_n - \mathbf{m}_o]$

where $\mathbf{C}_D$ and $\mathbf{C}_m$ are prior data and model covariance matricies respectively, and $\mathbf{m}_o$ and $\mathbf{m}_n$ are model vectors containing the prior and n^{th} trial model parameters respectively, (superscript t denotes transpose). The vector $\mathbf{d}_{obs}$ contains the

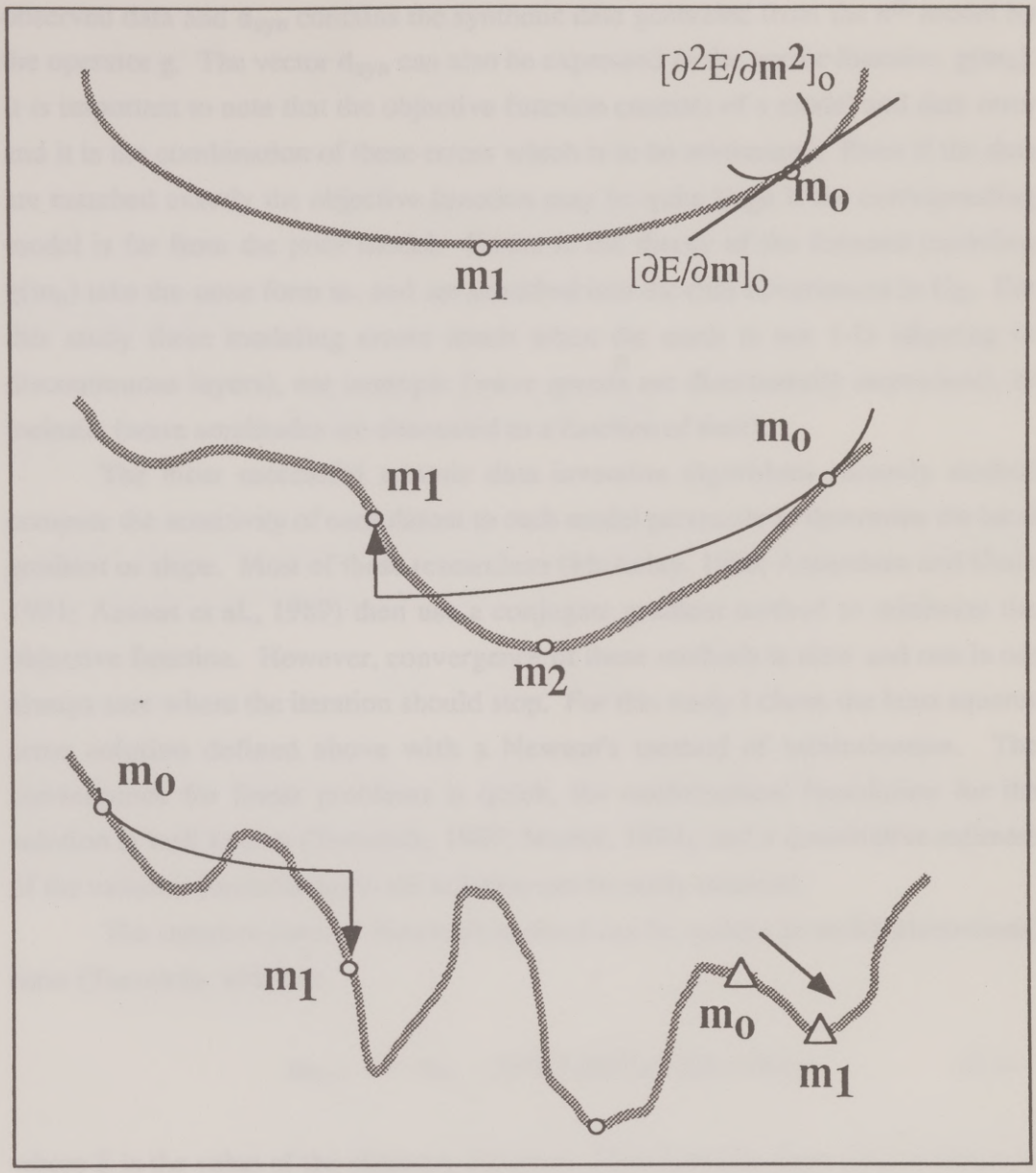

Figure 2.1. This shows three 1-D objective functions (grey) of varying complexity which are to be minimized. Random methods simply evaluate the curve at many points, the smallest of which is hoped to be the minimum. Gradient methods (triangles) use the slope to find the nearest minimum, and Newton's method (used in this study) uses the slope (first derivative) and curvature (second derivative) to make a parabolic fit. For increasingly non parabolic functions (middle) Newton's method may require more than one iteration to converge, and for extremely non parabolic functions (bottom) it will fail.

observed data and $\mathbf{d}_{syn}$ contains the synthetic data generated from the n^{th} model by the operator $\mathbf{g}$. The vector $\mathbf{d}_{syn}$ can also be expressed as the vector function, $\mathbf{g}(\mathbf{m}_n)$. It is important to note that the objective function consists of a model and data error and it is the combination of these errors which is to be minimized. Even if the data are matched exactly the objective function may be quite large if the corresponding model is far from the prior model. Errors in the theory of the forward modeling $\mathbf{g}(\mathbf{m}_n)$ take the same form as, and are absorbed into the data covariances in $\mathbf{C}_D$. For this study these modeling errors result when the earth is not 1-D (dipping or discontinuous layers), not isotropic (wave speeds are directionally dependent), or inelastic (wave amplitudes are attenuated as a function of time).

The most successful seismic data inversion algorithms recently studied compute the sensitivity of each datum to each model parameter to determine the local gradient or slope. Most of these researchers (McAulay, 1986; Amundsen and Ursin 1991; Assous et al., 1989) then use a conjugate gradient method to minimize the objective function. However, convergence of these methods is slow and one is not always sure where the iteration should stop. For this study I chose the least squares error solution defined above with a Newton's method of minimization. The convergence for linear problems is quick, the mathematical foundation for the solution is well known (Tarantola, 1987; Menke, 1989), and a quantitative estimate of the variance (uncertainty) in the solution can be easily obtained.

The iterative form of Newton's method can be written in multi-dimensional form (Tarantola, 1987) as

$$\mathbf{m}_{n+1} = \mathbf{m}_n - [\partial^2 S / \partial \mathbf{m}^2]_n^{-1} [\partial S / \partial \mathbf{m}]_n \qquad (2.1)$$

where S is the value of the objective function. Here both the slope and curvature of the model space at the n^{th} iteration are used to define a multi dimensional parabola, the apex of which represents the location of the $n+1^{th}$ model estimate, (Figure 2.1). For a parabolic objective function the minimum will be found in one iteration.

Taking the derivative of S to find the multidimensional slope yields

$$[\partial S / \partial \mathbf{m}]^k_n = \sum_{i=1}^{n_{mod}} \sum_{j=1}^{n_{dat}} G_n^{ik} \, [C_D^{-1}]^{ij} \, [g^j(\mathbf{m}_n) - d_{obs}^j]$$

$$+ \sum_{l=1}^{n_{mod}} [C_m^{-1}]^{kl} \, [m^l - m_o^l]$$

or in vector notation

$$= \mathbf{G}_n^t \mathbf{C}_D^{-1} \Delta \mathbf{d} + \mathbf{C}_m^{-1} \Delta \mathbf{m}$$

(2.2)

where the matrix $\mathbf{G}_n$ (sensitivity or Frechet derivative matrix) contains the sensitivity of each data parameter to each model parameter

$$G_n^{ij} = [\partial d^i / \partial m^j]_n$$

evaluated at the position of the n^{th} model. Its dimension is the number of data parameters (n_{dat}) by the number of model parameters (n_{mod}). Taking the second derivative to find the local curvature yields

$$[\partial^2 S / \partial \mathbf{m}^2]_n^{kl} = \sum_{i=1}^{n_{mod}} \sum_{j=1}^{n_{dat}} G_n^{ik} \, [C_D^{-1}]^{ij} \, G_n^{jl} + [C_m^{-1}]^{kl}$$

$$+ \sum_{i=1}^{n_{mod}} \sum_{j=1}^{n_{dat}} [\partial G^{ik} / \partial m^l]_n \, [C_D^{-1}]^{ij} \, [g^j(m_n) - d_{obs}^j].$$

Since the last term of this expression is difficult to compute and will be small if either the problem is linear, ($[\partial G^{ik}/\partial m^l]_n \approx 0$), or if the data residuals are small, ($[g^j(m_n) - d_{obs}^j] \approx 0$) it is dropped. This gives

$$[\partial^2 S / \partial \mathbf{m}^2]_n \approx \mathbf{G}_n^t \mathbf{C}_D^{-1} \mathbf{G}_n + \mathbf{C}_m^{-1} \, . \qquad (2.3)$$

Combining Equations 2.1, 2.2, and 2.3 gives the expression used in this study,

$$\mathbf{m}_{n+1} = \mathbf{m}_n - [\mathbf{G}_n^t \mathbf{C}_D^{-1} \mathbf{G}_n + \mathbf{C}_m^{-1}]^{-1} [\mathbf{G}_n^t \mathbf{C}_D^{-1} \Delta\mathbf{d} + \mathbf{C}_m^{-1} \Delta\mathbf{m} \quad (2.4)$$

where $\mathbf{G}_n$ is re-computed at each iteration and each of the other components on the right hand side is known at the start of the inversion.

Note that if the forward problem is linear then

$$\Delta\mathbf{d} = \mathbf{G}\,\Delta\mathbf{m}$$

exactly and

$$S = [\,(\mathbf{G}\,\Delta\mathbf{m})^t \mathbf{C}_D^{-1} (\mathbf{G}\,\Delta\mathbf{m}) + \Delta\mathbf{m}^t \mathbf{C}_m^{-1} \Delta\mathbf{m}\,]$$

which is quadratic in $\Delta\mathbf{m}$. Thus the Newton method will converge in one iteration.

Parameterization

Although the above calculations appear quite straight forward there is a major question as to how the problem should be parameterized so as to minimize computation time while still providing the desired information. The highest possible vertical resolution in V_p, V_s, and density is desired so the problem is over parameterized, i.e. the earth is divided into many thin layers, probably more than what are needed. If the fine layering is not required in some areas then neighboring layers should have similar properties. The layer thickness varies such that P-wave travel time across each layer is constant and equal to the sample rate of the data, ensuring that all frequencies recorded will be included in the result. The effects of differing parameterizations are discussed later.

In this study the earth model has been chosen to consist of a stack of n_{lay} homogeneous, isotropic, elastic layers each with an independently varying V_p, V_s, and density, (Figures 2.2 and 2.3). The first n_{lay} components of the model vectors are the P-wave velocities, the next n_{lay} components are the layer densities, and the last n_{lay} components are the layer S-wave velocities. The model space therefore has dimension $n_{mod} = 3 \times n_{lay}$. One feature of this parameterization is that portions of

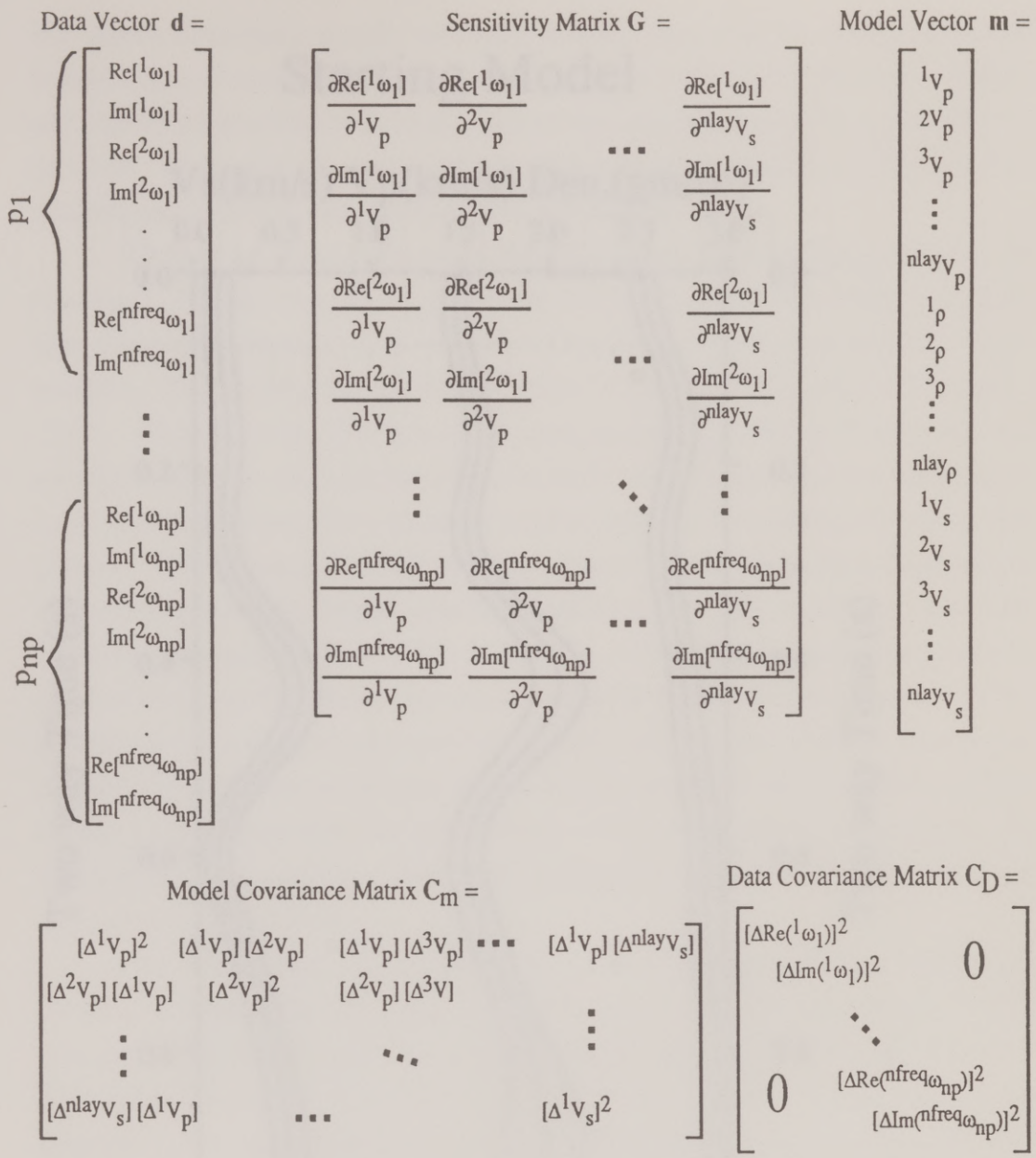

Figure 2.2. In this study the data vector is made up of the Fourier transform of each plane wave seismogram organized with increasing ω for increasing p. The sensitivity matrix contains the derivative of each datum to each model parameter. The model vector contains V_p, ρ, and V_S for each layer in the model. The model covariance contains the covariance of each model parameter with every other model parameter, with the diagonal representing the square of the standard deviation. The data covariance matrix is assumed diagonal and holds the variances of each datum.

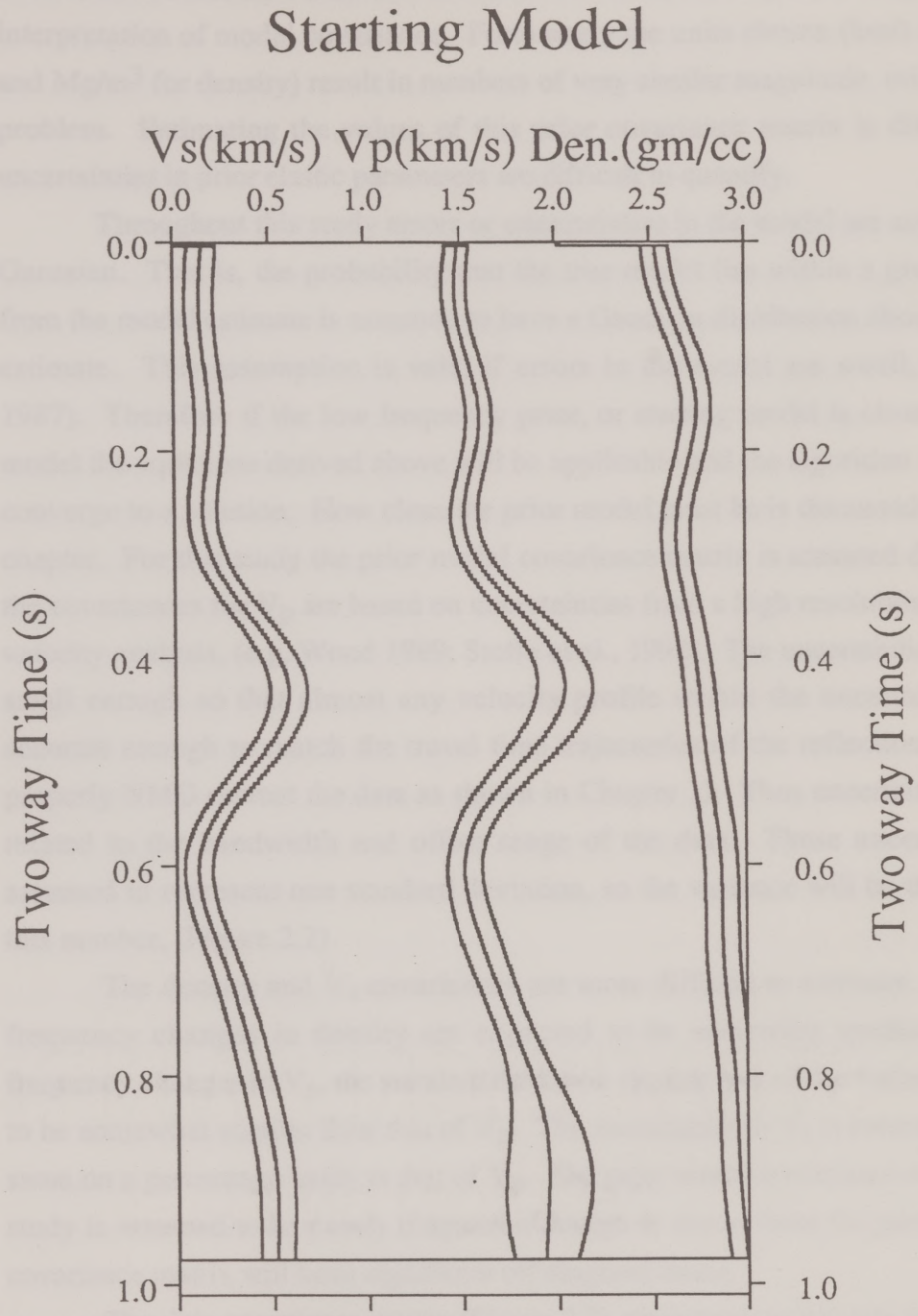

Figure 2.3. For the inversion in this study the earth is modeled, or parameterized as a 1-D stack of isotropic, homogeneous elastic layers each with independently varying V_p, V_s, and density. The model vector holds each of the elastic parameters for each layer. In the smooth model shown here the elastic parameters from layer to layer vary smoothly, producing minimal reflections, but contain enough V_p information such that two way travel times are correct.

the model covariance matrix will have mixed units, slightly complicating the interpretation of model covariance. Fortunately the units chosen (km/s for velocity and Mg/m^3 for density) result in numbers of very similar magnitude, mitigating this problem. Estimating the values of this prior covariance matrix is difficult since uncertainties in prior elastic parameters are difficult to quantify.

Throughout this study errors or uncertainties in the model are assumed to be Gaussian. That is, the probability that the true model lies within a given distance from the model estimate is assumed to have a Gaussian distribution about the model estimate. This assumption is valid if errors in the model are small, (Tarantola, 1987). Therefore if the low frequency prior, or starting model is close to the true model the equations derived above will be applicable and the algorithm will quickly converge to a solution. How close the prior model must be is discussed later in this chapter. For this study the prior model covariance matrix is assumed diagonal and the covariances for V_p are based on uncertainties from a high resolution travel time velocity analysis, (e.g. Wood 1989; Stoffa et al., 1992). The uncertainties should be small enough so that almost any velocity profile within the uncertainty will be accurate enough to match the travel time trajectories of the reflection events, (or properly NMO correct the data as shown in Chapter 1). Thus uncertainties will be related to the bandwidth and offset range of the data. These uncertainties are assumed to represent one standard deviation, so the variance will be the square of this number, (Figure 2.2)

The density and V_s covariances are more difficult to estimate. Since high frequency changes in density are expected to be somewhat smaller than high frequency changes in V_p, the standard deviation (square root of the variance) is taken to be somewhat smaller than that of V_p. The uncertainty in V_s is assumed to be the same on a percentage basis as that of V_p. The prior model covariance matrix in this study is assumed to be purely diagonal although as shown later the posterior model covariance matrix will have significant off diagonal terms.

The data covariance matrix (Figure 2.2) represents uncertainty in the data, in this case the complex frequencies. For example assume a signal level of 0.2 (water bottom reflectivity) and a random additive noise level whose standard deviation corresponds to a reflectivity of 0.04. This yields a signal to noise ratio of 5 or 14 db.

After Fourier transform over 512 samples this corresponds to an uncertainty of ~2.0 or a variance of ~4.0 so diag[C_D] = 4.0. Similarly a signal to noise ratio of 20 db corresponds to diag[C_D] = 1.3, and 40 db to diag[C_D] = 0.013.

Sensitivities

Calculation of the sensitivity matrix, G_n, in the offset vs. time (x-t) domain can be a very time consuming part of the above calculations. This time can be substantially reduced if the data being modeled are plane wave data (Brysk and McCowan, 1986a) as obtained from a plane wave decomposition, (PWD). In this domain the reflectivity method of Kennett and Kerry (1979) can be used as the forward algorithm to quickly generate the plane wave reflectivity for a 1-D stack of layers. McAulay (1986) and Amundsen and Ursin (1991) have shown that the sensitivity matrix can be computed analytically very quickly for seismograms in the domain of ω (angular frequency) and p (inverse of apparent horizontal phase velocity, also called ray parameter, Snell parameter, or horizontal slowness). They proceed by computing the analytical derivative of the reflectivity response at each ω and p to each layer V_p and ρ, (Figure 2.2). This can be done for the elastic case as well, at the cost of coding and debugging a large quantity of algebra.

Alternatively, Dietrich and Kormendi (1990) calculate the sensitivities by invoking the Born approximation (amounting in this case to assuming no interbed multiples) and computing the Green's functions for each layer elastic parameter. Although the contribution from interbed multiples will likely be small, it takes only slightly more effort to avoid making this assumption thus making the algorithm more general.

To compute the sensitivities I use an efficient numerical perturbation scheme, (Figure 2.4). When computing the forward problem, the reflectivity of the stack of layers is built up by combining the reflectivity at each layer (Kennett and Kerry, 1979). If just the reflectivity response is desired then only the last iteration is saved. To calculate the sensitivities, however, the response at each level is saved. The process is repeated from the top down, again saving the response at each level. At this point each elastic parameter of each layer is perturbed. When layer j is perturbed the reflectivity response from j+1 to the lower half space and from j-1 to the surface

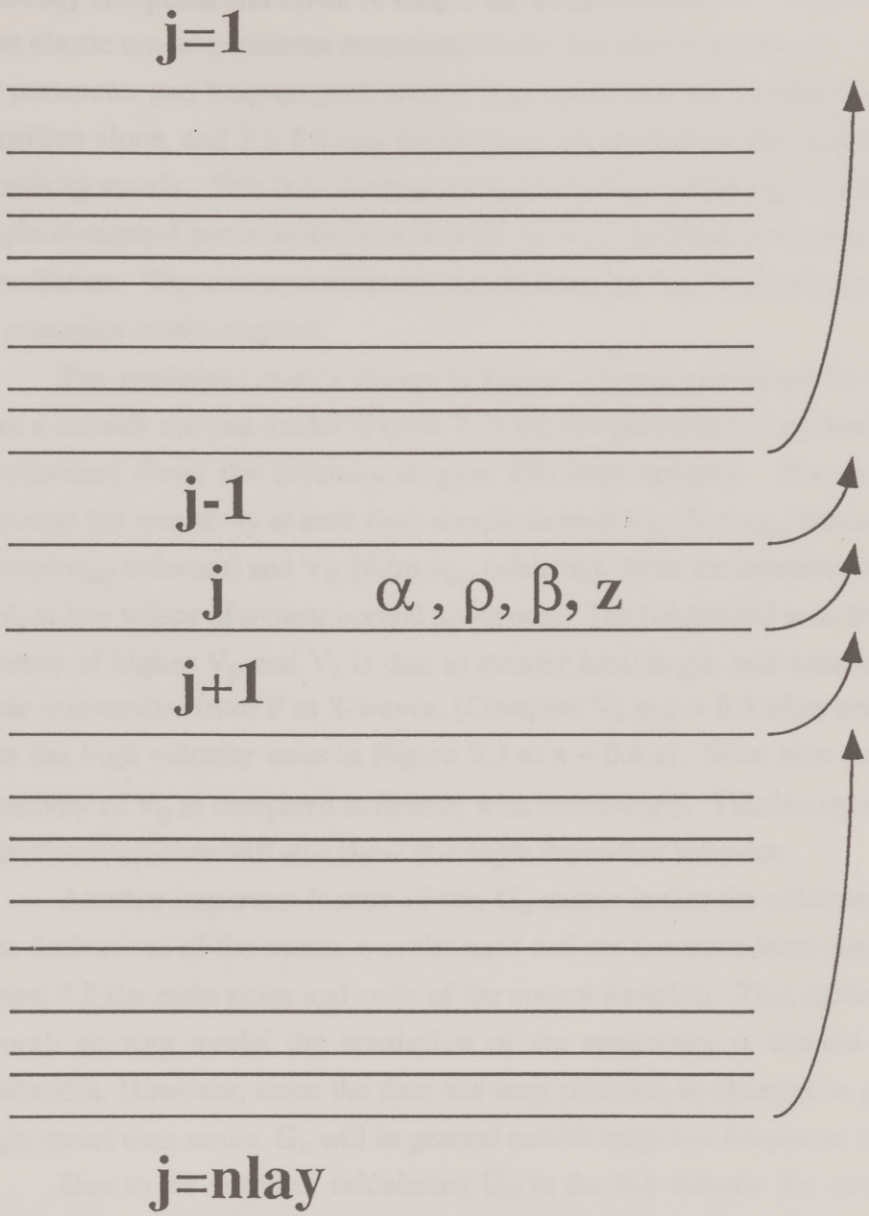

Figure 2.4. The reflectivity is built from the reflectivities of each layer, combined from the bottom up. To generate the sensitivities the response at each layer is saved. For each layer j, a parameter is perturbed changing the reflectivity of the interfaces above and below. The lower response is combined with the three perturbed reflectivities and is then combined with the upper response to form the perturbed response for this frequency.

is already computed and saved so only 3 layer combinations are required for each of three elastic model parameter perturbations for that elastic parameter. Thus for each ray parameter and frequency of interest n_{lay} operations are needed for the forward algorithm alone, and 3 x 3 x n_{lay} (order n_{lay}) are needed for the calculation of the sensitivity matrix. This is in contrast to n_{lay} x 3 x n_{lay} (order n_{lay}^2) operations for a simple numerical perturbation in which the forward problem is recomputed for each perturbation. The computational savings increase as n_{lay} increases, (n_{lay} = 244 for the examples in this chapter).

The sensitivity matrix shown in Figure 2.5 was calculated for this problem from a smooth starting model (Figure 2.3) via this perturbation method and Fourier transformed along the columns to give 256 time samples. The first 256 rows represent the sensitivity at each time sample to each V_p, (first n_{lay} columns), density, (second n_{lay} columns) and V_s, (third n_{lay} columns). Note the insensitivity of the data to V_s at low values of p (near normal incidence). The heightened sensitivity of the V_s in areas of higher V_p and V_s is due to greater local angle and subsequent greater mode conversion from P to S-waves, (Compare V_s at p = 0.3 s/km and at $\tau \sim 0.4$ s with the high velocity zone in Figure 2.3 at $\tau \sim 0.4$ s). Note also the increase in sensitivity of V_p as compared to density with increasing p. This is expected since the reflection amplitude will also show this angle dependent behavior.

Another important feature of this $\mathbf{G}_o$ matrix is that the columns are actually time derivatives of the source wavelet used and are therefore band limited, (note in Figure 2.5 the main pulse and coda of the source wavelet). This shows that for the smooth starting model the resolution of the sensitivity is limited by the data bandwidth. However, since the data are very sensitive to changes in phase caused slight travel time errors, $\mathbf{G}_n$ will in general exhibit large low frequency features.

Due to the speed of calculating $\mathbf{G}_n$ in the ω-p domain the entire inversion (Equation 2.4) is performed in this domain, (the details of transforming the field data to this domain are discussed in Chapter 3). Therefore the vectors $\mathbf{d}_{obs}$ and $\mathbf{d}_{syn}$ are organized with successive components of the vector occupied by increasing ω for each successive p, corresponding to each column of $\mathbf{G}_n$. However, the values of the elements of the associated data covariance matrix $\mathbf{C}_D$ are not completely certain.

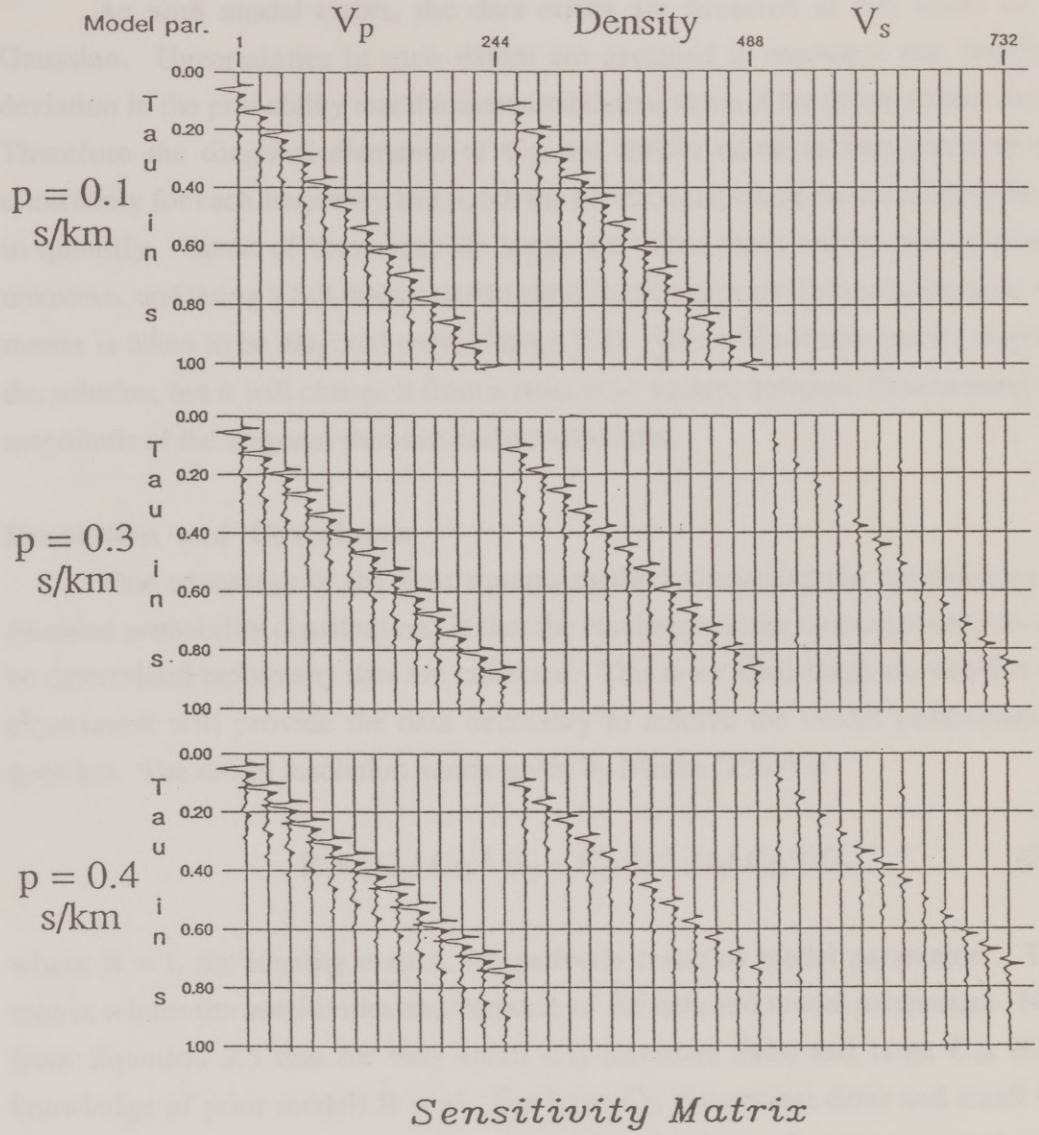

Figure 2.5. The sensitivity matrix $\mathbf{G}_0$ with columns Fourier transformed to time was calculated for the smooth starting model in Figure 2.2, (only every 20th trace is shown). Note the increasing sensitivity to model layers with higher velocities, and the increasing sensitivity to S-wave velocity with increasing p (angle).

As with model errors, the data errors are assumed in this study to be Gaussian. Uncertainties in each datum are assumed to represent one standard deviation in the probability that the measured datum value is the actual datum value. Therefore the diagonal elements of $\mathbf{C_D}$ are simply taken as the square of the uncertainty for each frequency and p, but the off diagonal elements are more difficult to quantify. Some of these may be large, but since these values are relatively unknown, and using a full matrix would significantly increase computation time, the matrix is taken to be diagonal only, (Figure 2.2). This will not necessarily degrade the solution, but it will change it from a strict least squares solution. Determining the magnitude of the diagonal elements is discussed later.

Resolution and Covariance

One advantage of the least squares method, (including the assumptions of gaussian probability distributions) is that the resolution of the model parameters can be determined before any data are collected. This is an ideal check on whether the experiment will provide the data necessary to resolve the model parameters in question. The model resolution matrix given by Menke (1989) is

$$\mathbf{R} = [\mathbf{G_n}^t \mathbf{C_D}^{-1} \mathbf{G_n} + \mathbf{C_m}^{-1}]^{-1} \mathbf{G_n}^t \mathbf{C_D}^{-1} \mathbf{G_n} , \qquad (2.5)$$

where $\mathbf{R} = \mathbf{I}$, the identity matrix, for perfectly resolved model parameters. This matrix relates the sensitivities and variance of the data and model parameters. Note from Equation 2.5 that for very small $\mathbf{C_D}$ (accurate data) and large $\mathbf{C_m}$ (little knowledge of prior model) $\mathbf{R} = \sim\mathbf{I}$. For large $\mathbf{C_D}$ (inaccurate data) and small $\mathbf{C_m}$ (very well known prior model) $\mathbf{R} = \sim\mathbf{C_m}$. Thus by estimating the expected noise (variance in prior model and measurements of data) one can obtain a measure of how well each model parameter is resolved.

Figure 2.6 shows **R** for **G** calculated for the smooth starting model shown in Figure 2.3 (including the discontinuity at the water bottom) with diag[$\mathbf{C_D}$] = 1.0. The units of these elements are dimensionless since they correspond to 1/(reflectivity)^2. This matrix can be thought of as a composite of nine sub-matricies, the upper left representing the resolution of each layer V_p with respect to every other

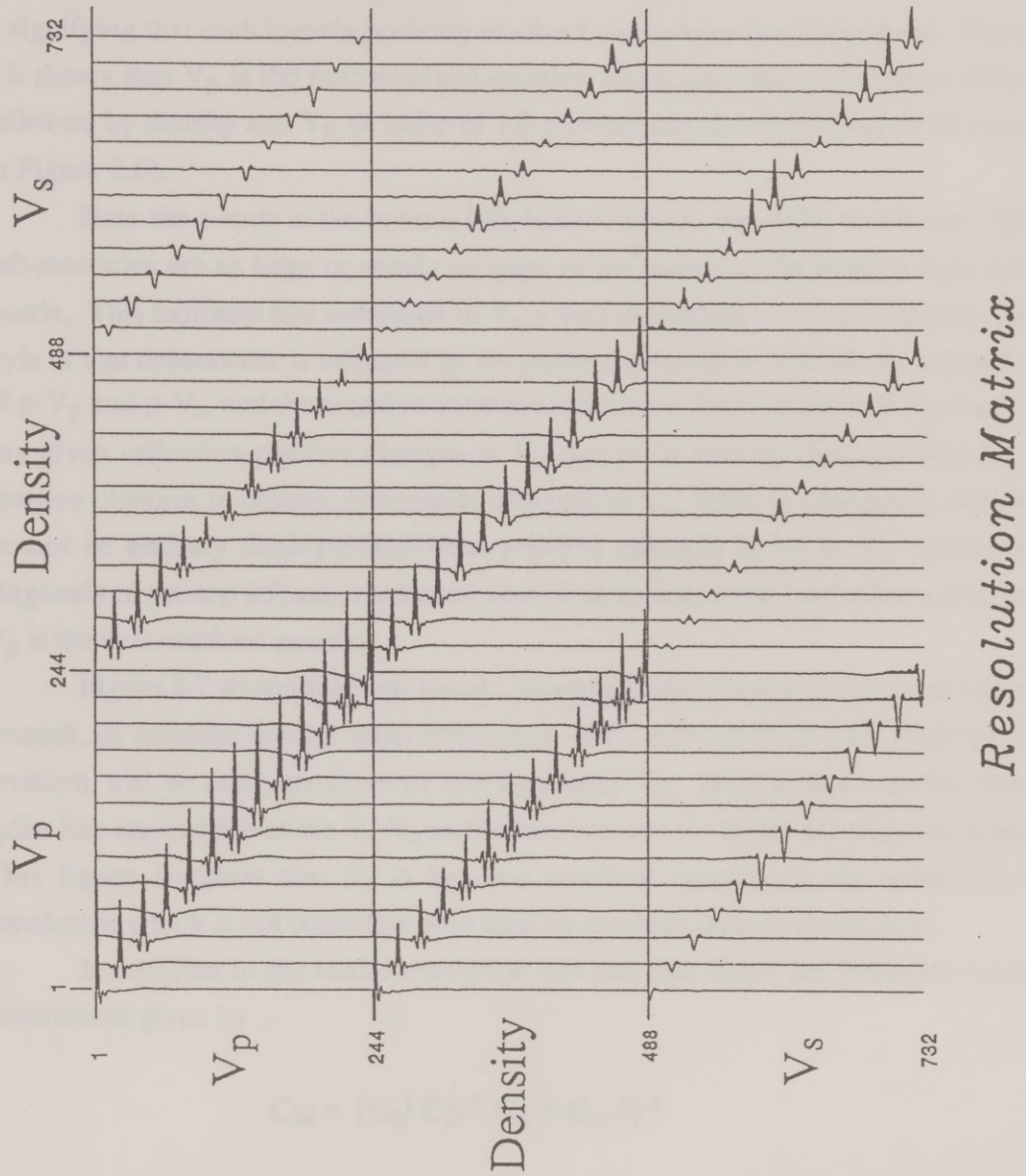

Figure 2.6. This is every 20th column of the model resolution matrix for the problem with p = 0.0 to p = 0.4 s/km and the diag[C_D] = 1.0. Note the high resolution of P-wave velocity compared to the other quantities, and the dependence of V_S resolution on that of V_P and density.

layer V_p, the center representing the resolution of each layer density with respect to every other layer density, and the lower right representing the resolution of each layer V_s with respect to each other layer V_s. In an ideal experiment one would expect R = I, signifying that each layer is perfectly resolved and independently resolved. Figure 2.6 shows that V_p is the best resolved quantity (diagonal values closest to unity), followed by density and V_s, (a value of 1.0 corresponds to a deflection of 10 traces in Figure 2.6).

Note the events in the bottom left, bottom center, top right, and center right sub-matricies are as large or nearly as large as the events in the bottom right sub-matrix. This indicates that resolution of V_s is very dependent on V_p and density. The style of that dependence is indicated by the positive correlation between the resolution of ρ-V_p and ρ-V_s, and the negative correlation between the resolution of V_p-V_s. For any given reflection positive changes in V_p cannot be entirely distinguished from positive changes in density or negative changes in V_s. Positive changes in density cannot be entirely distinguished from positive changes in V_p or V_s. Since the diagonals in the top left sub matrix are significantly larger than any other elements, V_p is the best resolved quantity.

Figure 2.7 shows the same matrix except that the starting model is no longer smooth, (it contains several small reflections ~0.03 and one large one, ~0.2) so the problem will be more sensitive to low frequency V_p. Note in this case the more spike like appearance of the V_s-V_s resolution, but also the larger off diagonal terms. This figure suggests that V_s is the best resolved quantity in the inversion, a conclusion which is not consistent with tests on synthetic data as shown later.

In addition to the model resolution one can also check the posterior model covariances given by

$$C_M = [G_n^t C_D^{-1} G_n + C_m^{-1}]^{-1}$$

where C_M is the posterior model covariance matrix, (Tarantola, 1987). Figure 2.8 shows this matrix computed from a realistic data noise level, diag[C_D] = 1.0, and is computed at the end of the inversion process and is therefore based on a rough model. This matrix can, like the resolution matrix, be thought of as a composite of

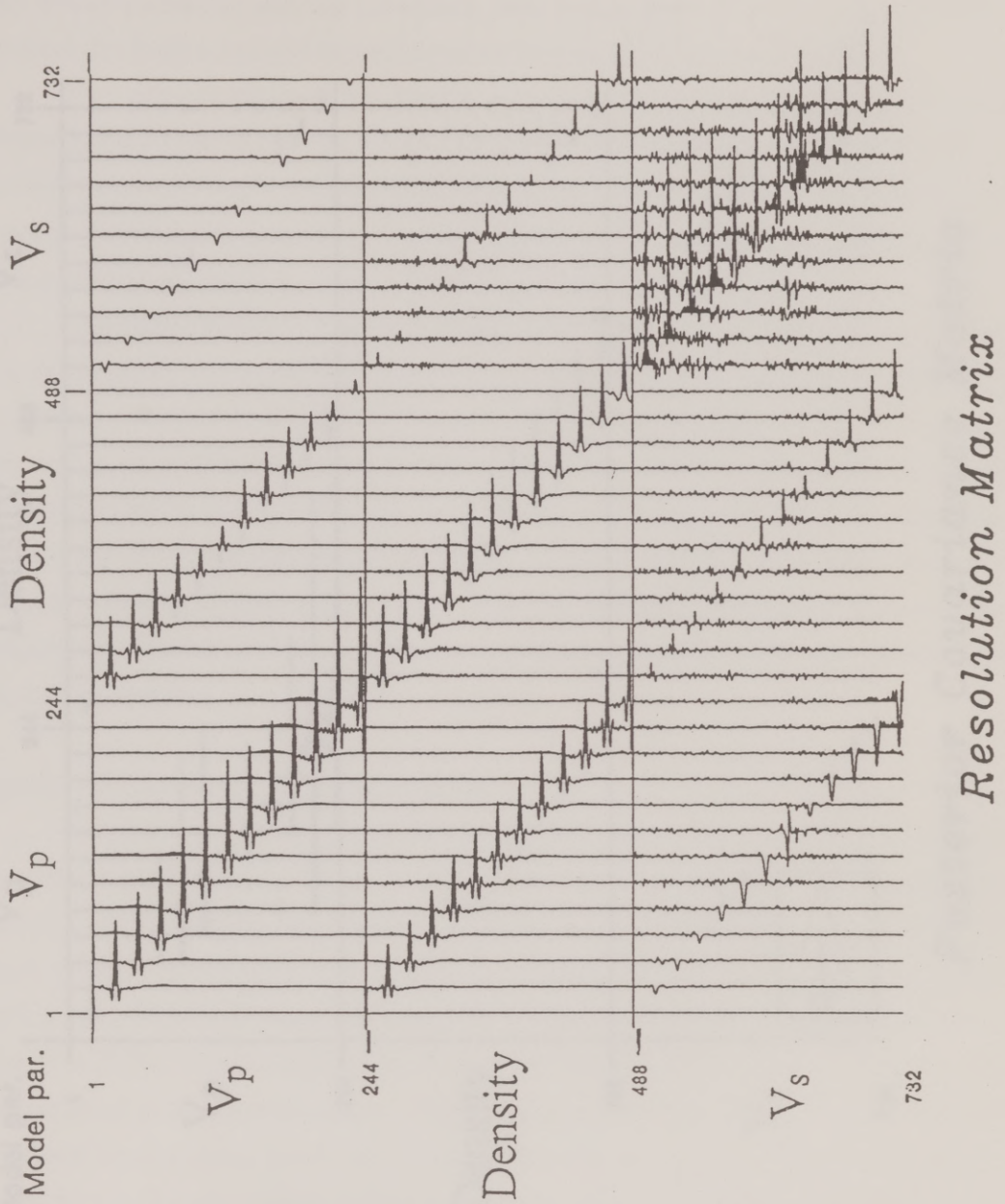

Figure 2.7. This model resolution matrix was computed assuming a model with some roughness, (every 20th column shown). Note the increased off diagonal terms for the V_S-V_S resolution.

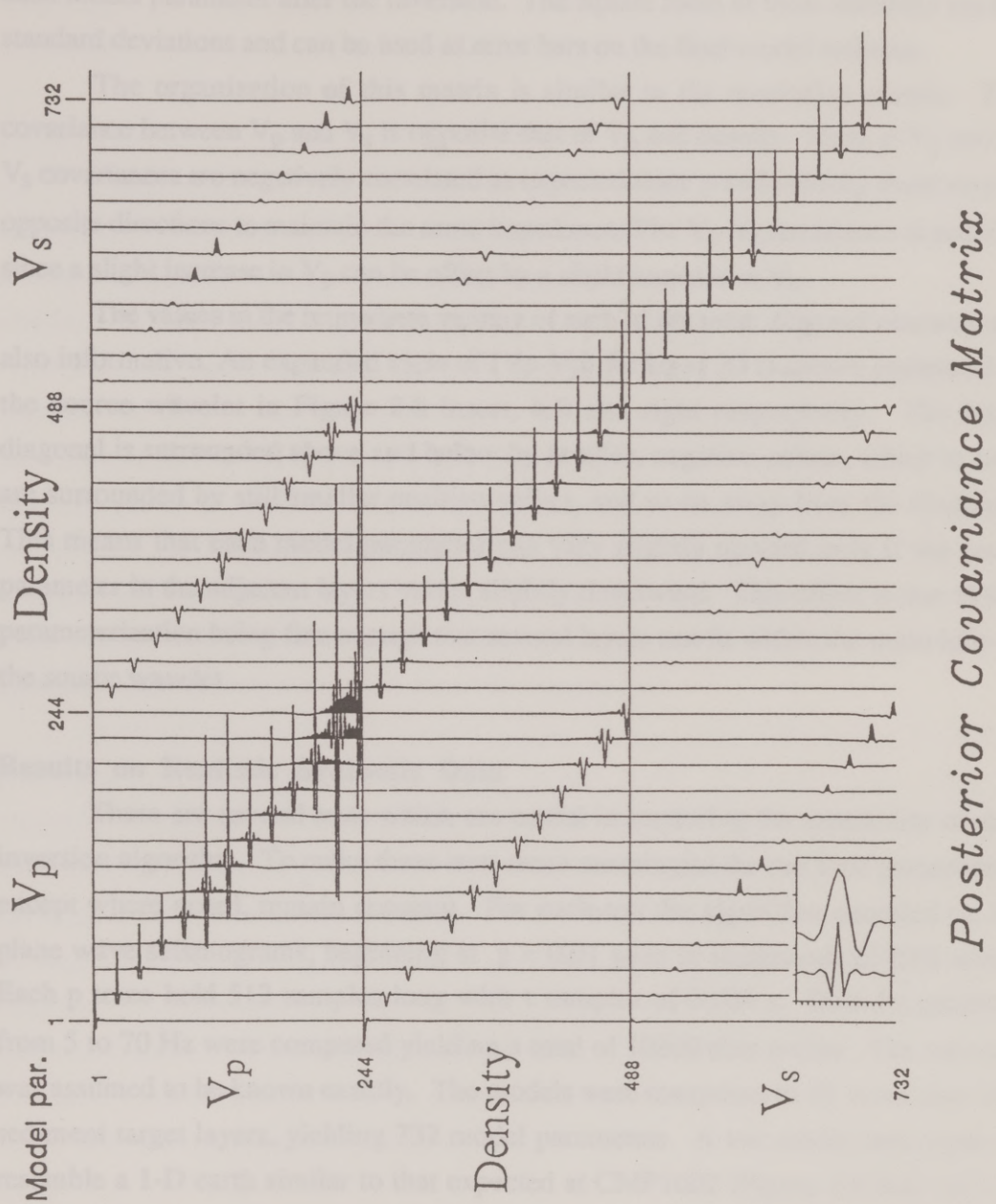

Figure 2.8. The posterior covariance matrix provides an estimate of the uncertainty in the final model. Off diagonal terms represent a correlation of uncertainty between model parameters, e.g. the terms in the lower left corner indicate how uncertainty in V_s is related to uncertainty in V_p. The insert shows the source wavelet (right), and an expanded view of V_p-V_p at layer 20 (left). The variations in covariance are higher than the data band pass.

nine sub-matricies. The values along the main diagonal represent the variance of each model parameter after the inversion. The square roots of these numbers are the standard deviations and can be used as error bars on the final model estimate.

The organization of this matrix is similar to the resolution matrix. The covariance between V_p and V_s is opposite that of V_p and density. Here, ρ-V_p and ρ-V_s covariances are negatively correlated as expected since ρ and velocity must vary in opposite directions to maintain the same impedance. The V_p-V_s covariance is positive since a slight increase in V_p can be offset by a slight increase in V_s.

The values in the immediate vicinity of each of the main diagonal elements are also informative. An expanded view of (Vp-Vp) for layer 20 is shown compared to the source wavelet in Figure 2.8 insert, left and right respectively. The large diagonal is surrounded above and below by smaller, negative values, which in turn are surrounded by still smaller positive values, and so on away from the diagonal. This means that each model parameter can vary slightly upward only if the same parameter in the adjacent layers varies slightly downward. This effect is due to the parameterization being fine enough that several layers can fit within the main lobe of the source wavelet.

Results on Realistic Synthetic Data

There are several tests which are useful in exploring the sensitivity of this inversion algorithm. To make these tests more meaningful the run time parameters, except where noted, remain constant. For each test the algorithm operated on 40 plane wave seismograms, beginning at $p = 0.01$ s/km in increments of 0.01 s/km. Each p trace held 512 samples long with τ samples of 0.004 s. Data frequencies from 5 to 70 Hz were computed yielding a total of 10800 data points. The wavelet was assumed to be known exactly. The models were composed of 12 water and 244 sediment target layers, yielding 732 model parameters. A test model was made to resemble a 1-D earth similar to that expected at CMP1602 (Figure 2.9 fine curve). The model contains frequencies as high as ~65 Hz. A starting model was obtained by smoothing the true model with a low pass 5 Hz filter, while retaining the sharp discontinuity at the water bottom, (Figure 2.3). The true model was used to generate a noiseless synthetic "observed" data set which was then inverted. The level of noise

present in the data is conveyed to the algorithm by the data covariance, C_D. Here diag[C_D] = 1.0. The seismograms shown in this chapter are all scaled so that 1 trace deflection is equal to a reflection coefficient of 0.2.

DATA ASSUMED PERFECT

The first test demonstrates the full power of the algorithm. Here diag[C_D] was set to 0.0025, corresponding to near perfect data. The result of this inversion is shown in Figure 2.9. The "observed data" (left) is shown adjacent to the true (fine) and best estimate (bold) models displayed in two way P-wave time. One hundred times the data residual is shown in Figure 2.9 (right), showing that the algorithm has matched the data to within ~40 db. Since the C_D matrix controls how closely the data are matched at the expense of the model, the prior model here was effectively ignored. However, since the data are truly noise free, the true model was very nearly recovered. The errors in the best estimate are small with the V_p error being the smallest, followed by density and V_s, (best seen at ~ 0.6 s). Decreasing diag[C_D] even further would reduce both the data and model residuals in this noise free example. Note the better fit above the high velocity zone.

Also of interest in this demonstration is the rate of convergence of this Newton's method algorithm, shown in Figure 2.10. Note the two orders of magnitude reduction in error (actually the combined data and model square error) after the first iteration showing the near linearity of the problem for this model, and the large error reduction that can be achieved with a single iteration. Another order of magnitude is achieved after two more iterations. For more non linear prblems, (e.g. models containg reverberations, or post critical events) a greater proportion of the error reduction occurs after the first iteration. Although this is significantly fewer iterations than have been used in other methods, (McAulay, 1986; Assous et al., 1989) only the high frequency model variations are sought here, not the background trend.

A small diag[C_D] corresponds to increased resolution and certainty (lower posterior model covariance) of model parameters. Figure 2.11 shows in model format the starting uncertainties (heavy dashed lines) and the posterior uncertainties (fine lines), which are the square root of the diagonals of the posterior covariance

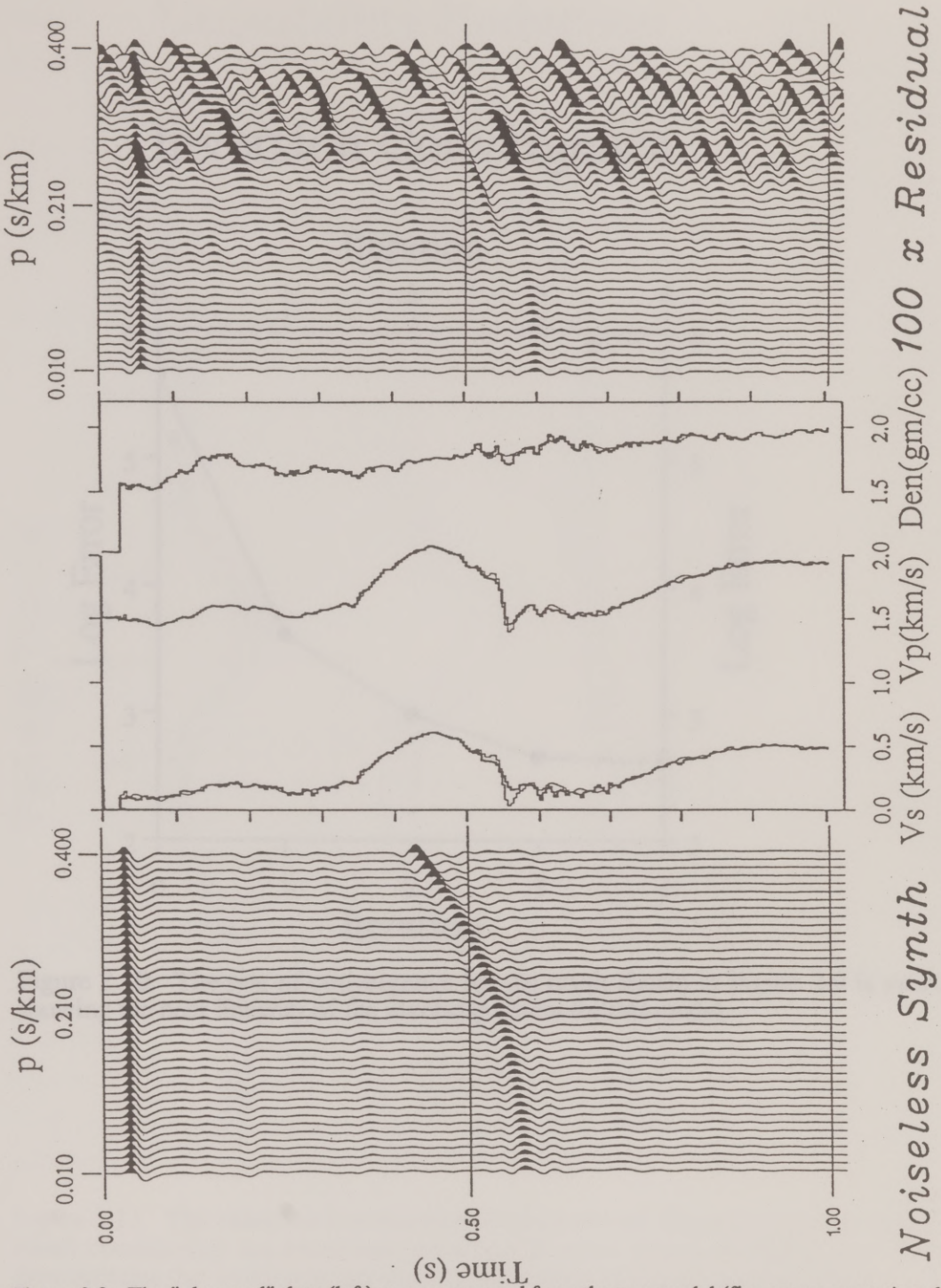

Figure 2.9. The "observed" data (left) were computed from the true model (fine curve, center) and inverted to yield the model estimate (bold curve, center) assuming diag[C_D] = 0.0025. One hundred times the difference between the "observed" data and the data computed from the best estimate is shown at right, indicating that the "observed" data have been accurately modeled.

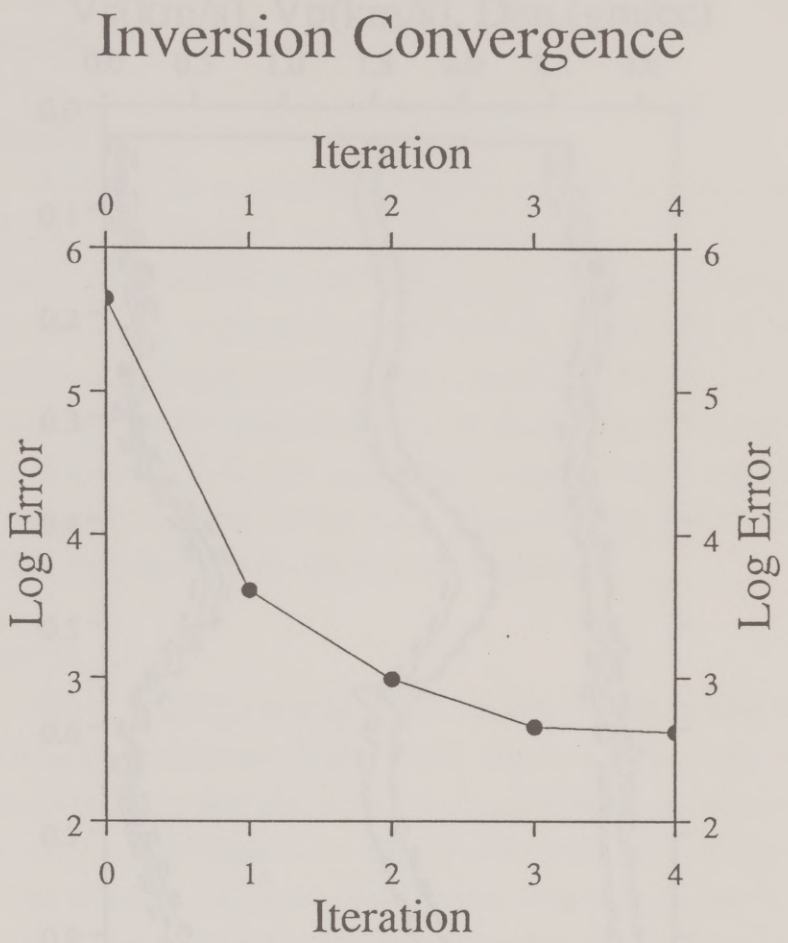

Figure 2.10. The rate of convergence for the result shown in Figure 2.9 is swift, showing the near linearity of the inverse problem for this model.

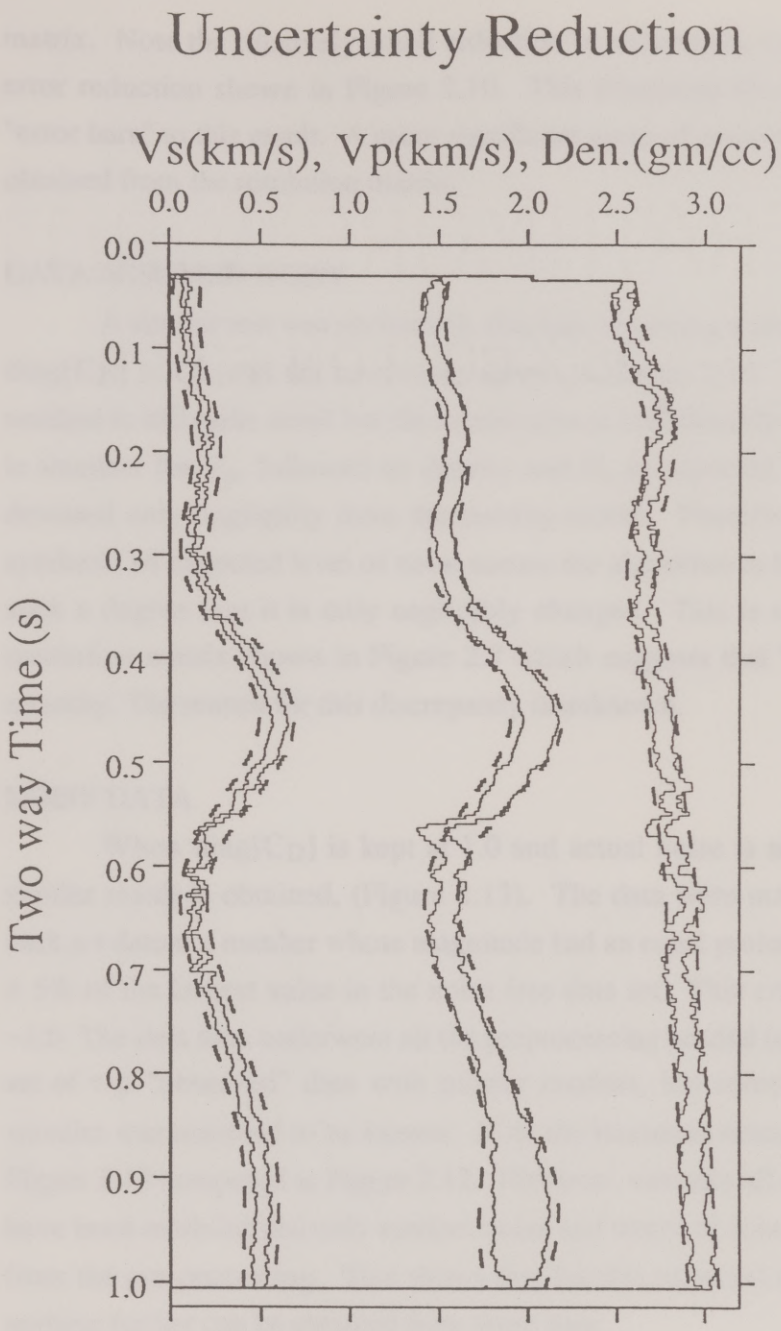

Figure 2.11. The reduction in uncertainty (square root of diagonal C_m) is relatively small considering the enormous reduction in error shown in Figure 2.9. This demonstrates that looking at just the diagonal values of C_m can be misleading.

matrix. Note the relatively small reduction in uncertainty even with the very large error reduction shown in Figure 2.10. This illustrates the difficulty in assigning "error bars" to this result. A more significant sense of accuracy of the final model is obtained from the resolution matrix.

DATA ASSUMED NOISY

A similar test was performed, this time assuming a more realistic noise level, diag[C_D] = 1.0, and the results are shown in Figure 2.12. The unmagnified data residual is still quite small but the model error is considerably larger. Again the error is smallest for V_p, followed by density and V_s as expected, but the V_s profile has deviated only negligibly from the starting model. Therefore even for a noiseless synthetic an expected level of noise causes the algorithm to honor the starting V_s to such a degree that it is only negligibly changed. This is not consistent with the resolution matrix shown in Figure 2.7 which suggests that V_s is the best resolved quantity. The reason for this discrepancy is unknown.

NOISY DATA

When diag[C_D] is kept at 1.0 and actual noise is added to the problem a similar result is obtained, (Figure 2.13). The data were made noisy by adding to each x-t datum a number whose magnitude had an equal probability of being between ± 5% of the largest value in the noise free data set. This corresponds to diag[C_D] ~1.0 The data then underwent all the preprocessing needed (see chapter 3) to yield a set of τ-p "observed" data with mostly random, but some coherent noise. The wavelet was assumed to be known. Note the increased model and data residuals of Figure 2.13 compared to Figure 2.12. However, virtually all of the reflection events have been modeled and only random noise and traces of coherent noise are left over from the pre-processing. This shows that for this expected noise level, (diag[C_D]) nothing further can be obtained from these data.

FREQUENCY GAP

The wavelet used in these tests contains frequencies from 5 to 65 Hz. In the previous tests the model variations < 5 Hz were given to the algorithm in the starting

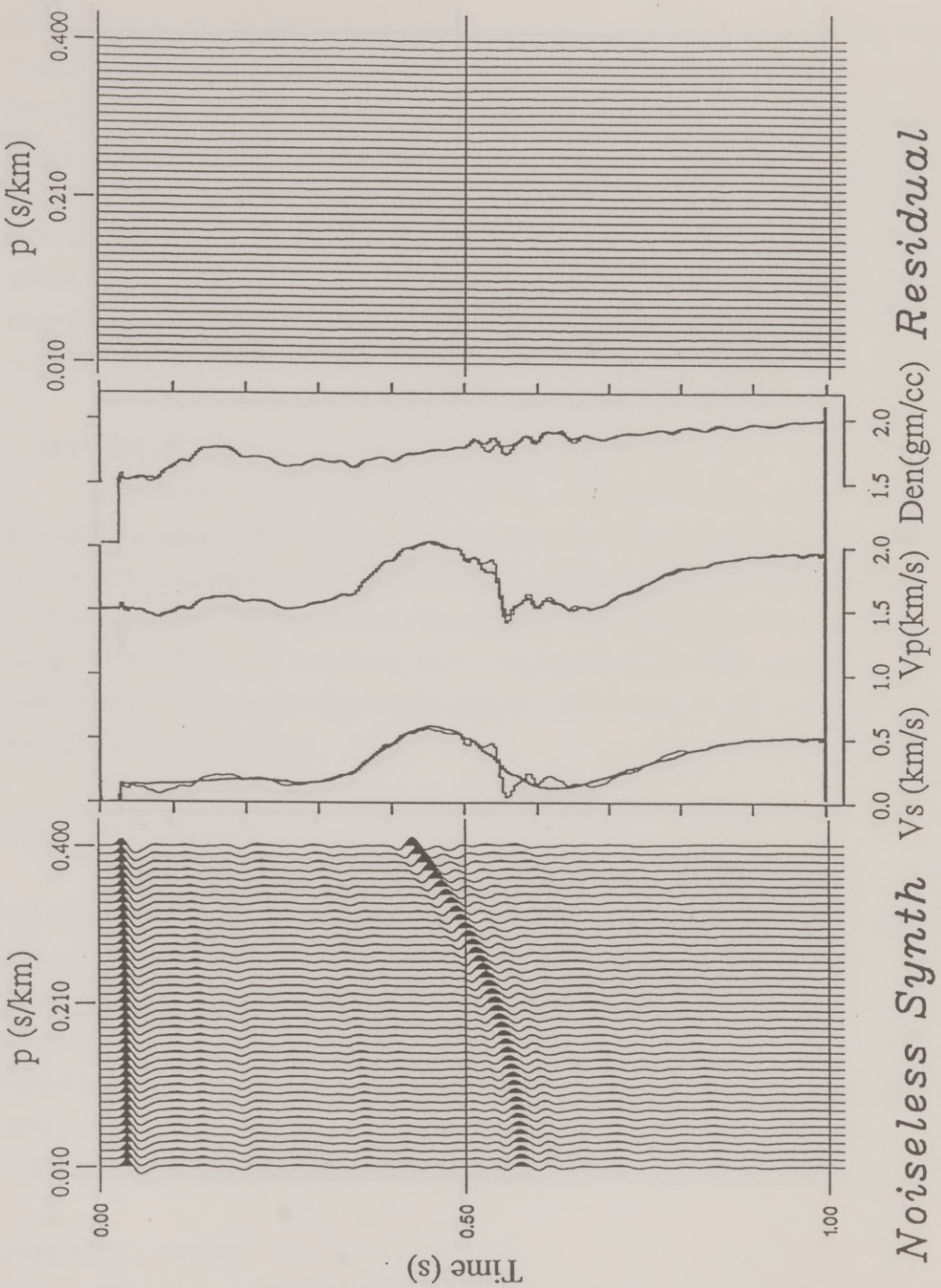

Figure 2.12. This test of the algorithm assumes diag[C_D] = 1.0. Note the accurate modeling of the data without full recovery of V_S. The V_S result, (bold) has hardly deviated form the starting value.

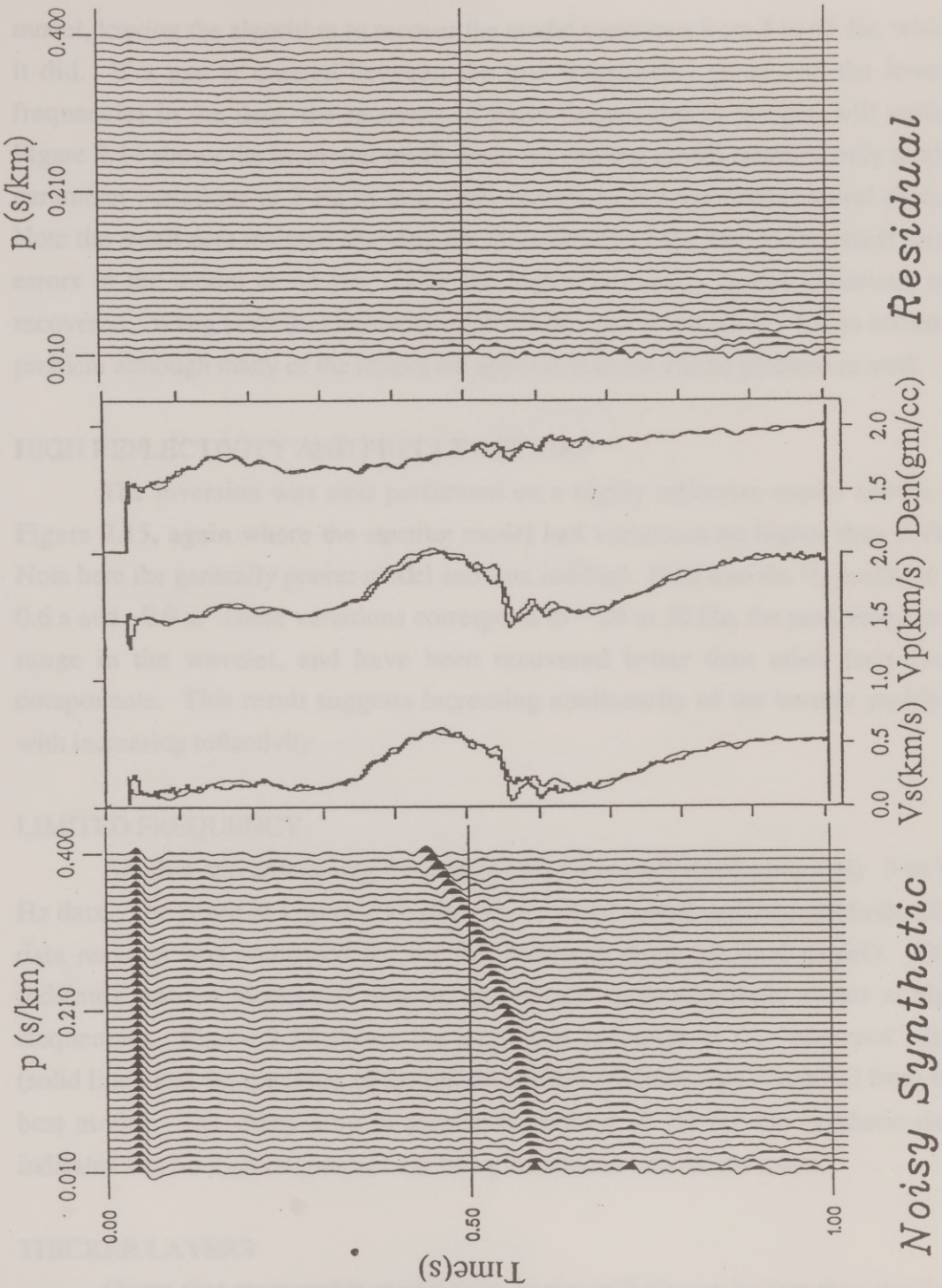

Figure 2.13. Similar to Figure 2.12 except that noise has been added to the data. Note the poorer model result (bold) while the data residual is still virtually free of reflection events.

model, leaving the algorithm to recover the model variations from 5 to 65 Hz, which it did. If a gap is created between the low frequencies given and the lowest frequencies in the data, the recovery of those frequencies in the gap will suffer. Figure 2.14 shows the inversion result when the starting model contains only model parameter variations of 2 Hz or less, (still enough to provide correct travel times). Note the small data residual showing the insensitivity of the data to the rather large errors in the model at ~3 Hz. Only the higher frequency model variations are recovered. Wang (1990) extensively explores this gap in sensitivity for an acoustic problem although many of the results are applicable to the elastic problem as well.

HIGH REFLECTIVITY AND FREQUENCY GAP

The inversion was next performed on a highly reflective model shown in Figure 2.15, again where the starting model had variations no higher than 2 Hz. Note here the generally poorer model and data residual. Note also the V_p profile at ~ 0.6 s and ~0.9 s. These variations correspond to ~ 20 to 30 Hz, the peak frequency range in the wavelet, and have been recovered better than other frequency components. This result suggests increasing nonlinearity of the inverse problem with increasing reflectivity.

LIMITED FREQUENCY

Another test concerning frequency range was performed using only 5 to 35 Hz data. The result in Figure 2.16 shows very small model and data residuals, (the data residual was computed for the full bandwith from the final model). This indicates that the model and data do not contain large amplitude events at high frequencies. Figure 2.17 shows the amplitude spectrum of the "observed" data (solid line), and the spectrum of the full bandwidth synthetic data computed from the best model. The sharp drop in amplitude beyond 35 Hz for the synthetic data indicates that no high frequencies are being introduced into the inversion.

THICKER LAYERS

Given that recoverable model frequencies will always be less than the data pass band, it makes little sense to parameterize the model such that higher frequencies

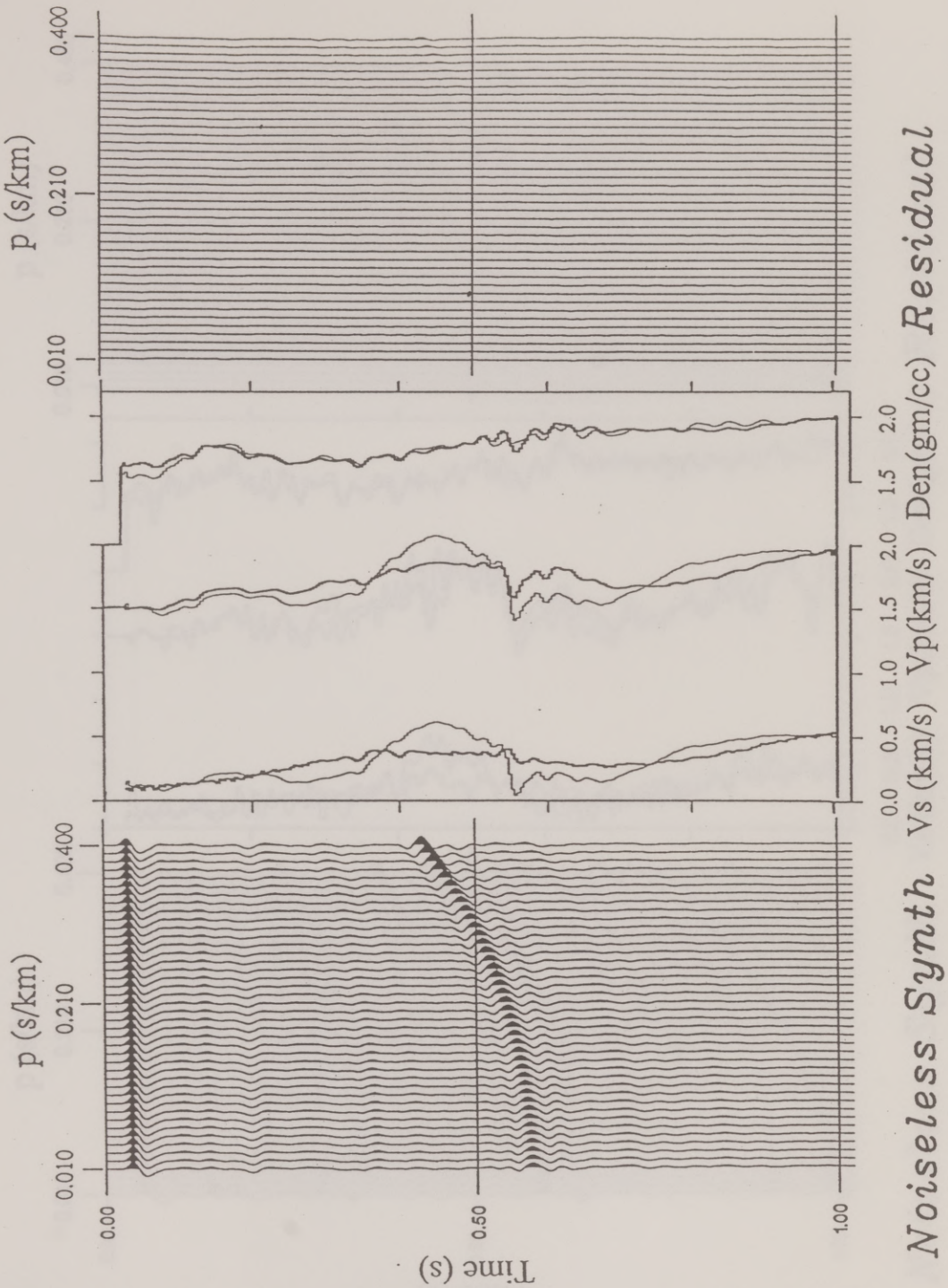

Figure 2.14. This result was obtained by using a starting model with variations in two way V_p time of less than 2.0 Hz. Note the large, 3 Hz model residual, (estimate:bold, true:fine) and the relatively small data residual showing the insensitivity of the data to these model frequencies.

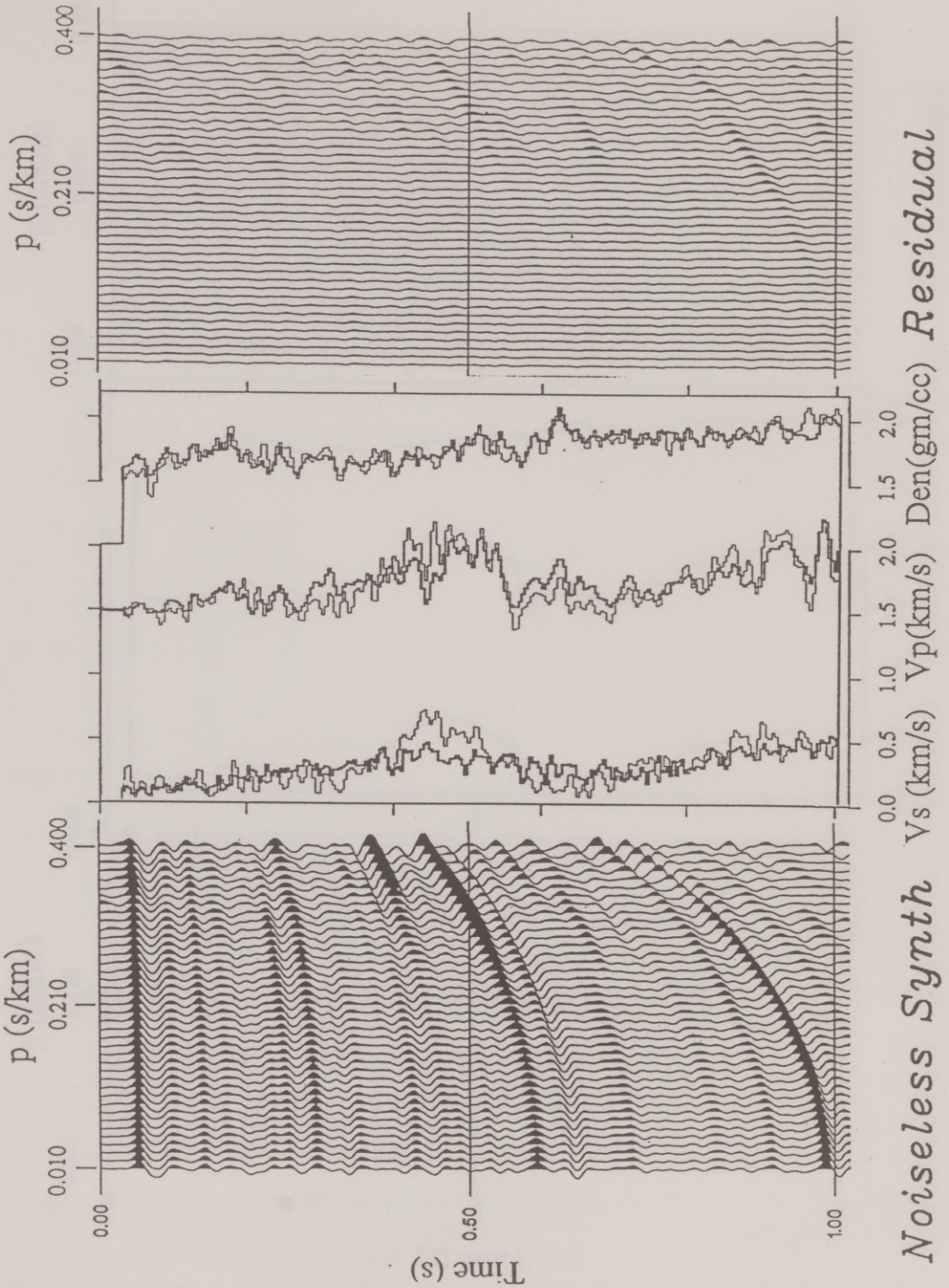

Figure 2.15. The inversion performance is degraded further when the true model is highly reflective in addition to the starting model being insufficient. Although the data residual is much smaller than the data, much of the model has not been recovered.

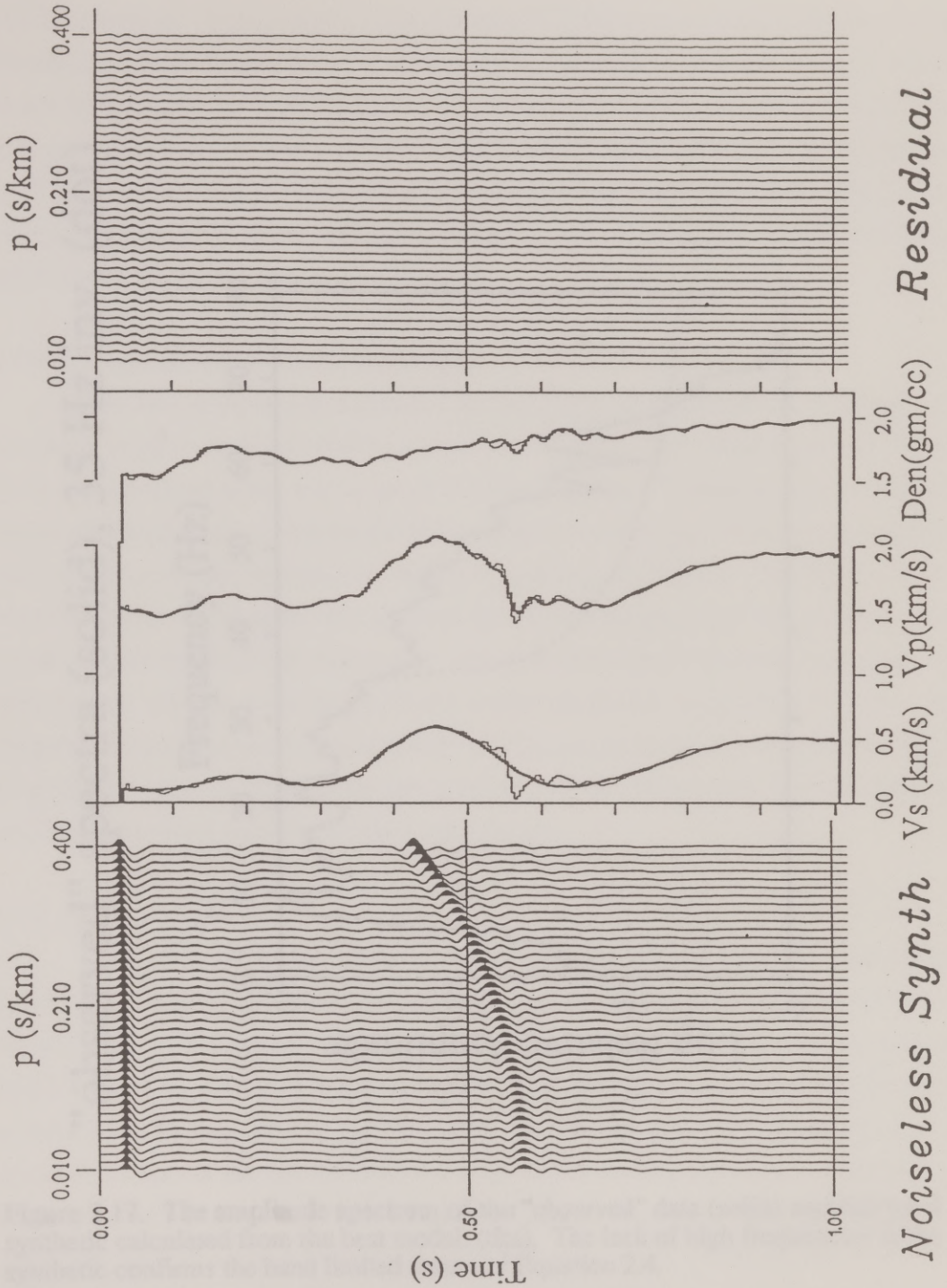

Figure 2.16. If only part of the data bandwith is used results are good but incomplete. High frequencies in the residual correspond to high frequencies in the model which have not been recovered.

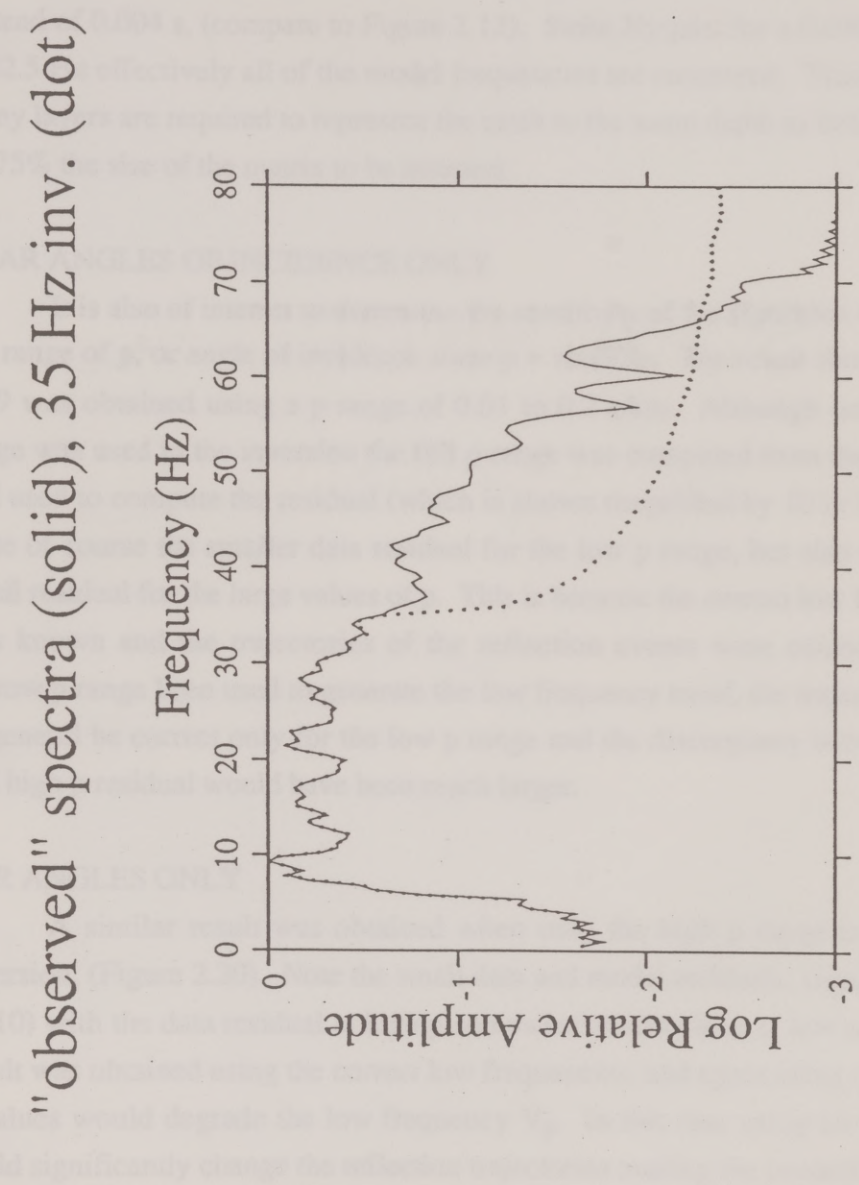

Figure 2.17. The amplitude spectrum of the "observed" data (solid) and full band synthetic calculated from the best model, (dot). The lack of high frequencies in the synthetic confirms the band limited nature of Equation 2.4.

can be obtained. It does make sense, however, to try to maximize the recoverable frequencies while minimizing the number of layers. Figure 2.18 shows an inversion result for an earth in which the layers were taken to be 0.008 s thick in P-wave time instead of 0.004 s, (compare to Figure 2.12). Since Nyquist for a 0.008 sample rate is 62.5 Hz effectively all of the model frequencies are recovered. Thus only half as many layers are required to represent the earth to the same depth as before, reducing by 75% the size of the matrix to be inverted.

NEAR ANGLES OF INCIDENCE ONLY

It is also of interest to determine the sensitivity of the algorithm to changes in the range of p, or angle of incidence since $p = \sin(\theta)/v$. The result shown in Figure 2.19 was obtained using a p range of 0.01 to 0.2 s/km. Although only the low p range was used in the inversion the full p range was computed from the final model and used to compute the residual (which is shown magnified by 10 in Figure 2.19). Note of course the smaller data residual for the low p range, but also a reasonably small residual for the large values of p. This is because the correct low frequency V_p was known and the trajectories of the reflection events were correct. Had this narrow p range been used to generate the low frequency trend, the trajectories would in general be correct only for the low p range and the discrepancy between the low and high p residual would have been much larger.

FAR ANGLES ONLY

A similar result was obtained when only the high p range is used in the inversion, (Figure 2.20). Note the small data and model residuals, (again multiplied by 10) with the data residual at high p somewhat smaller than at low p. Again this result was obtained using the correct low frequencies, and again using only the high p values would degrade the low frequency V_p. In this case using an incorrect V_p could significantly change the reflection trajectories making the inversion difficult if not impossible. However, for the correct background V_p, an inversion performed on either the large or small incidence angle data yields a result similar to that when the full angle reange is used, (Figures 2.12, 2.19, and 2.20).

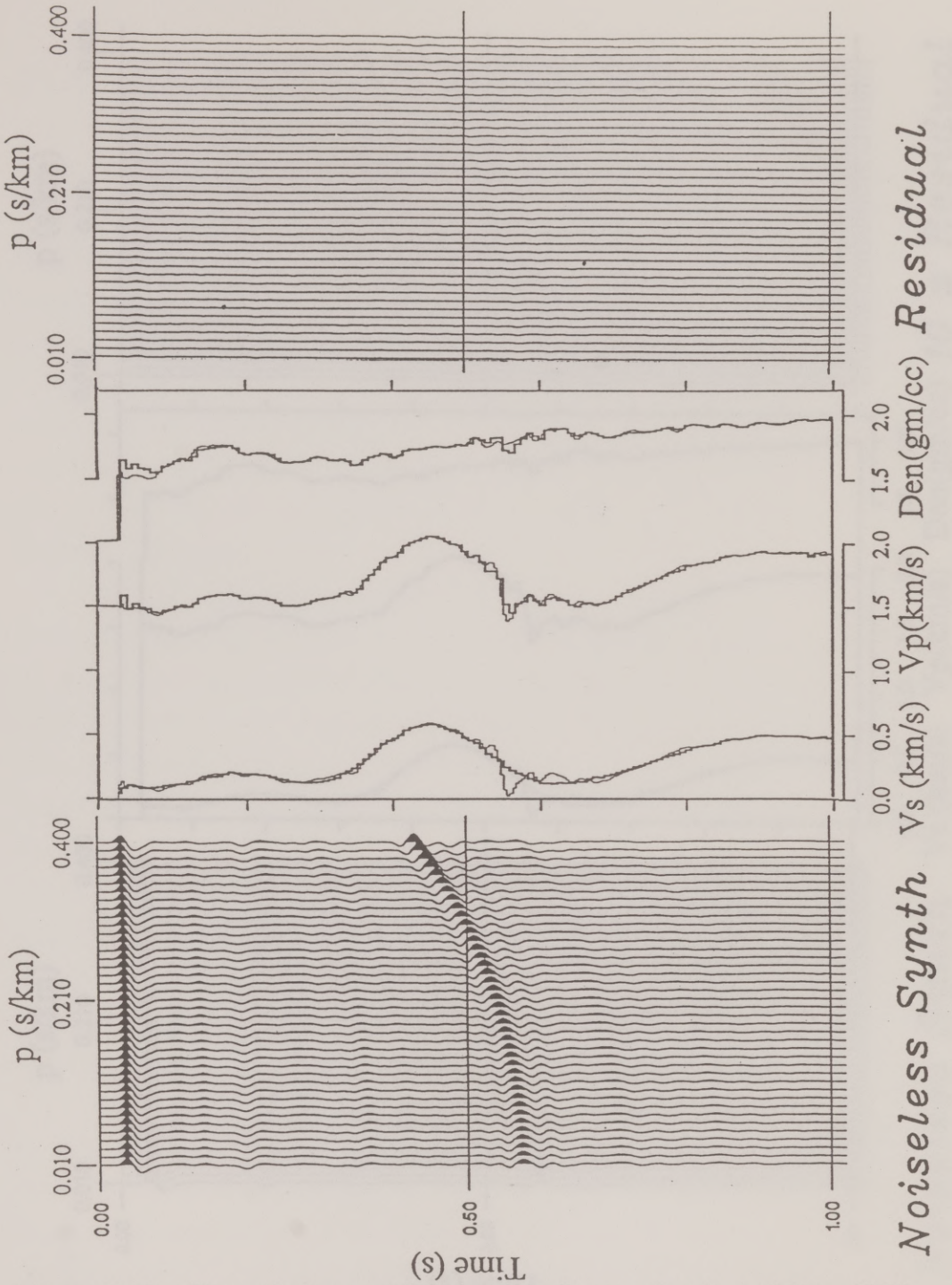

Figure 2.18. Since the true model contains frequencies from 0.0 to 65 Hz, a sampling of 0.008 s should be largely adequate. For the result shown here the layer thicknesses have been set to a P-wave travel time of 0.008 s, reducing the number of model parameters by one half. Compare data and model residuals to those in Figure 2.12.

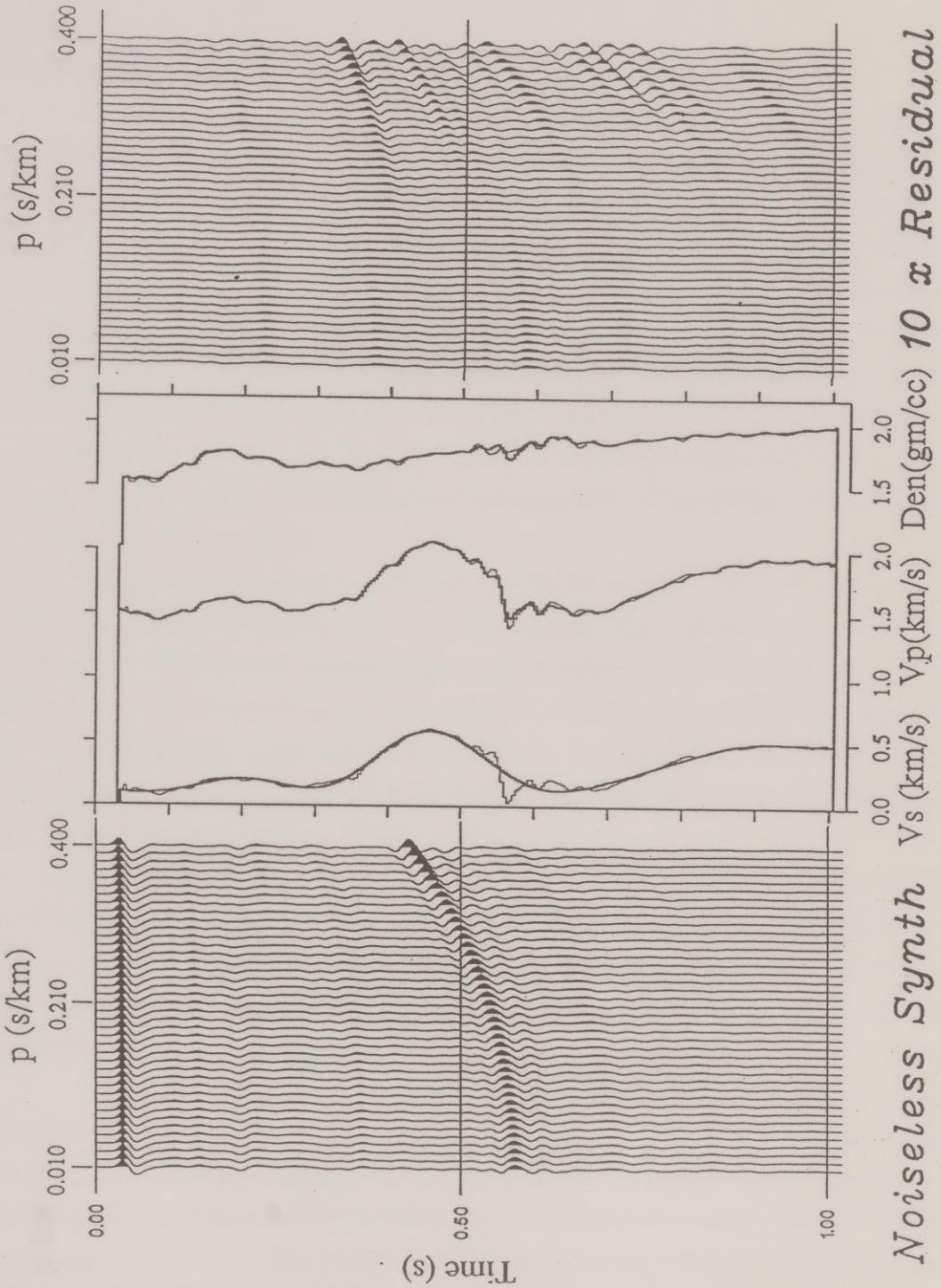

Figure 2.19. When only data from p = 0.01 to 0.2 s/km is used the model is still well recovered, (compare with Figure 2.11). The full p range synthetic data computed from the best model were used to compute the data residual. Note the better fit at p < 0.2 s/km.

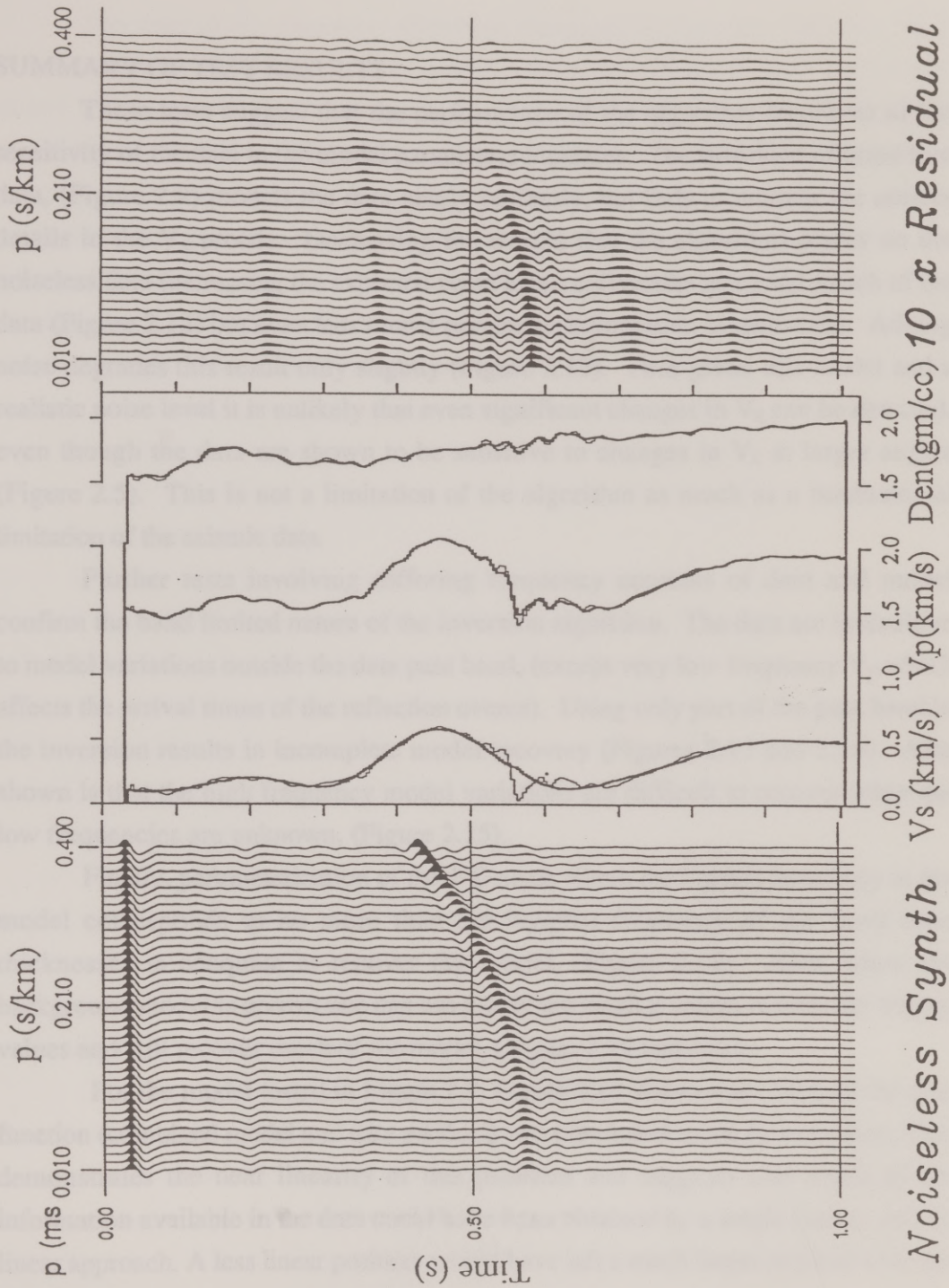

Figure 2.20. This shows the inversion result when only the far p range (0.2 to 0.4 s/km) is used. Note the better fit at high p, and good recovery of V_p and density. In both Figures 2.18 and 2.19 the correct backround model was given.

SUMMARY OF TEST RESULTS

These tests suggest that the performance of the algorithm improves as the sensitivity of the data to the model parameters increases. The inversion of noise free data, (Figure 2.9) models the data nearly perfectly, but fails to recover the correct details in the V_S profile. Decreasing the weight that the algorithm places on the noiseless data (increasing the expected noise level) still results in a good match of the data (Figure 2.12) but even less model parameter information is recovered. Adding noise degrades this result only slightly (Figure 2.13). Thus given this model and a realistic noise level it is unlikely that even significant changes in V_S can be detected, even though the data are shown to be sensitive to changes in V_S at larger angles (Figure 2.5). This is not a limitation of the algorithm as much as a fundamental limitation of the seismic data.

Further tests involving differing frequency contents of data and model confirm the band limited nature of the inversion algorithm. The data are insensitive to model variations outside the data pass band, (except very low frequency V_p which affects the arrival times of the reflection events). Using only part of the pass band in the inversion results in incomplete model recovery (Figures 2.15 and 2.16). Also shown is that the high frequency model variations are difficult to recover when the low frequencies are unknown, (Figure 2.15).

Finally, parameterization of the 1-D earth where the highest frequency in the model corresponds to no more than the Nyquist frequency of the layer time thicknesses is adequate to recover the model, (Figure 2.18). Also, when the background model is correct one can use a only the small p values or only the large p values and still recover much of the model, (Figure 2.19 and 2.20).

For the model tested in Figure 2.9, Figure 2.10 shows that ~99% of the cost function (combined model and data residual) was eliminated in the first iteration. This demonstrates the near linearity of this problem and suggests that much of the information available in the data could have been obtained by a single iterate, strictly linear approach. A less linear problem would have left a much larger residual after the first iterate.

The tests of the inversion algorithm discussed above show that to a large extent the algorithm will find a model which matches the data quite well. Figure 2.10 shows that However, it is only when the expected noise level is very low that significant portions of the V_S profile can be recovered. It is therefore important to remove or model the noise to a much greater extent than necessary in the conventional processing of seismic data. Also, the algorithm assumes, that the "observed" data input is infinite aperture plane wave data, but actual field data cannot be acquired in this form. It must therefore undergo a plane wave decomposition, discussed in the next chapter.

Chapter 3
Inversion of Carolina Trough Data

Although the results in Chapter 2 suggest incomplete resolution at realistic noise levels the technique may still be useful in answering specific geologic questions. This application requires very careful preparation of the data and is examined here in detail for the Carolina Trough data mentioned earlier (Figure 1.2), although the procedures are similar for the data from Nankai Trough.

Geologic Objective

For sediments at the water depth of CMP1602 pressure and temperature conditions are favorable for the formation of ice like crystalline gas/water hydrates, also called gas hydrates. The hydrates are found in the upper few hundred meters of the sedimentary section and have been sampled directly in other parts of the world, (Shipley and Didyk, 1982; Mathews and von Huene, 1985). The sharp acoustic impedance contrast between a high velocity hydrate and either low velocity, gas charged sediments or just normal non-hydrated sediment below, make the bottom of the hydrate stability zone detectable as a bottom simulating reflector (BSR) in seismic data. The chief component gas of the hydrates is methane, present in excess of 98%, (Claypool and Kaplan, 1974; Kvenvolden, 1984) making them of interest to hydrocarbon explorationists as well as environmentalists concerned with a large methane release in the event of submarine slumping. Objectives of this study include quantifying the amount of methane present and determining the exact nature of the impedance contrast which makes up the BSR by inverting seismic waveform data from a CMP gather in this area.

Corrections for Non-Ideal Acquisition

The inversion algorithm discussed previously requires that the observed data, $\mathbf{d}_{obs}$ be plane wave decomposed data, presumably acquired with point sources and equi-spaced, equally sensitive, horizontal, collinear, point receivers. Because of slight irregularities in even state of the art acquisition of seismic data, it must be

modified so that the deviations from this ideal geometry do not adversely affect the inversion result. Some of these irregularities cause artifacts which are easy to remove from the data. Others are easier to model as part of the inversion process. In either case failure to account for these effects degrades the best possible fit between observed and synthetic data and will likely degrade the resulting model. This pre-processing of the data consists of several statics and amplitude adjustments before and after the data are transformed to the plane wave domain. The processing is summarized in flow chart form in the Appendix. The estimation of the angle dependent source wavelet is also discussed.

FILTERING, STATICS

The first step is to determine the frequency range of interest. Figure 3.1 shows the normalized amplitude spectrum of the raw data averaged over 240 traces each with 2048, 0.004 s samples. To minimize the numbr of frequencies used in the inversion only the strongest amplitudes were retained. Data with amplitudes more than 20 db down from the maximum were not used, so the pertinent frequency range for this data is from 5 to 65 Hz.

The statics corrections to the data are small and can be easily made. Figure 3.2 (upper) shows the water bottom reflection (at 0.04 s) after application of a moveout correction which should make it flat and horizontal. Note the significant deviations from horizontal due to acquisition effects such as feathering, varying streamer depths, electronic delays as well as from slight sea floor dip. Similar statics problems and their elimination are discussed extensively by Stark (1986). To correct for these deviations the traces are multiplied in the frequency domain (to maintain regular time samples) by $\exp[i\omega\Delta t]$ where Δt is the delay needed to make the water bottom reflection horizontal. The result for the water bottom is shown in Figure 3.2 (lower), although reflections throughout the section were also substantially improved. Failure to make these corrections results in a non elliptical trajectory when the data are decomposed into plane waves and a degraded data fit.

AMPLITUDE CORRECTIONS

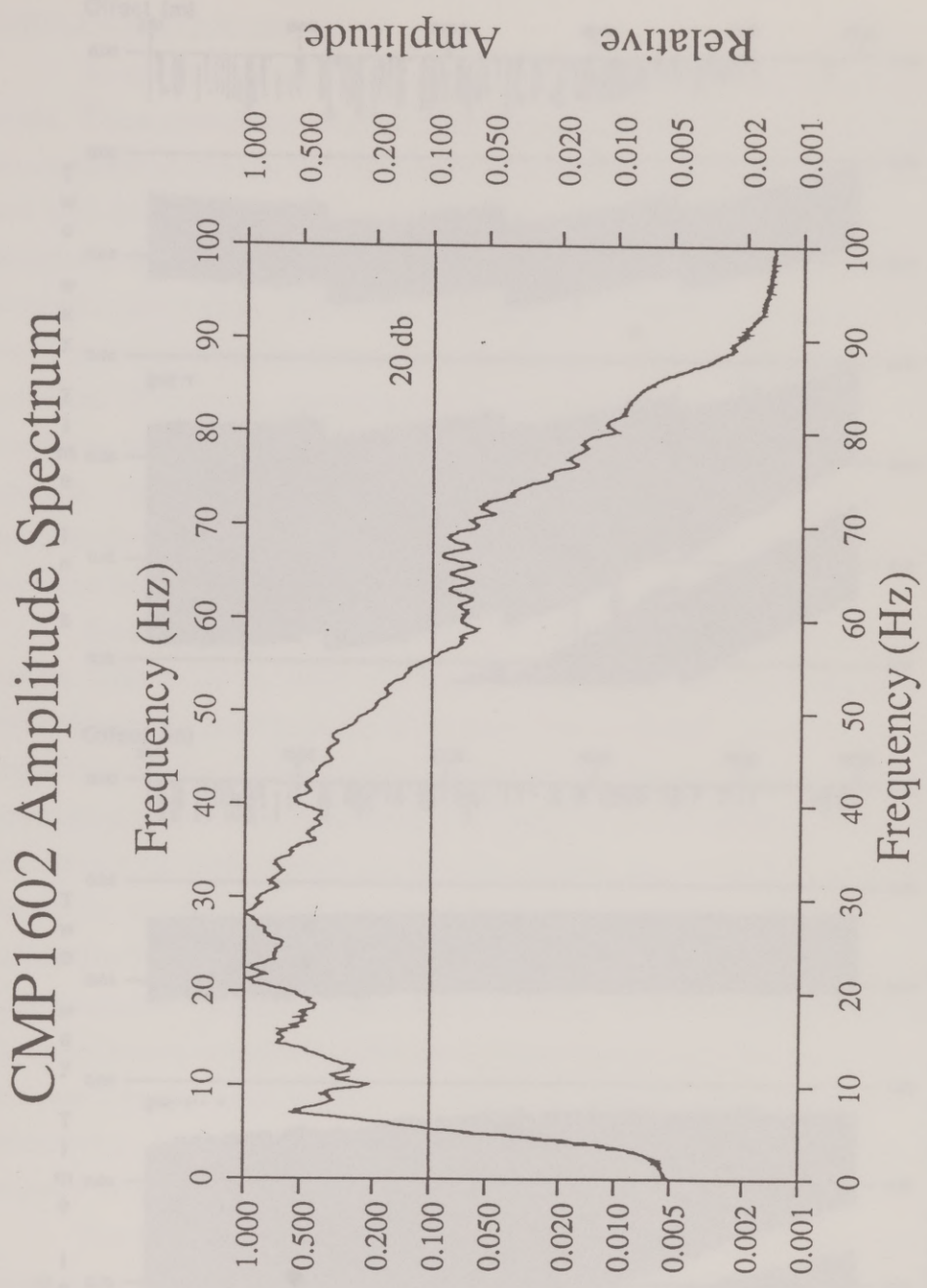

Figure 3.1. This is the normalized amplitude spectrum of CMP1602 prior to filtering. Frequencies below 5 Hz and above 65 Hz are assumed to dominated by noise.

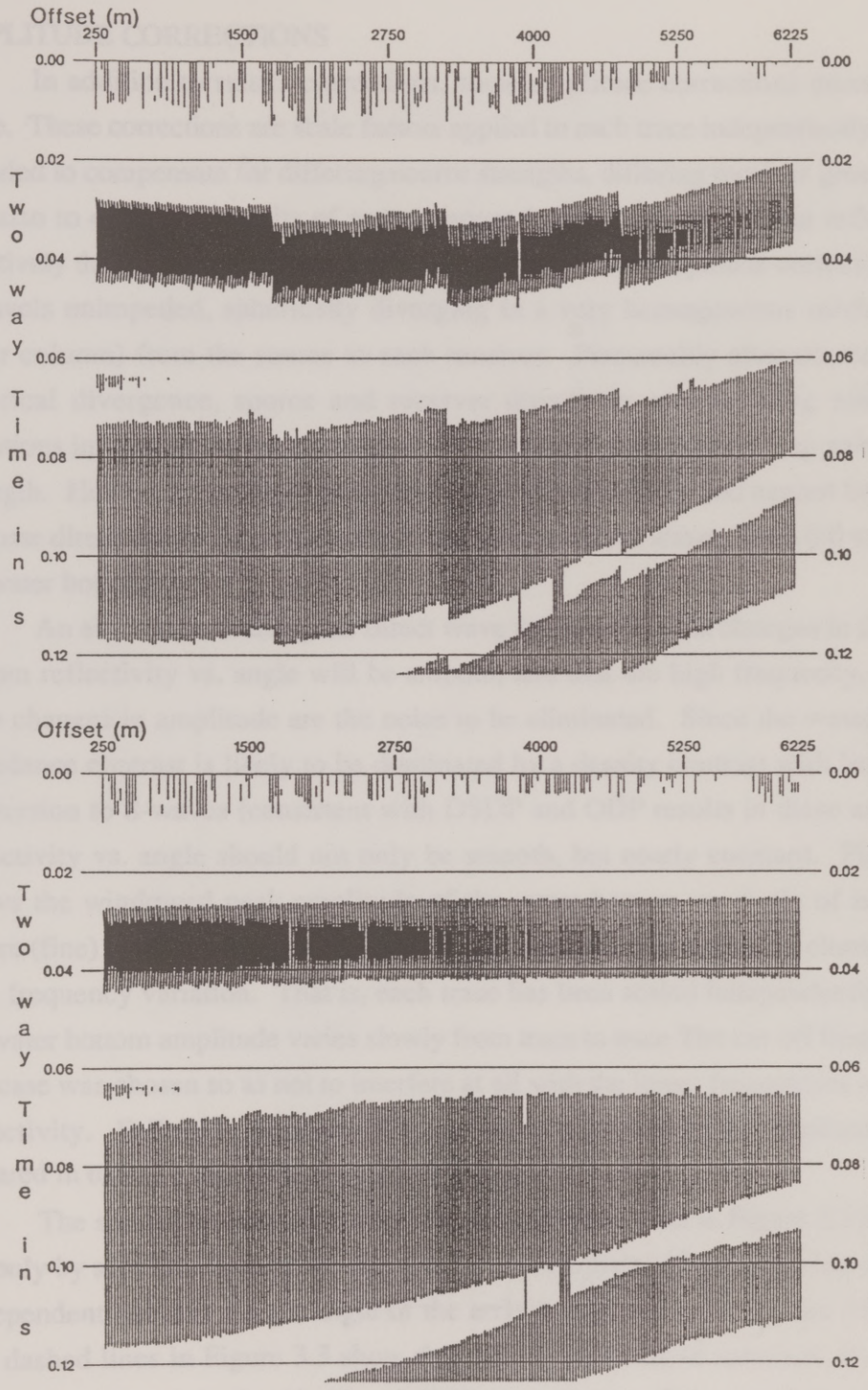

Figure 3.2. This is water bottom reflection in CMP1602 at an expanded time scale before (upper) and after (lower) statics corrections to reconcile small static shifts due to various small positioning errors. The result is improved reflection trajectories which result in more accurately modeled events.

AMPLITUDE CORRECTIONS

In addition to statics corrections, some amplitude corrections must also be made. These corrections are scale factors applied to each trace independently and are intended to compensate for differing source strengths, differing receiver group gains, and also to convert the units of measurement (typically millivolts) to reflectivity. Intuitively the direct wave seems a good candidate for this amplitude correction since it travels unimpeded, spherically diverging in a very homogeneous medium (the water column) from the source to each receiver. Presumably after correction for spherical divergence, source and receiver directivity and ghosting effects the variations in the amplitude represent actual variations in receiver group gain or shot strength. However, the direct wave travels only horizontally and cannot be used to estimate directivity at the angles of the incoming reflected waves, from 0.0 to ~55° at the water bottom.

An alternative to using the direct wave is to assume that changes in the water bottom reflectivity vs. angle will be smooth, and that the high frequency, trace to trace changes in amplitude are the noise to be eliminated. Since the water bottom impedance contrast is likely to be dominated by a density contrast with little or no conversion to S-waves (consistent with DSDP and ODP results in these areas) the reflectivity vs. angle should not only be smooth, but nearly constant. Figure 3.3 shows the windowed peak amplitude of the water bottom vs. angle of incidence before (fine) and after (bold) a trace amplitude smoothing operation to eliminate this high frequency variation. That is, each trace has been scaled independently so that the water bottom amplitude varies slowly from trace to trace The cut off frequency in this case was chosen so as not to interfere at all with the lower frequencies related to reflectivity. Failure to perform this correction again results in amplitude errors smeared in ω and p, degrading any fit of $\mathbf{d}_{obs}$.

The significant decrease in amplitude with offset seen in Figure 3.3 is caused not only by spherical divergence but also by the directivity of the receiving array and is dependent not only on the angle of the arriving wave but also on the frequency. The dashed lines in Figure 3.3 show the combined effects of spherical divergence and receiver directivity for 10, 30 and 60 Hz components. Because of this effect, as

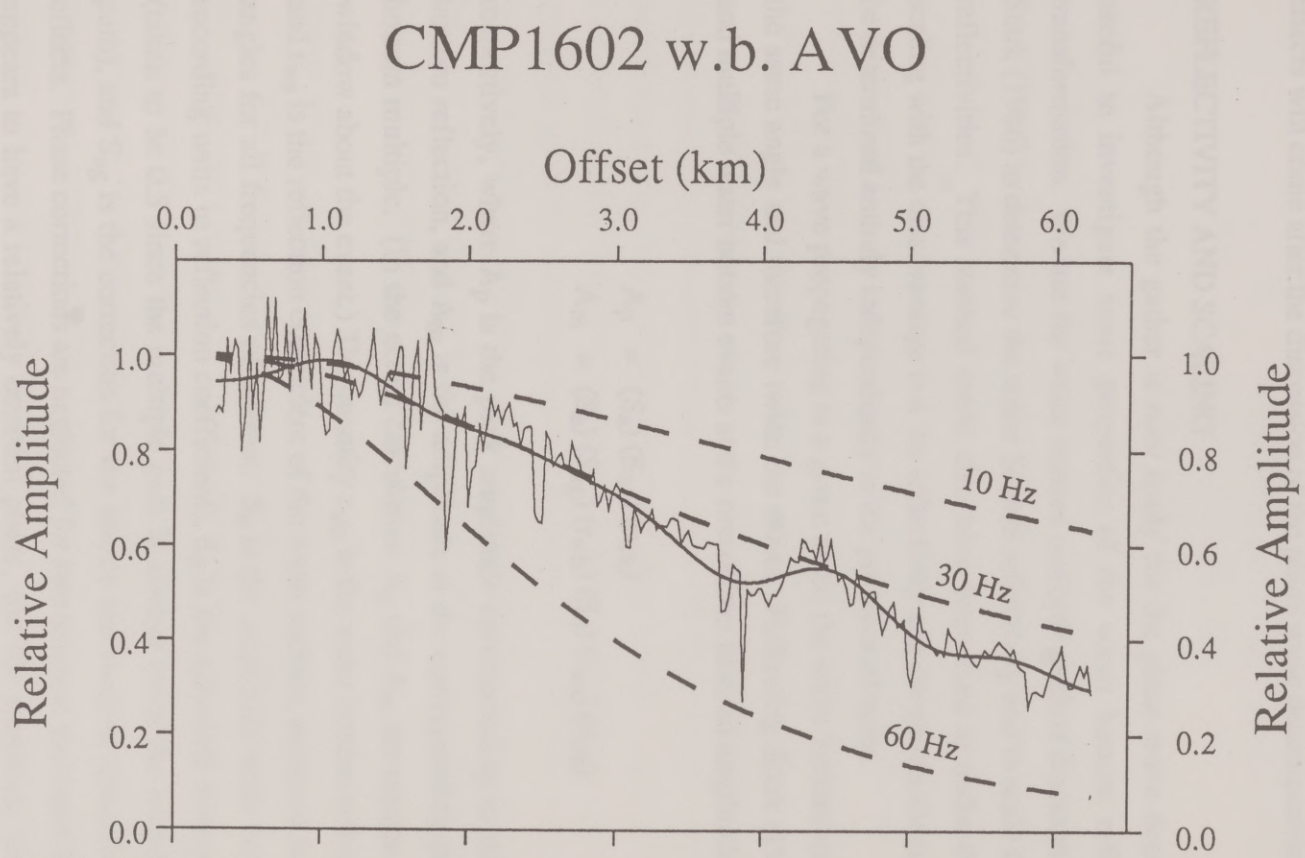

Figure 3.3. Amplitude of the water bottom event before (fine solid) and after (bold solid) individual trace scaling to ensure a smooth reflectivity variation with offset. The dashed lines show the decrease in amplitude with offset expected for a combination of spherical divergence and receiver array directivity for 10, 30, and 60 Hz.

well as the effects of source directivity and ghosting, is a simpler function of p and ω (plane wave domain variables) than of x and t, the discussion of the nature of these effects will come after the discussion of the plane wave decomposition (PWD).

REFLECTIVITY AND SCALING

Although the gather is now ready for the plane wave decomposition it is useful to investigate some properties of the water bottom reflection prior to transformation. We use the water bottom multiple method discussed extensively by Stark (1986) to determine the water bottom reflectivity and to scale the amplitudes to reflectivities. This method could also have been used to make the trace to trace scaling with the disadvantage that the reflectivity and the amplitude corrections cannot be determined entirely independently in the presence of noise.

For a wave propagating at a given angle the water bottom multiple arrives at the same angle and therefore twice the offset. Following Stark (1986) the primary and multiple water bottom events at the two offsets have an amplitude given by

$$A_p = (S_a)\,(S_{ag})\,(r_{wb})$$
$$A_m = (S_a)\,(S_{ag})\,(r_{wb})\,(S_d)\,(r_{ws})\,(r_{wb})$$

respectively, where A_p is the peak amplitude corresponding to the primary water bottom reflection, and A_m is the amplitude at the corresponding peak in the water bottom multiple. (In the actual calculation A_p and A_m are computed over a small window about the event.) The quantity r_{wb} is the water bottom reflection coefficient, and r_{ws} is the reflection coefficient of the water surface, assumed here to be -1 at all angles for all frequencies of interest. S_a is the amplitude scale factor, (converting recording units to reflection coefficient), S_d is the spherical divergence correction, (taken to be 0.5 since the multiple path is always twice the length of the primary path), and S_{ag} is the correction for the source and receiver directivity and ghosting effects. Phase corrections are neglected for two reasons; the water bottom reflection appears to have a relatively constant phase, and the amplitude measurements are taken over a time window which mitigates the effect of phase changes.

Given these definitions the value of r_{wb} is then given by

$$r_{wb} = A_m / (S_d\ r_{ws}\ A_p) = (-2\ A_m) / A_p$$

so

$$\begin{aligned} S_a &= A_p / (S_{ag}\ r_{wb}) = A_p / [S_{ag}\ A_m / (S_d\ r_{ws}\ A_p)] \\ &= S_d\ r_{ws} A_p^2 / (S_{ag}\ A_m) \\ &= -A_p^2 / (2 S_{ag}\ A_m) \end{aligned}$$

Note that the scale factor S_a is dependent on the source and receiver directivity and ghosting which is in turn dependent on the angle and frequency of the incident wave. This indicates that before the data amplitudes can be scaled to those of their corresponding reflection coefficients, the acquisition geometry must be properly modeled. The water bottom reflection coefficient, however, is independent of S_{ag} and is shown in Figure 3.4 for each primary/multiple pair available. Here $r_{wb} = 0.21 \pm 0.02$, which is expected and geologically reasonable.

Another byproduct of this water bottom multiple exercise is a check for static time delays in the recording, which may introduce depth errors in later analyses if not handled properly. The time between the primary and the multiple is the time needed to travel from the receiver array, up to the water surface, down to the water bottom, and back up to the receiving array. This may not be exactly twice the time of the primary because of differences in depth between the source and receiver, or time delays in the recording apparatus. For CMP1602 a time delay of 0.04 s (probably a time delay in the recording) corrects the gather.

Plane Wave Decomposition

The next step in the preparation of the data in the plane wave decomposition. The plane wave decomposition can be performed by applying a Fourier Bessel transform or equivalently, a cylindrical slant stack (Brysk and McCowan 1986a). However, the application of infinite range integral transforms to finite, sampled data will always generate artifacts. One source of these artifacts which is frequently ignored when working with synthetics is that caused by collecting the data with a finite length receiving array (Brysk and McCowan 1986b; Dobbs et al. 1990). When the target is deep compared to the array length (i.e. only narrow reflection angles

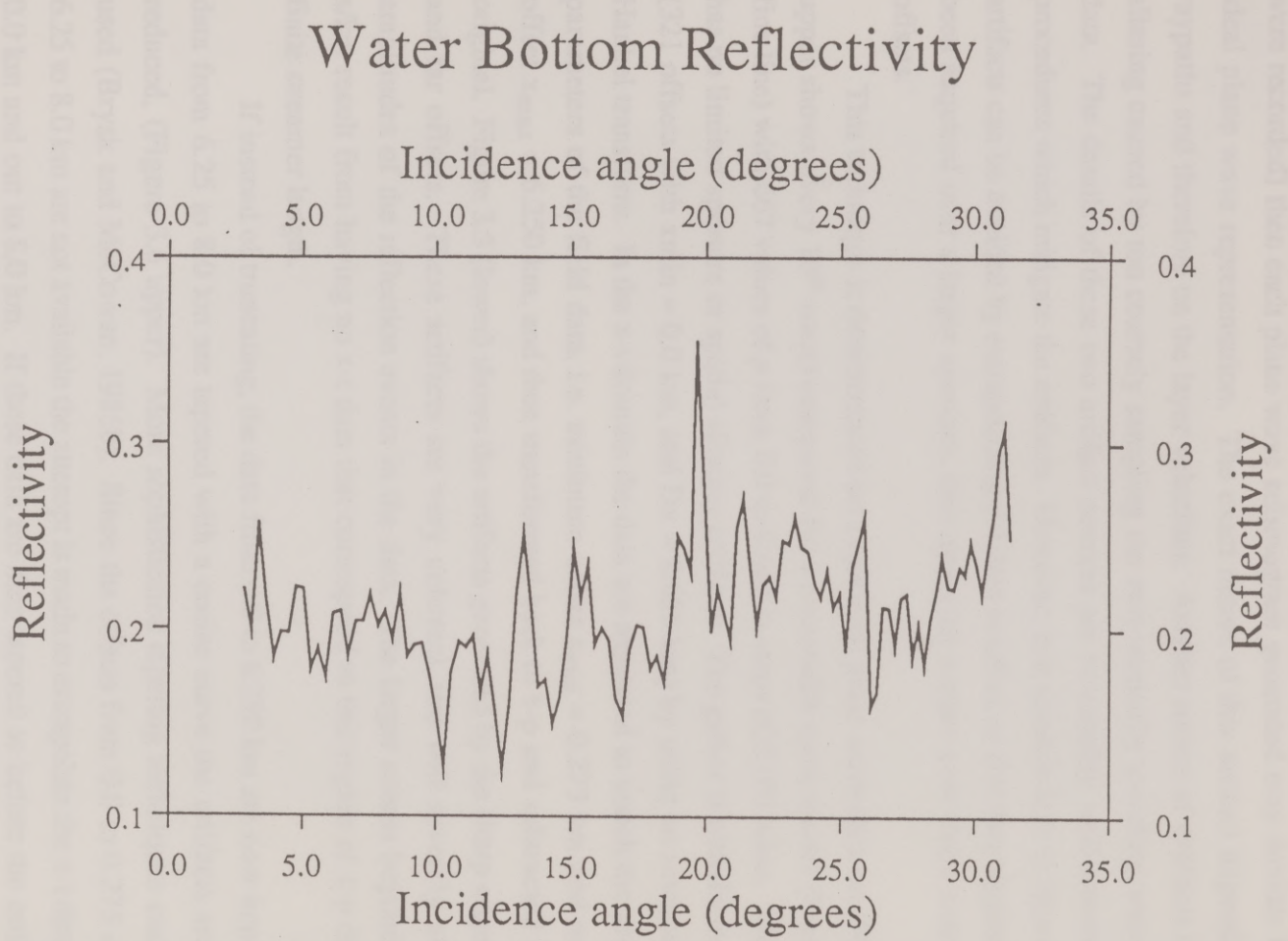

Figure 3.4. Reflectivity of the water bottom vs. angle of incidence for CMP1602. The average value is 0.21 ± 0.02 and is used to scale the final τ-p seismogram.

were recorded) then each plane wave seismogram generated may deviate from the ideal plane wave representation. The exact nature of this artifact depends on the raypaths and therefore on the layer velocities. Another source of artifacts is spatial aliasing caused by too coarsely sampling the non-vertically traveling waves in the data. The details of these two artifact sources are reasonably well known, as are procedures which mitigate the artifacts. However, it is suitable here to show that the artifacts can be avoided by extrapolating the data in offset so that they appear to have been acquired over a larger aperture, then applying a taper over these extrapolated offsets.

This technique is demonstrated on a synthetic plane wave data set (Figure 3.5 upper shows every 10^{th} trace) computed for a reasonable earth model (Figure 2.12, fine line) with 667 values of p from 0.0 to 0.666 in steps of 0.001 s/km. This gather has no limited aperture or spatial aliasing artifacts. The gather is transformed to x-t (321 offsets with xmin = 0.0 km, and Dx = 0.025 km) by using an inverse Fourier Hankel transform. In the x-t domain the data are truncated to match the acquisition parameters of the field data, i.e. minimum offset x_{min} = 0.275 km and maximum offset x_{max} = 6.250 km, and then transformed back to τ-p and subtracted from the original. Figure 3.5 (lower) shows the artifacts generated by the sharp edges at near and far offsets. These artifacts are very coherent and will severely affect the amplitudes of the reflection events in the data. The larger events beyond p = 0.5 s/km result from having no x-t data that correspond to this region of τ-p due to the finite streamer length.

If instead of truncating, the data from 0.0 to 6.250 km are now kept and the data from 6.25 to 8.0 km are tapered with a cosine curve the artifacts are greatly reduced, (Figure 3.6 upper). More sophisticated tapering techniques can also be used (Brysk and McCowan, 1986b). Since the offsets from 0.0 to 0.275 and from 6.25 to 8.0 km are not available the attempt is made to extrapolate the x-t data back to 0.0 km and out to 8.0 km. If these data are then tapered as before the artifacts are once again greatly reduced (Figure 3.6 lower). Thus for these acquisition parameters and model the extrapolation does not significantly affect the amplitudes of the reflection events for $p < \sim 0.4$ s/km.

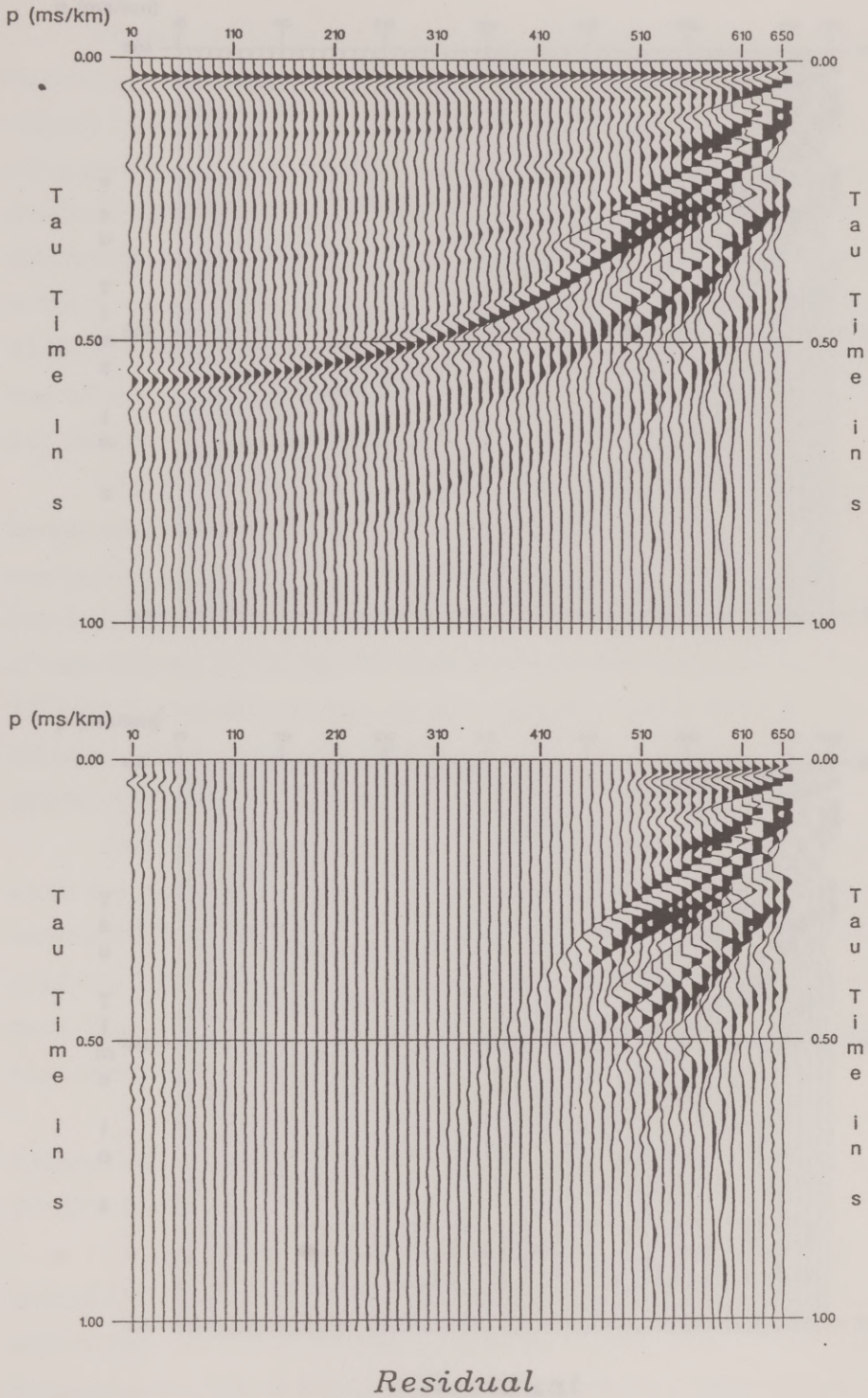

Figure 3.5. (upper) This synthetic data contains no noise or artifacts. When it is transformed to x-t, truncated to match the aperture length of CMP1602, then transformed back to τ-p and subtracted from the original, large coherent limited aperture effects result (lower).

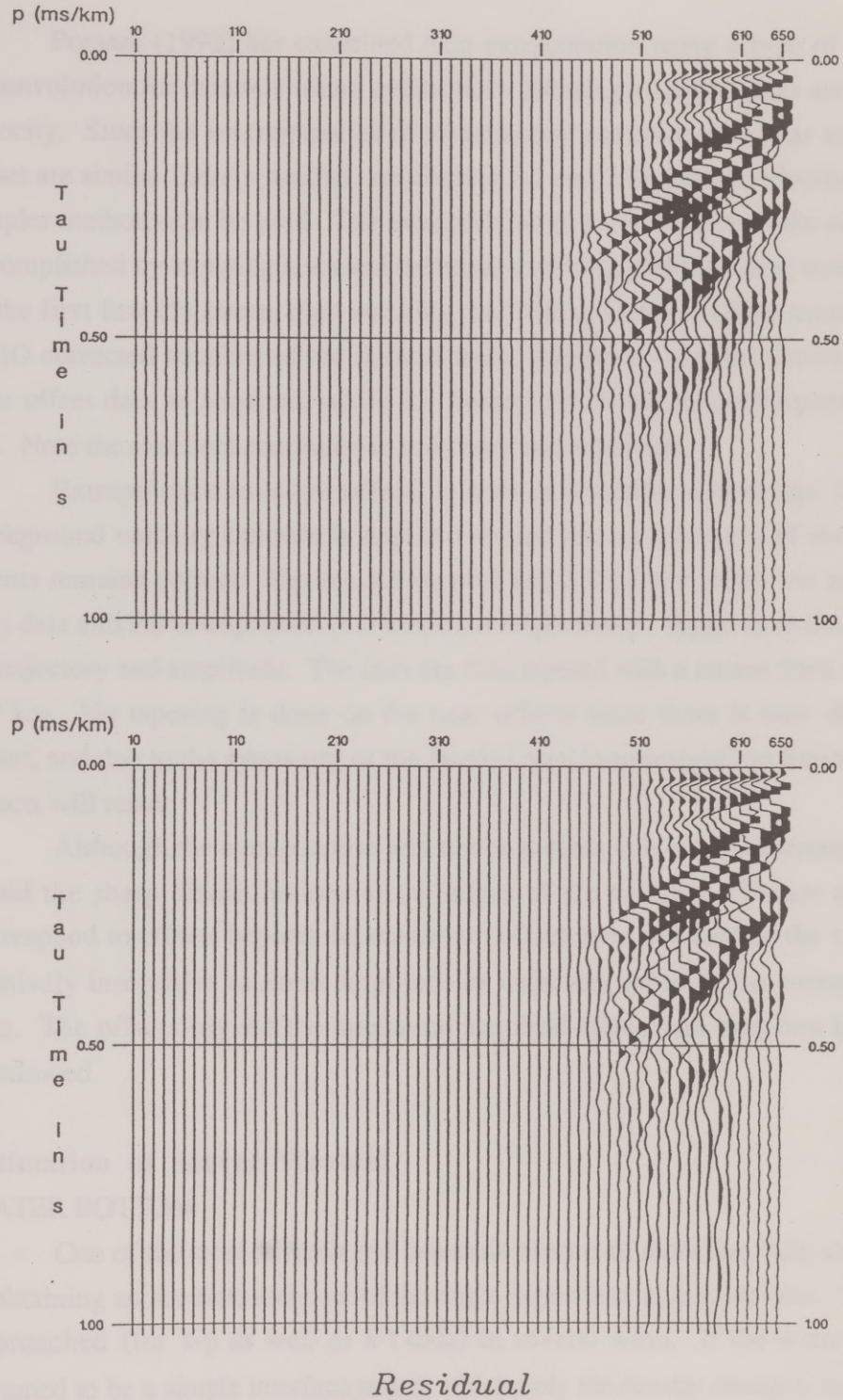

Figure 3.6. (upper) If the data could have been gradually tapered out to 8.0 km before transforming back to τ-p instead of truncated at 6.225 km the residual artifacts could be substantially reduced. Since this is not possible the data are extrapolated to 8.0 km and then tapered, yielding almost as good a result (lower) as if the data had been collected out to 8.0 km.

Porsani (1992) has examined data extrapolation using a type of predictive deconvolution for data sets where events have differing x-t trajectories and unknown velocity. Since the x-t trajectories of all reflection events at very near and very far offset are similar (nearly parallel, see Figures 3.7 and 3.8) and the velocity is known, simpler methods can be used. The extrapolation to zero offset from the minimum is accomplished by applying a normal moveout correction (NMO) using water velocity to the first few (5) traces, then stacking, and filling in the missing traces with the NMO corrected versions of the stacked trace. Figure 3.7 (upper) shows the actual near offset data as acquired, while 3.7 (lower) shows the data extrapolated to x = 0.0. Note the excellent continuity in trajectory and amplitude.

Extrapolation to larger offsets is done in a similar way except that a good background velocity estimate is required so that the x-t trajectory of the reflection events remains correct. Figures 3.8 (upper) and 3.8 (lower) show the actual (6.25 km) data and the extrapolated (8.0 km) data respectively. Again note the continuity of trajectory and amplitude. The data are then tapered with a cosine from 6.25 km to 8.0 km. No tapering is done on the near offsets since there is now data at zero offset, and due to the symmetry of the Hankel transform integral no limited aperture effects will result.

Although the extrapolation will not be perfect, it is most important to simply avoid the sharp discontinuities at the edges of the x-t data. Values of p which correspond to offsets beyond the maximum offset were not used so the τ-p data are relatively insensitive to small amplitude or trajectory errors in the extrapolated x-t data. The offsets beyond the maximum acquired offsets can therefore be severely windowed.

Estimation of Source Wavelet

WATER BOTTOM

One of the most difficult and uncertain aspects of modeling field seismograms is obtaining an accurate estimate of the angle dependent source wavelet. This can be approached (for τ-p as well as x-t data) in several ways. If the water bottom is assumed to be a simple interface across which only the density changes, then the

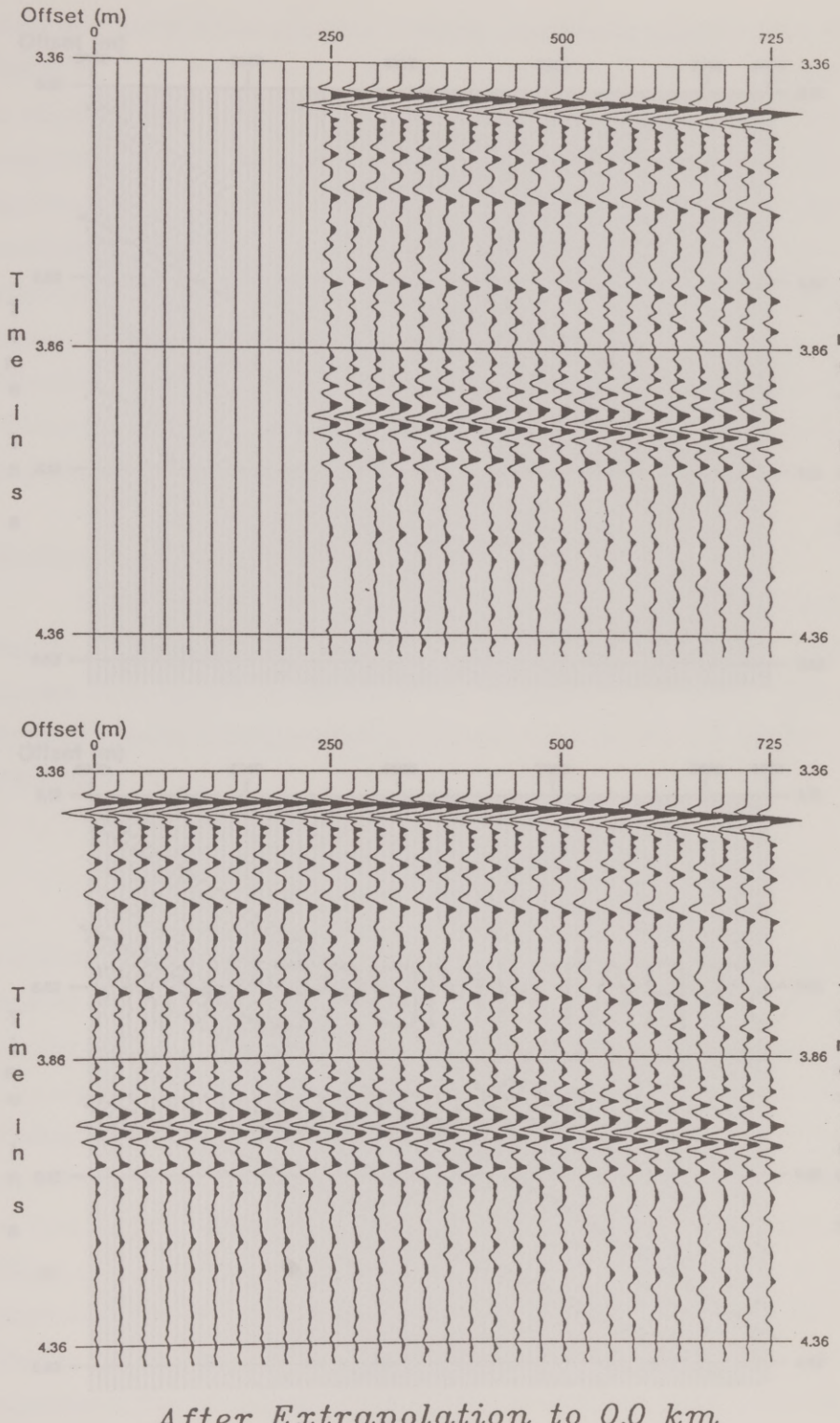

Figure 3.7. (upper) The extrapolation to near offsets is performed by NMO correcting the first 5 traces, averaging, and move out correcting the averaged trace individually for each missing offset. (lower) Note the continuity in trajectory and amplitude.

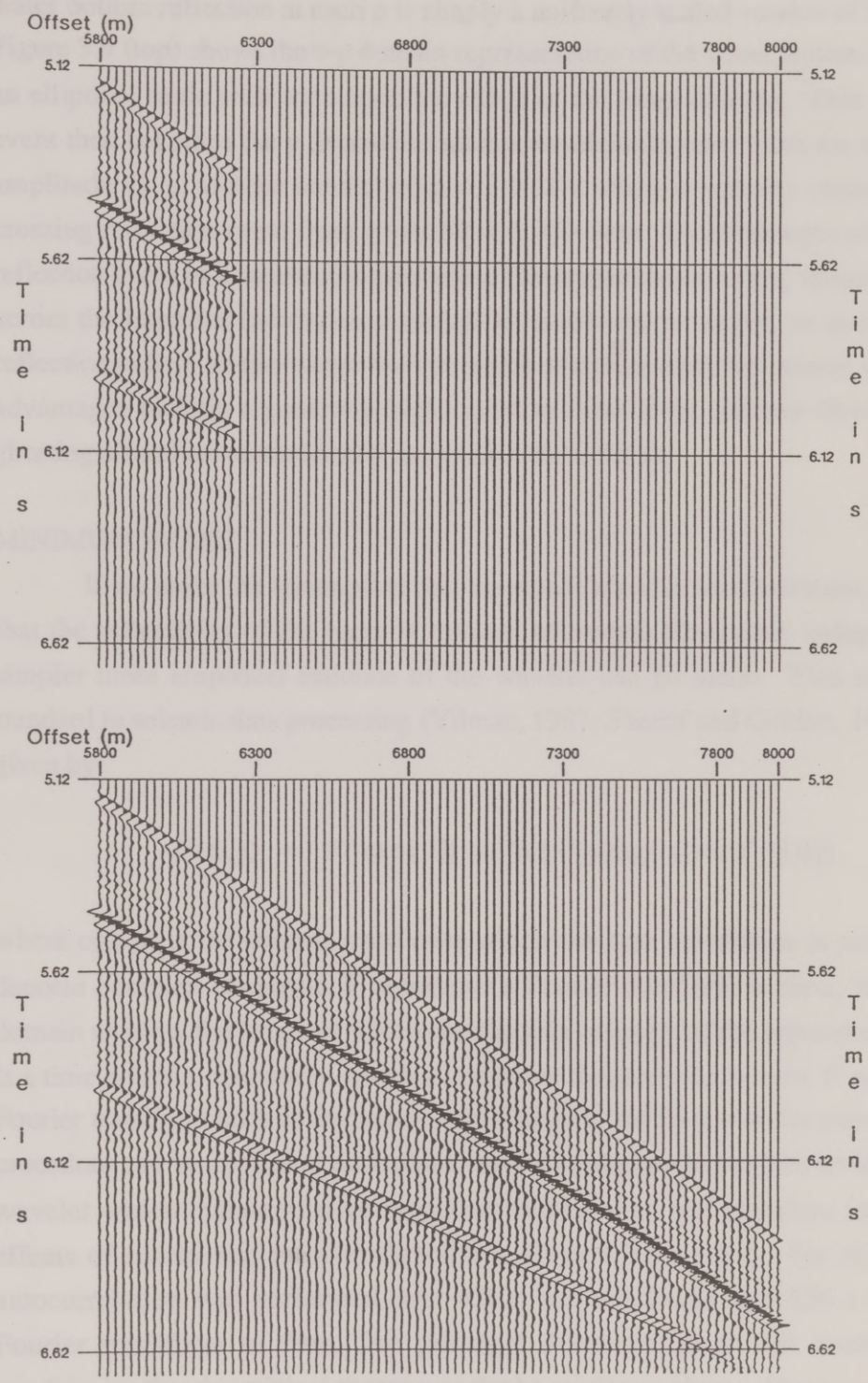

Figure 3.8. (upper) Extrapolation to far offsets is handled similarly although background velocities are required to ensure accurate trajectories. (lower) Again note the continuity of amplitude and trajectory.

water bottom reflection at each p is simply a uniformly scaled version of the source. Figure 3.9 (top) shows the τ-p domain representation of the water bottom event after an elliptical static shift to remove the effect of the water column. This windowed event then becomes the p dependent source wavelet estimate. Note the decrease in amplitude vs. p, and the bubble pulse at ~ 0.22 s which is partially obliterated by a crossing reflection event from p =0.250 to 0.330 s/km. Disadvantages of using this reflection event as a source estimate include inaccuracies due to any velocity changes across the interface (producing a change in amplitude vs. angle), or as in this case reflections close to the water bottom which interfere with the source coda. The advantages include a generally high signal to noise level and any directivity and ghosting effects are automatically included in the estimate.

MINIMUM PHASE

If we make the assumption that the actual wavelet was minimum phase, and that the reflectivity of the earth is random and white (frequency independent), a simpler more empirical estimate of the wavelet can be made. This approach is standard in seismic data processing (Yilmaz, 1987; Sherrif and Geldart, 1986) and is given by

$$C(\omega,p) = F'(\exp\{ H[\ln(W\{ F[c(\omega,p)\, c(\omega,p)^*]\})]\})$$

where $c(\omega,p)$ is the seismic trace over which the auto-correlation is performed, * denotes complex conjugate, F represents a Fourier transform to time, W is a time domain window the length of which corresponds to length of the wavelet estimate, H is a time domain operator in which all negative times are set to zero, F' represents a Fourier transform back to frequency, and $C(\omega,p)$ is the final wavelet estimate. This procedure can be applied to each plane wave seismogram to produce an ω-p domain wavelet which retains relative amplitude information and therefore includes the effects of source and receiver directivity, (Figure 3.9 center). For this case the autocorrelation was performed over 4.0 s, and windowed to 0.256 s before the Fourier transform to time. The principal disadvantage to this method is the requirement that the original source wavelet be minimum phase. Also required is that

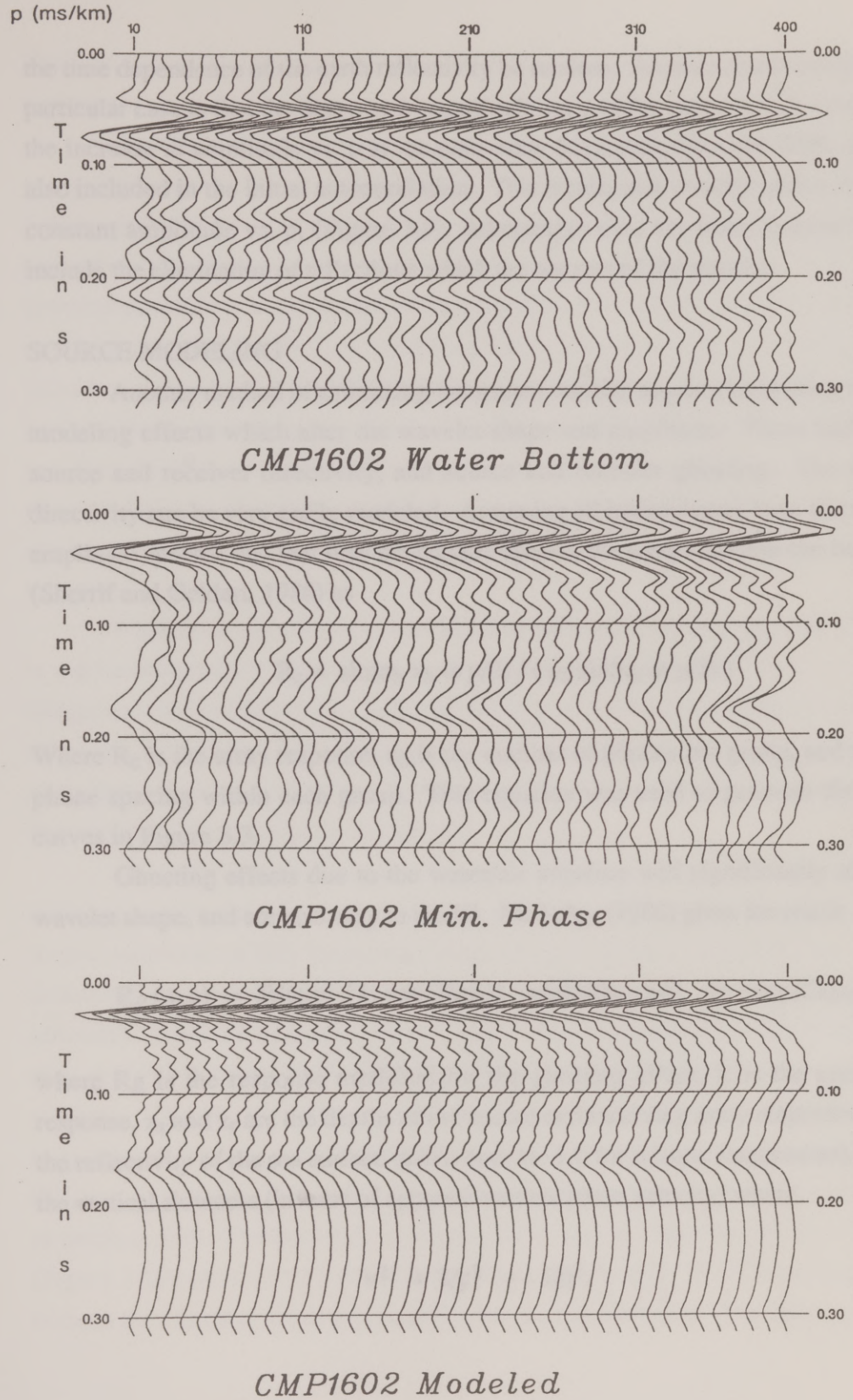

Figure 3.9. The p dependent source wavelet can be estimated by (top to bottom) analysis of the water bottom reflection, minimum phase, or by data independent modeling of source and receiver arrays. Note the same general shape of each estimate, and the decrease in amplitude with p for the water bottom and modeled wavelets.

the time dependence of the earth reflectivity be random. Another disadvantage in this particular case is that the decrease in amplitude vs. p at the water bottom is offset by the increase in amplitude vs. p at the only other large reflection, the BSR, which is also included in the initial autocorelation. This results in a wavelet with a relatively constant amplitude vs. p, (Figure 3.9). Advantages over the water bottom wavelet include the elimination of reflections which are not part of the wavelet.

SOURCE MODELING

Another method of estimating the source wavelet requires estimating and then modeling effects which alter the wavelet shape and amplitude. These include the source and receiver directivity, and source and receiver ghosting. The receiver directivity can be very easily modeled. Assuming all hydrophones have flat and unit amplitude spectra, and that they are equally spaced, the array response can be written (Sherrif and Geldart, 1986) as

$$R_c = \sin(n_h x_h \omega p/2) / (n_h \sin(x_h \omega p/2)) \qquad 3.1$$

Where R_c is the array response, n_h is the number of phones per group, and x_h is the phone spacing within each group. This equation was used to generate the dashed curves in Figure 3.3.

Ghosting effects due to the water/air interface will significantly affect the wavelet shape, and are also easy to model. McAulay (1986) gives the result

$$R_g(\omega,p) = R(\omega,p)\ [1- \exp(2iqz_r)]\ \exp[iq(z_r - z_s)]\ [1 - \exp(2iqz_s)] \qquad 3.2$$

where Rg is the response modified for the ghosting effect, R is the unmodified response, z_s and z_r are the depths of the source and receiving array respectively, r_o is the reflectivity of the sea surface (taken here as -1.0 for seismic frequencies), and q is the vertical slowness (inverse of apparent vertical phase velocity) where

$$v^2 = 1/p^2 + 1/q^2.$$

The first exponential term in Equation 3.2 represents the receiver ghost, and the next two terms represent the source ghost phase shifted to the level of the receivers.

The effect of source directivity is similar in principle to that of the receiver group, but is somewhat more difficult to model. The difficulty arises when the large bubble created by the sudden release of compressed air from a single gun no longer expands and contracts against hydrostatic pressure, but against a time variant pressure caused by the expansion and contraction of the bubbles from the other guns in the array. Ziolkowski et al. (1982) showed that if near field signatures of each gun are measured the time variant pressure can be computed and the signature from each source corrected for this effect. These corrected or notional source signatures can then be added linearly, just as the responses of the individual hydrophones discussed above. For this study the program MODGUN™ generated the notional source signatures from which the source as a function of w and p could be computed.

When all these effects are combined (multiplied in the w-p domain) the result is a data independent wavelet estimate which is based solely on the experimental design and has incorporated no assumptions about wavelet shape or earth reflectivity (Figure 3.9 bottom). Note the decrease in amplitude with increasing p similar in magnitude to that in the water bottom wavelet. Note also the decrease in high frequencies with increasing p as expected.

Although the general shape of these wavelets is similar each has a somewhat different character and it is difficult to say which is the best. In future implementations of this inversion it may be quite helpful to include the wavelet estimation as a part of the inversion, negating the need for this choice. All three estimates implicitly contain a p dependence which is somewhat different for each case, and which appears to be incorrect. The p dependence is therefore removed by stacking. Figure 3.10 shows from left to right the stack of the water bottom, minimum phase and modeled wavelet. Again note the same general shape, but differences in detail. However, the amplitudes of these wavelets vary over time by as much as 25%. For this study I assume that the stacked minimum phase is the best (Figure 3.10 center) since it has close to the same character as the water bottom but without the effects of the crossing reflections mentioned earlier. It is therefore used

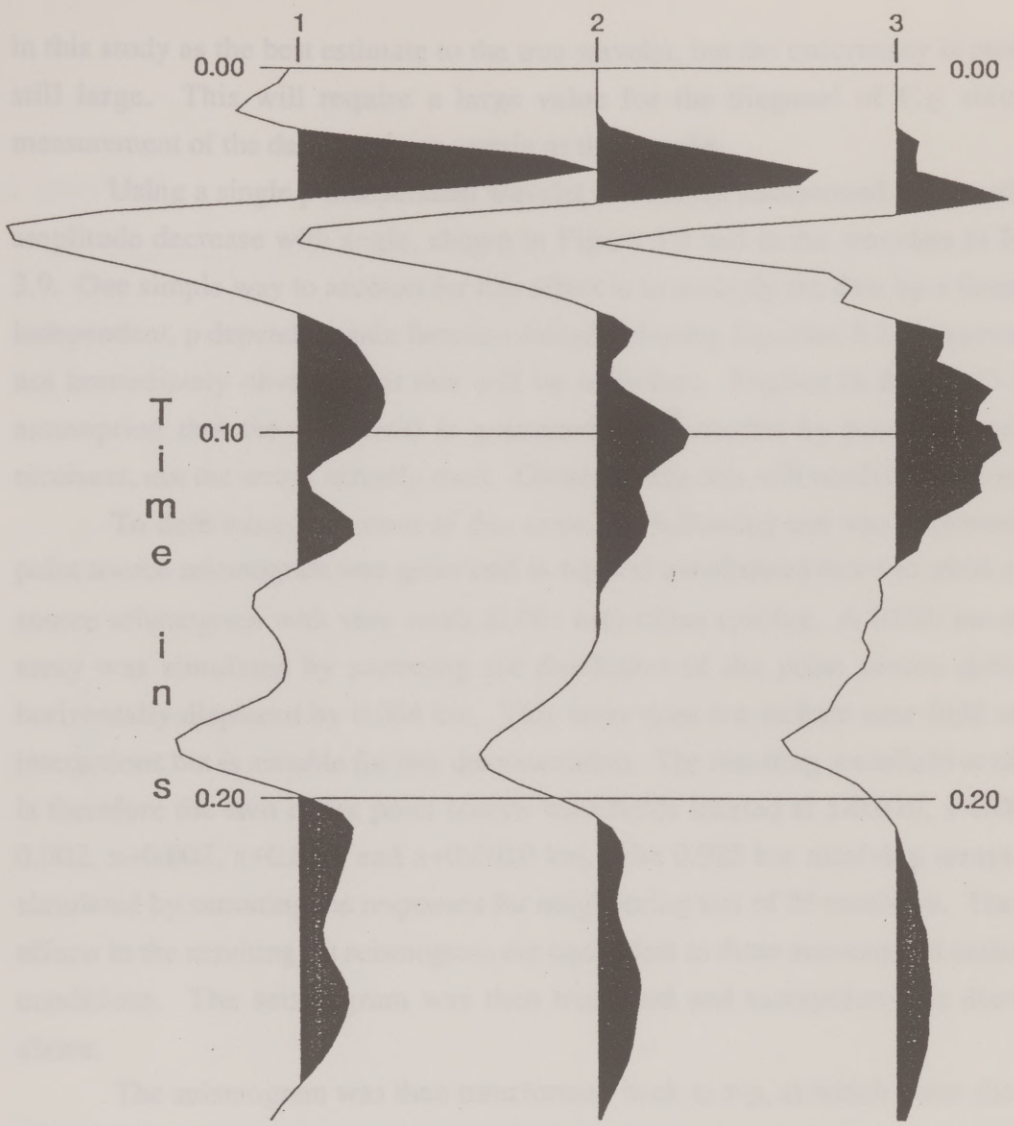

Figure 3.10. Stacking each of the wavelets in Figure 3.9 (left to right; water bottom, minimum phase, and modeled) results in a p independent wavelet with less random noise. The stacked minimum phase wavelet was chosen for this study.

in this study as the best estimate to the true wavelet, but the uncertainty is probably still large. This will require a large value for the diagonal of C_D since the measurement of the data is only as certain as the wavelet.

Using a single p independent wavelet still leaves unanswered the question of amplitude decrease with angle, shown in Figure 3.3 and in the wavelets in Figure 3.9. One simple way to account for this effect is to multiply the data by a frequency independent, p dependent gain function calculated using Equation 3.1. However it is not immediately obvious that this will be sufficient. Implicit in the PWD is the assumption that the wavefield is generated and recorded by point sources and receivers, not the arrays actually used. Consequently, this will result in some error.

To determine the extent of this error, the following test was performed. A point source seismogram was generated in τ-p and transformed to x-t to yield a point source seismogram with very small (0.001 km) offset spacing. A 0.020 km source array was simulated by summing six duplicates of the point source data each horizontally displaced by 0.004 km. This array does not include near field air gun interactions but is suitable for this demonstration. The resulting wavefield at offset x is therefore the sum of six point source wavefields located at x-0.010, x-0.006, x-0.002, x+0.002, x+0.006, and x+0.0010 km. The 0.025 km receiving arrays were simulated by summing the responses for neighboring sets of 25 receivers. The array effects in the resulting x-t seismogram are equivalent to those encountered under field conditions. The seismogram was then truncated and extrapolated as discussed above.

The seismogram was then transformed back to τ-p, at which point the array effects were removed by application of p dependent gain function computed for a constant frequency of 33 Hz. Another seismogram was processed identically except that no array or truncation effects were added in x-t or removed in τ-p. The difference between these two data sets is shown in Figure 3.11. The residual from both the array and truncation artifacts is acceptably small for values of p less than 0.4 s/km, the range used in this study. If improved methods of wavelet estimation are achieved it may be necessary to apply the full ω dependent correction.

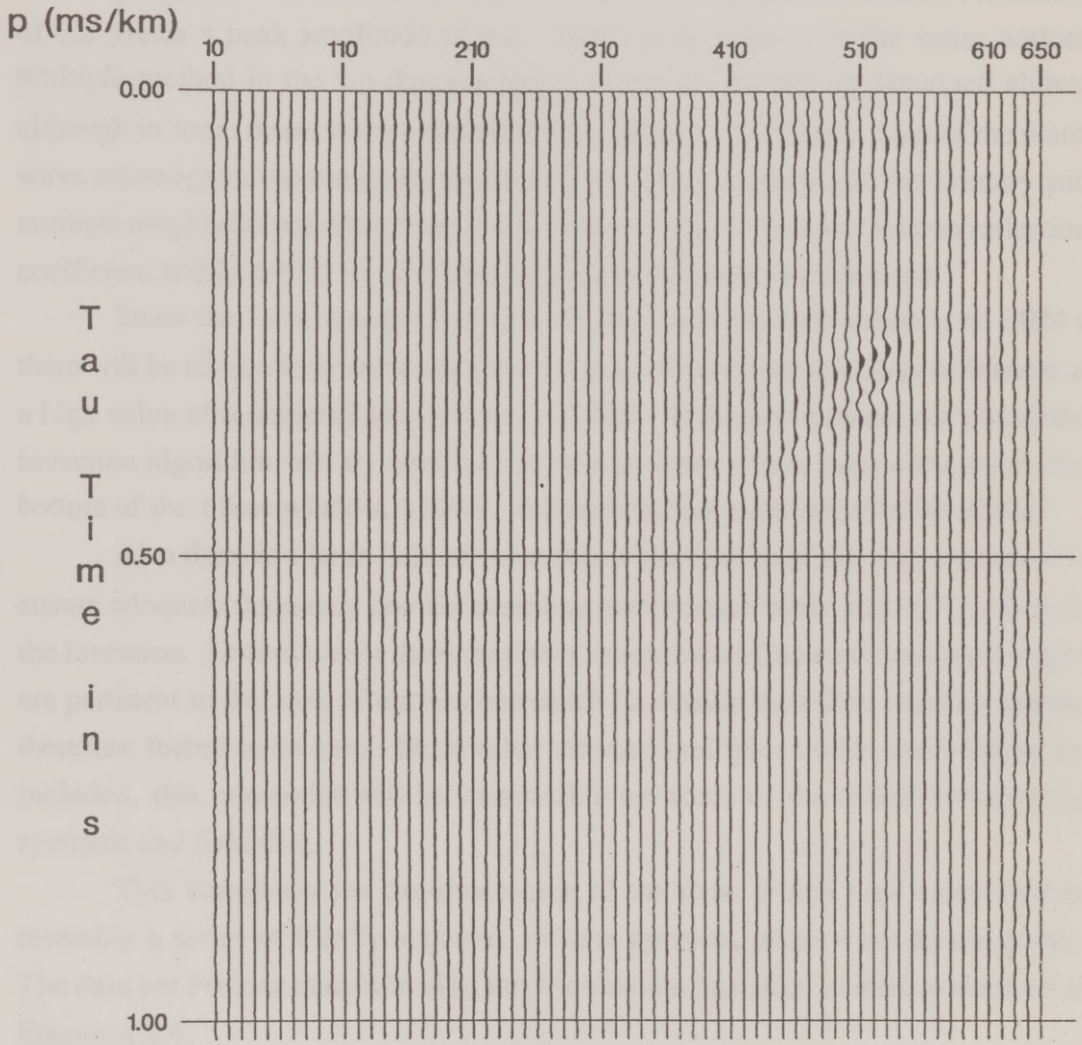

Figure 3.11 This is the error incurred by removing source and receiver directivity effects in the plane wave domain, (assuming a model and data acquisition parameters similar to those used in the Carolina Trough data set). Note the increase in error with p as the directivity becomes more severe.

Final Scaling, Muting, and Windowing

The field data must now be scaled so that, for example a reflection coefficient of 0.2 yields a peak amplitude of 0.2. This can be done with the water bottom multiple method in the τ-p domain just as in the x-t domain as discussed above, although in some respects the calculations are simpler. Since each trace of the plane wave seismogram represents the impinging wave at a single angle, the primary and multiple amplitudes are taken from the same trace. Again the water bottom reflection coefficient is 0.21 ± 0.02 and the plane wave data are scaled to this event.

Since the τ time range of interest of the inversion ends abruptly at 1.024 s there will be some events from just after this time which enter the range of interest at a high value of p (stippled area, Figure 3.12 left). If these events are not muted the inversion algorithm will try (and fail) to find an event which stops abruptly at the bottom of the τ time window, 1.024 s. Actual field data must therefore be muted.

Also there is a large field of zeros below the bottom of the τ time window to ensure adequate frequency domain sampling and prevent "wrap around" artifacts in the inversion. Unfortunately there may also be some data (interbed multiples) which are pertinent to the zone of interest but which lie outside the t time window and are therefore forced to be zero. Since other interbed multiples within the window are included, this constraint will be responsible for some of the misfit between the synthetic and field data.

This completes the pre-processing of the data, which now more closely resemble a series of ideally acquired, infinite aperture, plane wave seismograms. The data are Fourier transformed to the w-p domain just prior to implementation of Equation 2.4.

Results of Inversion

The best inversion result achieved on the CMP1602 data is shown in Figure 3.12. The prior uncertainty in V_p was taken from a high resolution travel time analysis (Stoffa et al., 1992), and $\text{diag}[C_D] = 4.0$. As discussed in Chapter 2, the variations in V_p, V_s, and density of the model can only be recovered at frequencies less than or equal to those of the data, in this case ~65Hz. Therefore the model

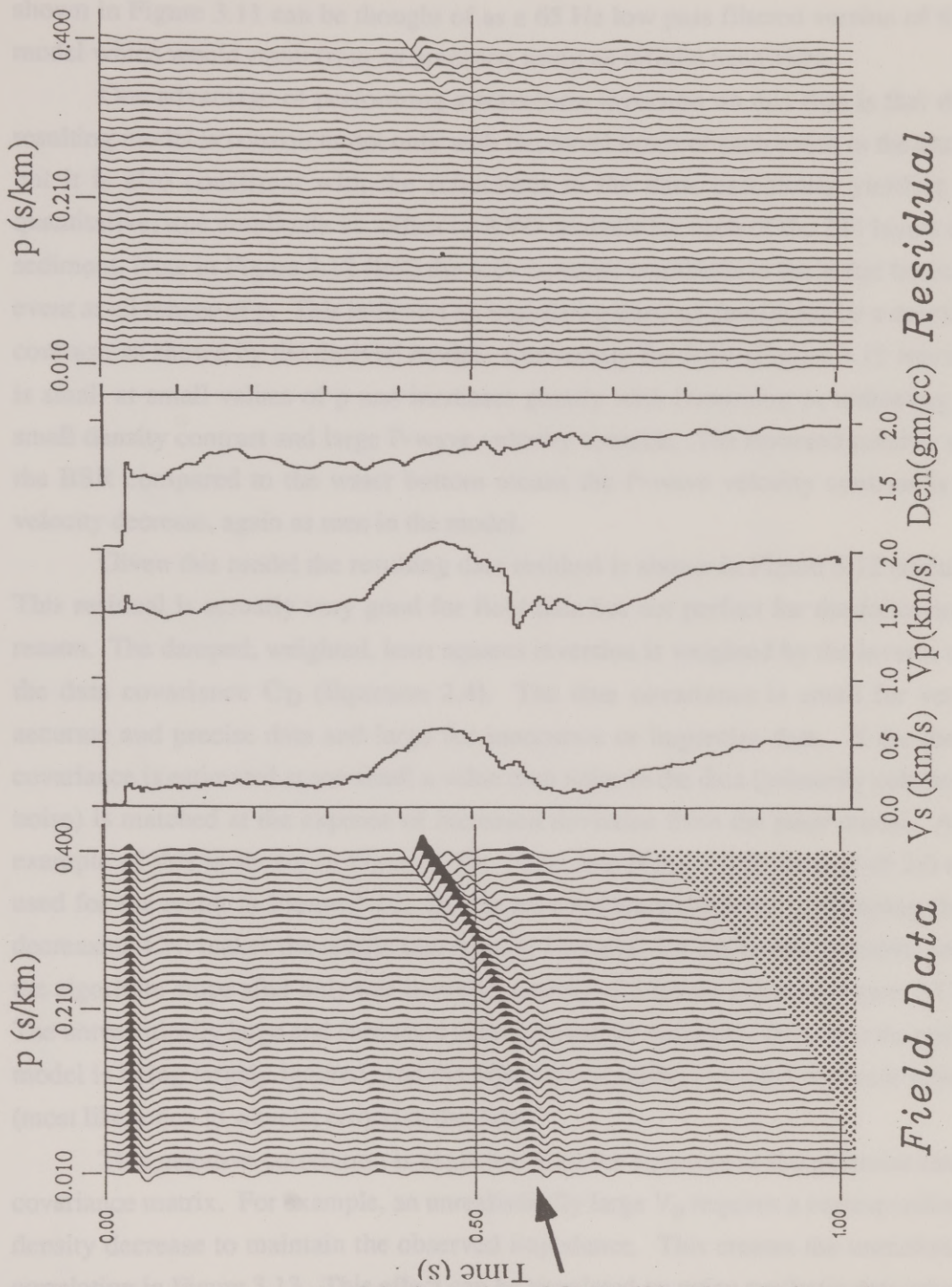

3.12. This is the best result of the inversion of CMP1602. Note the large decrease in V_p, relatively unchanged density, and slight increase in V_s at the BSR (0.6 s at p=0.0 ms/km).

shown in Figure 3.11 can be thought of as a 65 Hz low pass filtered version of the model which would result from an inversion using an infinite bandwidth.

One advantage of performing a waveform inversion on this data is that the resulting model is consistent not only with the travel times of each event in the data, but it is also consistent with the reflections in the data, essentially yielding a quantitative, true amplitude vs. offset or AVO analysis for each of the 244 layers of sediment. Note in Figure 3.12 (left) the very constant amplitude in the water bottom event at all ranges of p. This indicates an impedance contrast dominated by a density contrast, as shown by the derived model. Conversely the BSR (Figure 3.12 arrow) is small at small values of p and increases greatly with increasing p, indicating a small density contrast and large P-wave velocity contrast. The reversed polarity of the BSR compared to the water bottom means the P-wave velocity contrast is a velocity decrease, again as seen in the model.

Given this model the resulting data residual is shown in Figure 3.12 (right). This residual is actually very good for field data but not perfect for the following reason. The damped, weighted, least squares inversion is weighted by the inverse of the data covariance $\mathbf{C}_D$ (Equation 2.4). The data covariance is small for very accurate and precise data and large for inaccurate or imprecise data. If the data covariance is estimated at too small a value then noise in the data (primarily coherent noise) is matched at the expense of increased deviation from the prior model. An example of this is shown in Figure 3.13. Here diag $[\mathbf{C}_D] = 0.25$ instead of 2.0 as used for the result in Figure 3.12. In this case reducing the level of damping (by decreasing $\mathbf{C}_D$) makes the matrix inversion in Equation 2.4 somewhat unstable, and the algorithm stops after only one iteration, instead of 3 for the result in Figure 2.12. The unrealistically large and correlated elastic parameter variations show that the prior model is being largely ignored, and the algorithm is trying to model coherent noise (most likely due to wavelet errors) in the data.

This negative correlation is expected from the structure of the posterior data covariance matrix. For example, an unrealistically large V_p requires a corresponding density decrease to maintain the observed impedance. This creates the unrealistic correlation in Figure 3.13. This effect can be simulated on noisy synthetic data when noise in the data is underestimated. However, the opposite effect, a positive

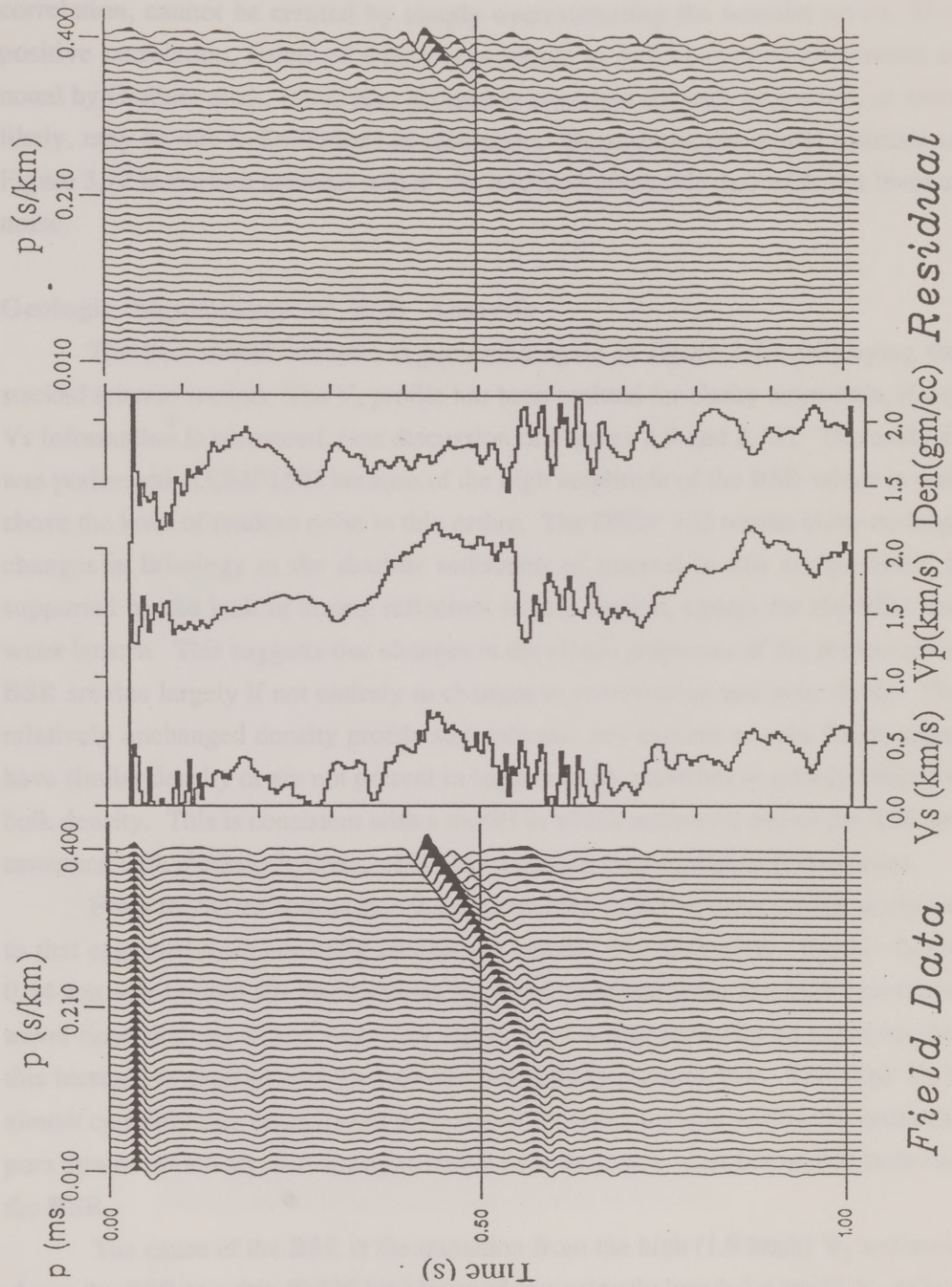

3.13. If a smaller noise level (less damping) is used the matrix inversion becomes less stable and a poorer data residual is obtained. The algorithm is also less constrained by the prior model and unrealistically large and strangely correlated elastic parameter profiles result.

correlation, cannot be created by simply overestimating the wavelet errors. This positive correlation, (some of which is expected in sedimentary environments as noted by Gardner et al., 1974) may accurately represent the rock properties, or more likely, may be due to limitations in resolution. Regardless, the model estimate in Figure 3.12 is the best estimate which can be found given this data with this level of noise.

Geologic Significance of BSR Analysis

The best model estimate is presented again in figure 3.14 overlaying the stacked seismic section. The V_S profile has been omitted for clarity since little, if any Vs information is recovered, (see discussion of Figures 2.9 and 2.12). The analysis was performed at CMP1602 because of the high amplitude of the BSR which is well above the level of random noise in this gather. The DSDP 533 results show no large changes in lithology in the shallow sediments of interest in this study, which is supported by the lack of strong reflectors in this section, except for the BSR and water bottom. This suggests that changes in the elastic properties of the section at the BSR are due largely if not entirely to changes in cementation and pore fluids. The relatively unchanged density profile suggests that any cement or pore fluids either have similar density or are not present in large enough quantities to greatly affect the bulk density. This is consistent with a model in which sediments above the BSR are cemented with methane hydrate, which has a density very similar to that of water.

From the water bottom to ~ 0.3 km sub-bottom the velocity profile is similar to that expected from normally compacted hydrate free sediments. From ~ 0.3 to 0.44 km sub-bottom the background V_p trend obtained from the high resolution travel time analysis shows velocities higher than would normally be expected, but this increase is gradual enough such that reflectivity remains low. This high V_p is almost certainly due to increased amounts of methane hydrate within the sediment pore spaces which are also acting to cement the sediment. Just below this zone lies the BSR.

The cause of the BSR is the transition from the high (1.9 km/s) V_p sediment above the BSR to a thin (0.025 km) layer of anomalously low (~1.4 km/s) V_p below the BSR. Note the velocity increase below the sharp decrease indicating that some

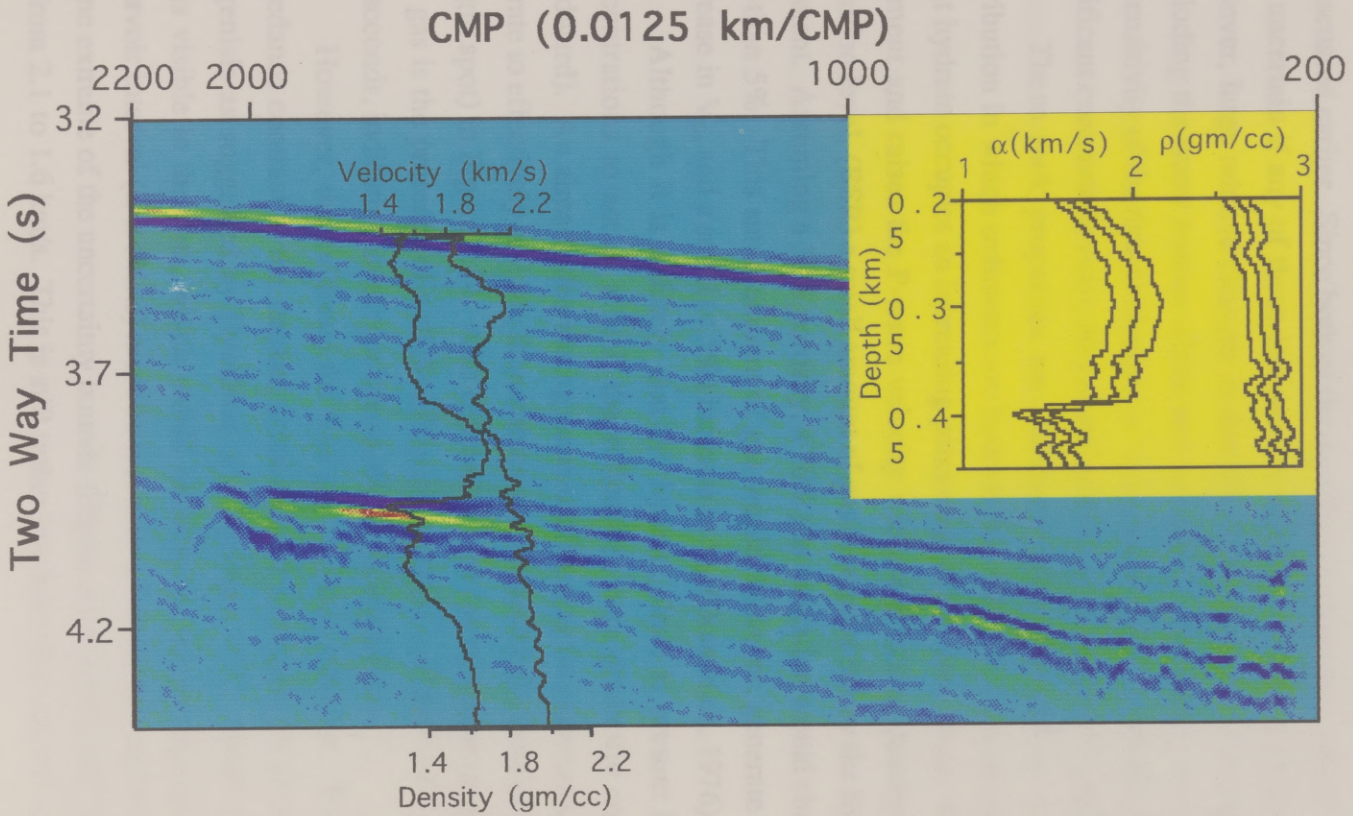

Figure 3.14. When Vp and density Density are superimposed on the stacked section the large velocity decrease at the BSR is seen as a high amplitude event (bright spot). The subbottom depth profiles and the posterior uncertainties are shown in the insert.

constructive interference (tuning) is enhancing the BSR. Below this level the V_p profile returns to that expected of normally compacted sediments in this area.

The density and V_S result of the inversion are more poorly resolved than V_p as discussed earlier. Since both of these profiles contain only small (5%) deviations, it is uncertain if any of these features correspond to actual rock property changes. However, large relative changes in density should be detectable but none are seen (excluding the water bottom which was included in the starting model). Also since the sensitivity of the data to changes in V_S increases greatly with increasing V_S, if any significant contrasts do exist, they must be from an already low V_S to even lower V_S.

These rock properties are consistent with a model of methane hydrate distribution in which sediments are hydrate free until ~0.3 km sub-bottom at which point hydrate occupies an increasing percentage of the pore space. This cements the sediment and raises the P-wave velocity without affecting density. At the phase transition level, (BSR) a small amount of gas is trapped below the hydrate cemented sediment. Assuming a 30% porosity, a 10% gas saturation would change the density less than 5%. This small amount of gas would, however, generate a large (~25%) decrease in V_p, and a small (< 5%) increase in V_S, (Domenico, 1976).

Although it is unlikely that the hydrate alone is present in high enough concentrations to act as a seal, the reflections here gradually converge up dip, (landward). An already decreasing permeability may be augmented enough by the hydrate to effectively seal small quantities of gas causing the zone of high reflectivity (bright spot) in Figure 3.14. Also consistent with the existence of small amounts of free gas is the presence of a slight diffraction visible in Figure 3.14 at CMP 2100 at 4.0 seconds, indicating an abrupt lateral change in impedance.

However, the evidence for free gas is not conclusive. The abrupt lateral impedance contrast in the stacked section could be caused by increased carbonate diagenisis as suggested by Hyndman and Spence (1992). Since there are no flat spots visible in the data, which would indicate the bottom of a gas reservoir, the reservoir interval (if it exists) must be less than a few meters thick. Finally, if taken at one extreme of the uncertainty bounds (Figure 3.14, insert) the V_p decrease could be from 2.1 to 1.6 km/s. This is still rather low but other interval velocity analyses

in this area show thick layers at this depth with a velocity of 1.6 km/s or lower where no flat spots or other indications of gas exist.

Although some questions remain, by employing a waveform inversion of the data, ~ 6 meter resolution of sediment elastic properties is obtained showing in detail the elastic properties of the phase transition responsible for the BSR at the bright spot in Figure 3.14. These findings point toward the existence of a thin (~0.025 km) layer of gas charged sediments below the BSR. This differs from the findings of Hyndman and Spence (1992) who studied the BSR in the northern Cascadia subduction zone and found no evidence for an anomalously low velocity layer beneath the BSR.

Remarks

The exceptionally high resolution elastic parameter profiles resulting from the waveform inversion were essential for the analysis of the BSR in this area. A more conventional analysis of the stacked data would have revealed substantially less information than what the data actually contained. Since the objective in this analysis concerned primarily events in close proximity to the BSR, only those events were fully discussed. However, the results from the inversion of the Nankai data will show events of interest throughout the section both vertically and laterally.

Chapter 4
Preparation of Background Model, and Large and Small Aperture Seismic Data in the Nankai Trough

Introduction

As mentioned earlier the 1987 Nankai Trough survey consisted of two types of seismic data, expanding spread profiles, (ESPs), and conventional multi-channel seismic or (MCS) data. The MCS data have been configured into a common midpoint (CMP) geometry, mitigating the effect of dipping layers (Diebold and Stoffa, 1981) so that each CMP has the appearance of being collected in a 1-D area. The ESPs also underwent preliminary processing to generate equi-distant traces in a CMP gather, (Stoffa et al., 1992). Thus both types of data have the same source and receiver configuration, the principal difference being the aperture size, up to 22 km for the ESPs and 1.6 km for the MCS data. Both data sets are suitable for the 1-D inversion but because of the very large offset range of the ESPs more detailed elastic parameter information can be obtained from these profiles. The MCS data were acquired with a much smaller aperture and are sensitive almost exclusively to changes in acoustic impedance.

Geologic Objectives

Convergent plate margin tectonics are strongly dependent on sediment physical properties which control deformation and resulting structural geometry. Since the Nankai trough is very well imaged seismically (bedding and fault planes are more clearly delineated than in other accretionary wedges) it seems reasonable that a careful analysis of seismic data in this wedge, both in terms of imaging and inversion for sediment properties, should provide a better understanding of the mechanics of sediment accretion.

Inversion of the Nankai Trough data provides the detail to complement the background elastic parameters obtained from the travel time analysis and well data. While low frequency profiles are adequate for resolving large features (zones of relatively low V_p and inferred density), waveform modeling is required to delineate the boundaries of these large zones, and to locate other smaller features.

In an area such as the Nankai Trough where matrix lithology is reasonably well known from well and other data, large unexpected zones of anomalously low V_p are generally associated with high fluid content, especially if a noticeable low density zone is also present. High fluid content at depth is often found in conjunction with increased pore pressures, decreased cementation, and shear strength, (Han et al., 1986). Thus low V_p zones have in the past been assumed to delineate zones of shear weakness, particularly in the case of a low angle decollement in a subduction zone, (Moore et al., 1990; Bangs et al. 1990). If these sediments are under horizontal stress it is within these zones that slip is most likely to occur.

If these low V_p zones are in fact fluid rich compared to neighboring sediments some may represent localized conduits through which the wedge sediments are dewatering. It is the goal of the inversion to accurately locate these low V_p zones (and low V_s zones if possible) and to quantify the extent of the velocity and density reduction.

Preliminary Analysis; Formation of a Starting Model

The formation of the prior model to be used in the inversion was a relatively simple matter for the single Carolina Trough CMP gather discussed in Chapter 3. However, since the objective here is a 2-D cross section of sediment properties, a 2-D background model must first be established. The background V_p, V_s, and density are smooth (< 5 Hz) versions of profiles taken from nearby well data and high resolution travel time analysis (Stoffa et al., 1992) of the ESP data.

DETERMINING BACKGROUND V_p

The processing and interval velocity travel time analysis of the two ship seismic data has been discussed extensively in Wood (1989). Briefly, the ESP data were first sorted into common offset bins to improve the signal to random noise ratio. The bins were 0.01667 km wide resulting in slight travel time differences within each bin. This was corrected by statically shifting each trace such that the water bottom events were aligned. The data were then transformed into the τ-p domain with a simple slant stack, and the high resolution travel time velocity analyses were performed.

These analyses were performed at several locations along the toe of the wedge. Figure 4.1 shows the stacked, depth migrated MCS dip line and the location of the ESPs of interest and two DSDP well locations very close to this line (see also Figure 1.4). Figure 4.2 is a line drawing based on the data in Figure 4.1 showing the major reflections and general lithology. Also shown are the results of the ESP travel time analysis. As evidence of the high accuracy of the data and methods the depth to the decollement determined by similar analyses in an area ~100 km to the north east was confirmed by ODP drilling to be within ~0.010 km (Taira et al., 1991). The exact positions (latitude, longitude, shot point, and CMP) of the ESP midpoints and DSDP sites is given in Table 4.1.

To determine the background V_p between the ESP sites the profiles were linearly interpolated parallel to high amplitude reflections in the wedge, (i.e. those shown in the line drawing). Vertical variations more rapid than 5 Hz were removed by low pass filtering. The resulting background V_p model is shown in Figure 4.3. Note the general landward and downward increase in V_p, with prominent low velocity zones from 5.4 km depth at s.p. 131 to 5.9 km depth at s.p. 550, and a thinner parallel zone 0.5 km deeper, just above the oceanic crust. At 4.8 km depth at s.p. 740 another low V_p zone exists, extending seaward to 5.2 km depth at s.p. 690. Although the oceanic crust is not directly of interest in this study it is included in this model so that the sediment-crust interface may be properly modeled. Several inter-crust reflections were found enabling a travel time velocity analysis of the crustal material, which was found to have a V_p of ~4.0. In this model the crust V_p is assumed constant.

Since almost no low frequency V_p information is available from the MCS data (due to only 10° of angular coverage at the water bottom), this model represents the best possible estimate of the background V_p in this area. Although some sonic velocity measurements were made on cores from the DSDP wells these measurements were very sparse. Also, since these measurements were made on very small in vitro samples at very high frequencies they are not as pertinent to the waveform inversion as those V_p measurements made from the ESPs.

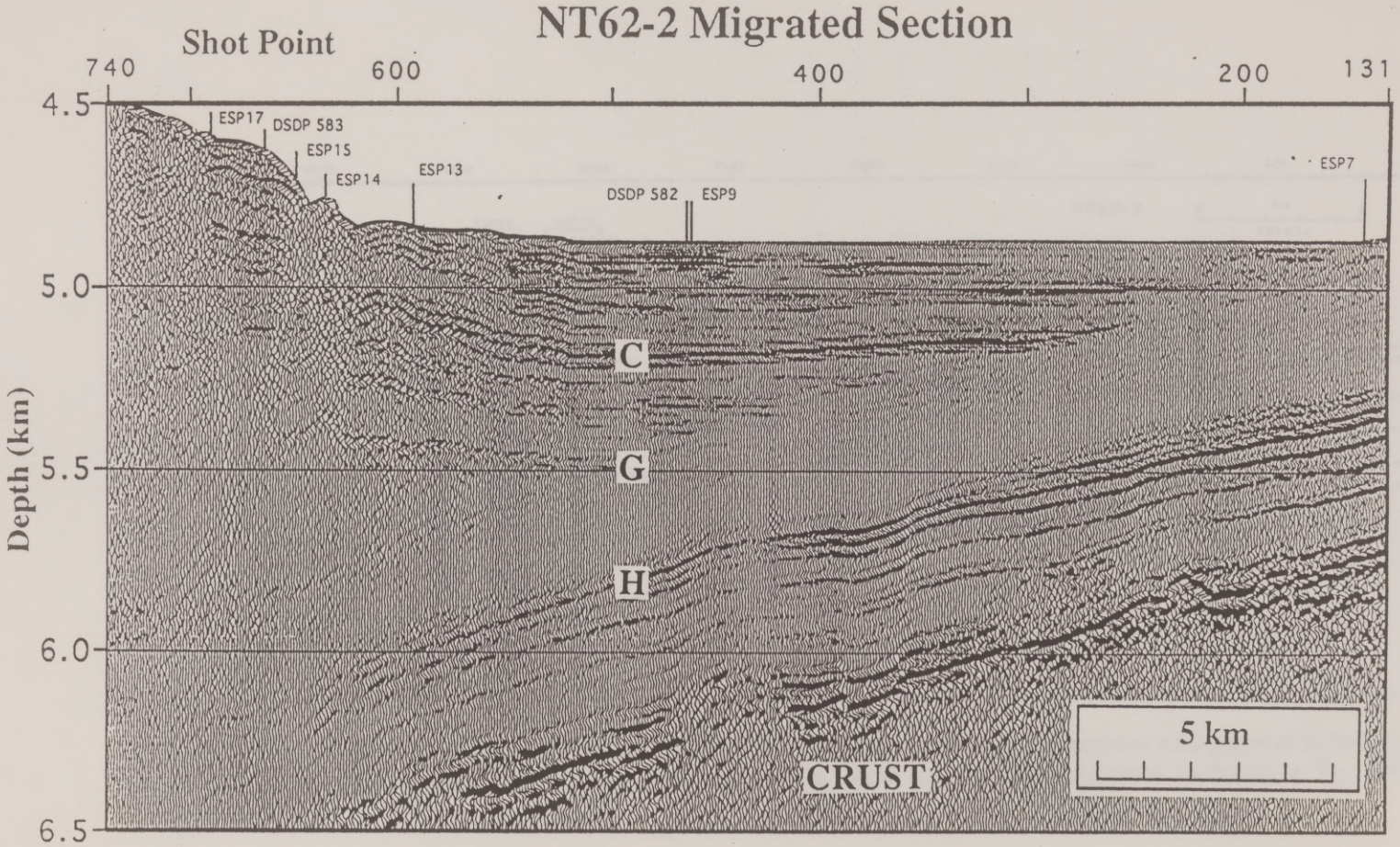

Figure 4.1. The MCS data of NT62-2 were stacked and migrated with the background Vp from the travel time analyses. This image shows the subducting crust (5.7 km at s.p. 131) overlain by ~0.8 km of Shikoku basin hemipelagic sediment (4.9 to 5.7 km at s.p.) inturn overlain by a landward thickening trench fill sediment wedge (zero thickness at s.p. 131 to 1.5 km thick at s.p. 740). Note the landward decrease in trench fill deformation.

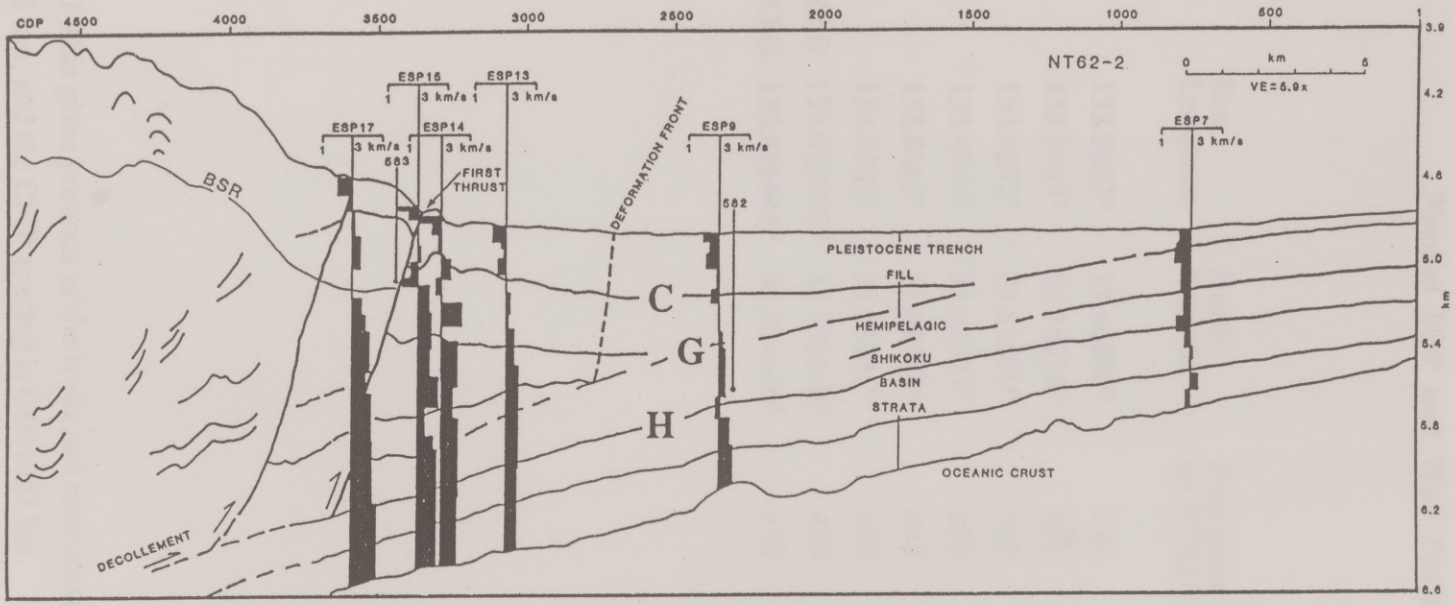

Figure 4.2. This line drawing based on the data in Figure 4.1 shows the major reflections and general lithology of the wedge, along with the ESP travel time analysis results. Note the general landward increase in V_p. (From Stoffa et al. 1992)

Nankai ESP and Well Position

	East Longitude	North Latitude	Shot point on NT62-2	CMP on NT62-2
ESP7	133.9903°	31.66900°	148	768
ESP9	133.8955°	31.76238°	461	2356
ESP13	133.8672°	31.81030°	592	3074
ESP14	133.8584°	31.82327°	633	3290
ESP15	133.8466°	31.82284°	647	3363
ESP17	133.8332°	31.83746°	690	3591
DSDP 582 B	133.913833°	31.775166°	470	2327
DSDP 583 G	133.856666°	31.834500°	470	3443

Table 4.1 This gives postions of the wells and midpoints of the ESPs. Shot spacing is ~0.045 km, and the CMP spacing is 0.001667 km.

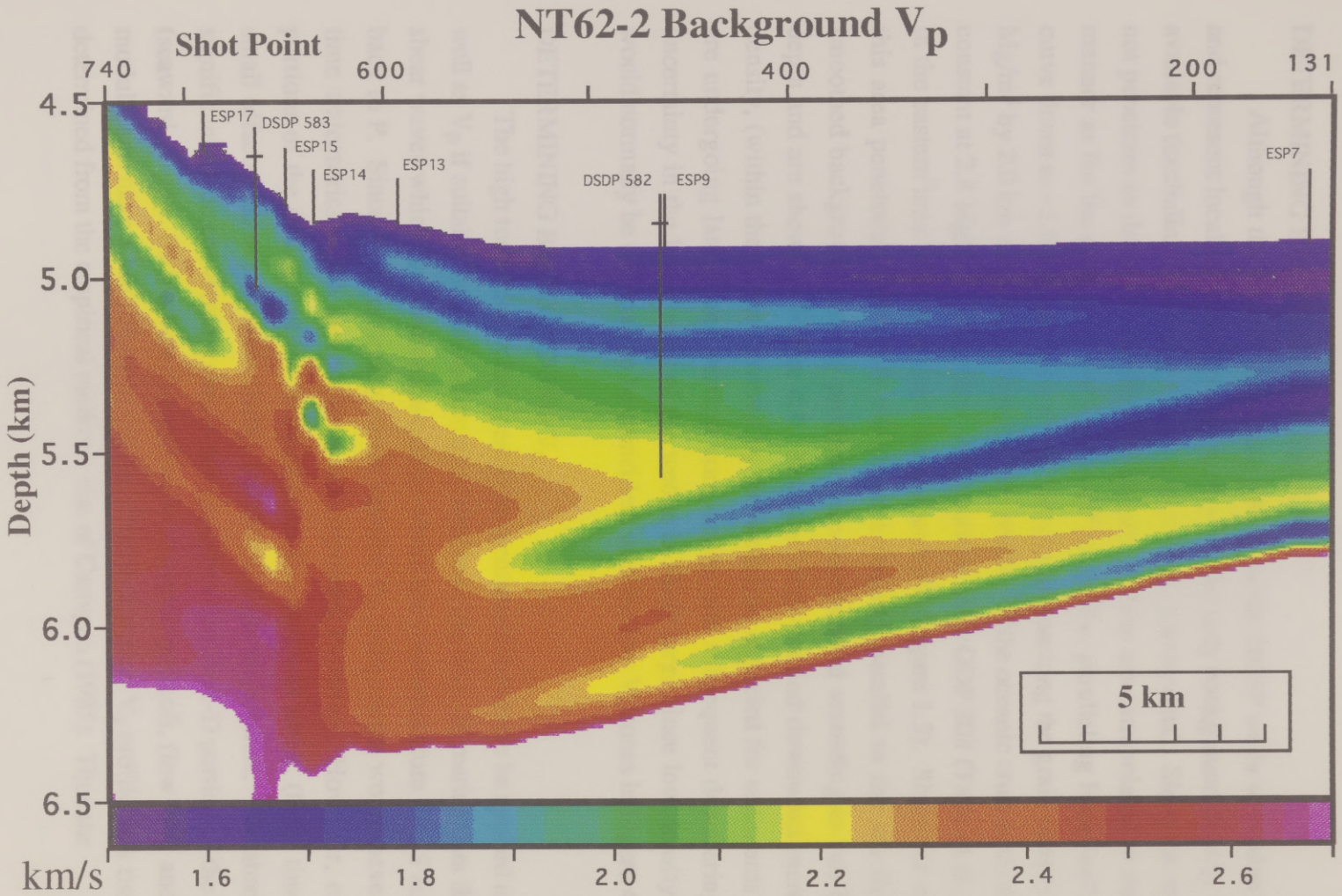

Figure 4.3. The background Vp from the travel time analyses shows significant low velocity zones from s.p. 131 at 5.4 km depth to s.p. 550 at 5.9 km depth, and a parallel zone 0.5 km deeper. Others are found higher on the wedge.

DETERMINING BACKGROUND DENSITY

Although the density measurements from the DSDP wells were also sparse and represent localized measurements, they are the only background density values available (excluding inherently very low resolution gravity data). Since the wells do not penetrate as deeply as needed, the density profiles are extrapolated in the same manner as for the density in the Carolina Trough, (i.e. paralleling Hamilton's 1976 curve down to ~1.0 km sub-bottom and linearly approaching the grain density of 2.7 Mg/m^3 by 2.0 km sub-bottom depth). The density of the oceanic crust is taken to be constant at 2.8 Mg/m^3. This value was obtained from ODP 808 (Taira et al., 1991) in the eastern area where the crust was penetrated, (Figure 1.3). Since the wells in this area penetrated sediments which were roughly parallel to the sea floor the smoothed background density profiles were interpolated according to sub-bottom depth and are shown in Figure 4.4. Note the landward and downward increase in density, (within the depths covered by the wells), as expected for sediments which are undergoing lateral and vertical compaction and subsequent dewatering. The uncertainty in the lower parts of the wedge is likely large since low density zones would normally be expected to be coincident with the low V_S zones in Figure 4.3.

DETERMINING BACKGROUND V_S

The high resolution velocity analysis mentioned above can be applied to V_S as well as V_P if suitable reflection events are visible in the data. In marine data the only shear waves which are recorded are those which are converted from P to S and then back to P. Since V_S is generally much smaller V_P these events would have travel time trajectories much steeper than nonconverted P-waves. However, even in portions of the data where interference from P-waves was small, (large times and small offsets), no events were visible which had these trajectories. The absence of significant mode converted waves is not unexpected in the 1-D portion of the trench (seaward of ~s.p. 600) where the sediments are relatively soft, (low bulk and shear moduli) and have a high Poisson's ratio. The background V_S profile was therefore determined from the empirical mudrock line of Castagna (1985). Thus the

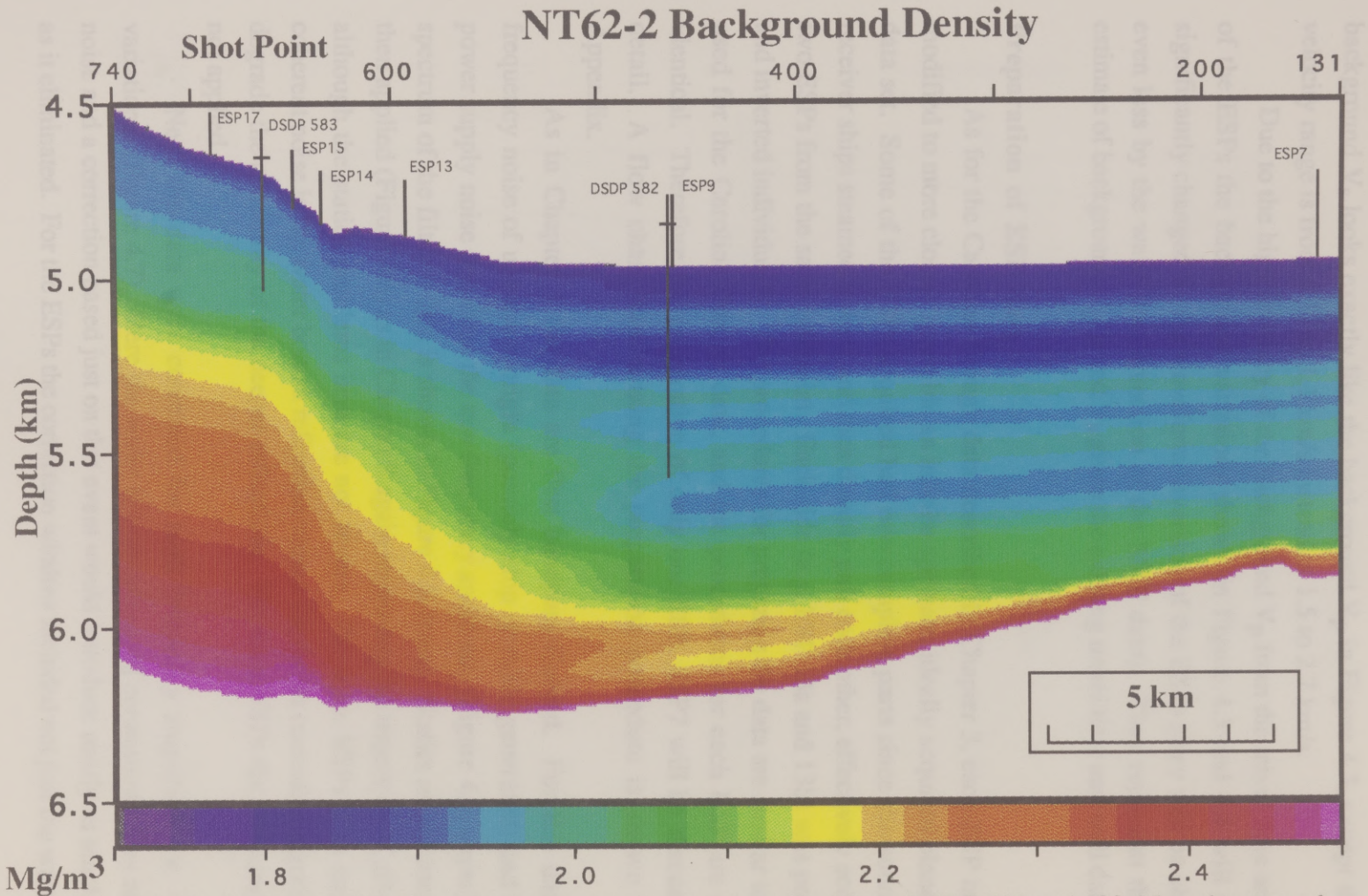

Figure 4.4. The background bulk density interpolated and extrapolated from DSDP 582 and 583. Note the general density increase down and landward.

background V_S looks exactly like the background V_P in Figure 4.3, except that the velocity range is from 0.17 to 1.1 km/s instead of 1.5 to 2.7 km/s.

Due to the high accuracy of the background V_P from the travel time analyses of the ESPs the background variations shown in Figure 4.3 and 4.4 will not be significantly changed by the waveform inversion of the ESPs (they will be changed even less by the waveform inversion of the MCS data). They represent the best estimate of background V_P, ρ and V_S given the existing travel time and well data.

Preparation of ESP data

As for the Carolina Trough data described in Chapter 3, each ESP must be modified to more closely resemble an infinite aperture, ideally acquired plane wave data set. Some of the ESPs acquired had two complete parts since the source and receiver ships steamed toward and then directly past each other, effectively acquiring two ESPs from the same midpoint. Each side (e.g. ESP 13a and 13b) was prepared and inverted individually. The procedures for preparing the data are similar to those used for the Carolina Trough data, and the procedures for each ESP are nearly identical. Therefore the preparation of only one ESP, ESP7 will be discussed in detail. A flow chart summarizing the preparation procedure is shown in the Appendix.

As in Chapter 3 the data are first bandpass filtered. For this data low frequency noise of unknown origin (possibly ship or cable generated) and 60 Hz power supply noise dominate the raw frequency spectrum, (Figure 4.5, upper). The spectrum of the filtered data is shown in Figure 4.5, lower. Statics corrections were then applied (Figure 4.6) as in Chapter 3 again improving the trajectory of all events although the statics problems here are not severe. For some ESPs (13a and 17b) coherent noise in the water bottom reflection caused the statics correction algorithm to degrade the continuity of the deeper reflections. For these ESPs the correction was not applied.

Next the data were corrected for high frequency amplitude vs. offset variations, (Figure 4.7). Here the water bottom appeared contaminated by random noise and a correction based just on this event would introduce nearly as much noise as it eliminated. For the ESPs the correction window included not just the water

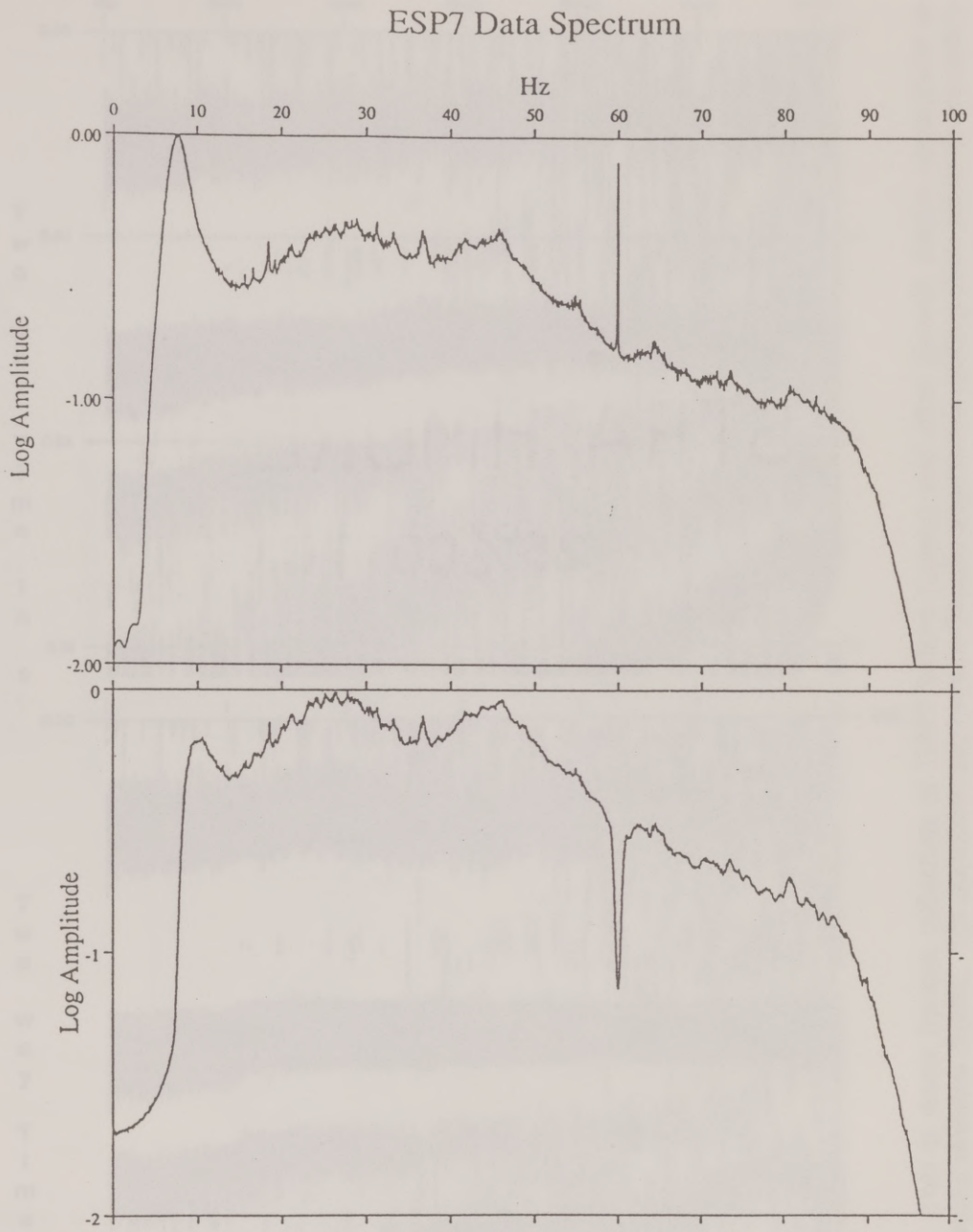

Figure 4.5. The amplitude spectrum of the ESPs was dominated by an unknown ~8 Hz source and 60 Hz power supply noise. Filtering (lower) removed these effects.

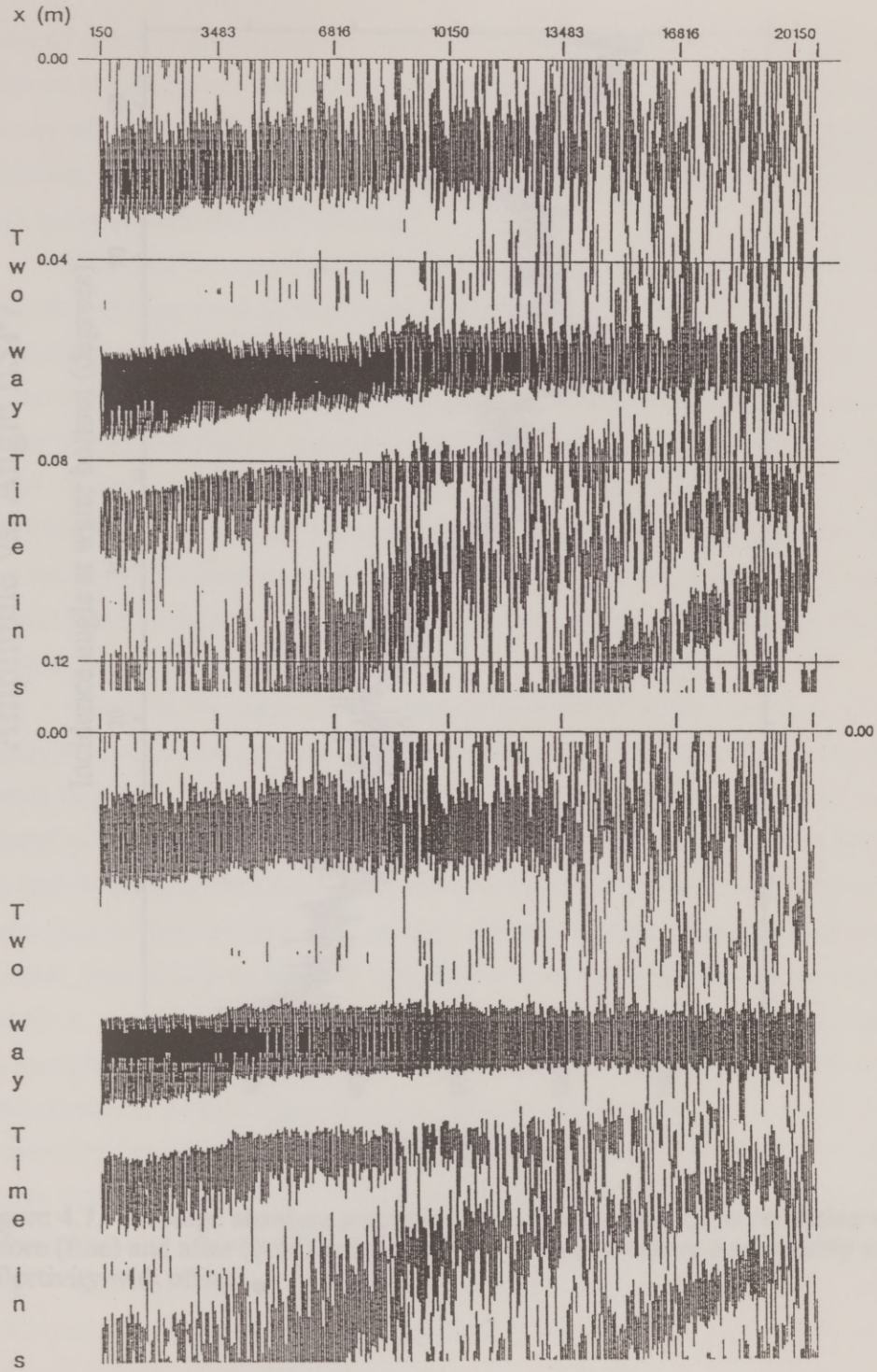

Figure 4.6. This is water bottom reflection of ESP7 before (upper) and after (lower) statics corrections to reconcile varying streamer depths. The correction improves reflection trajectories making them easier to accurately model.

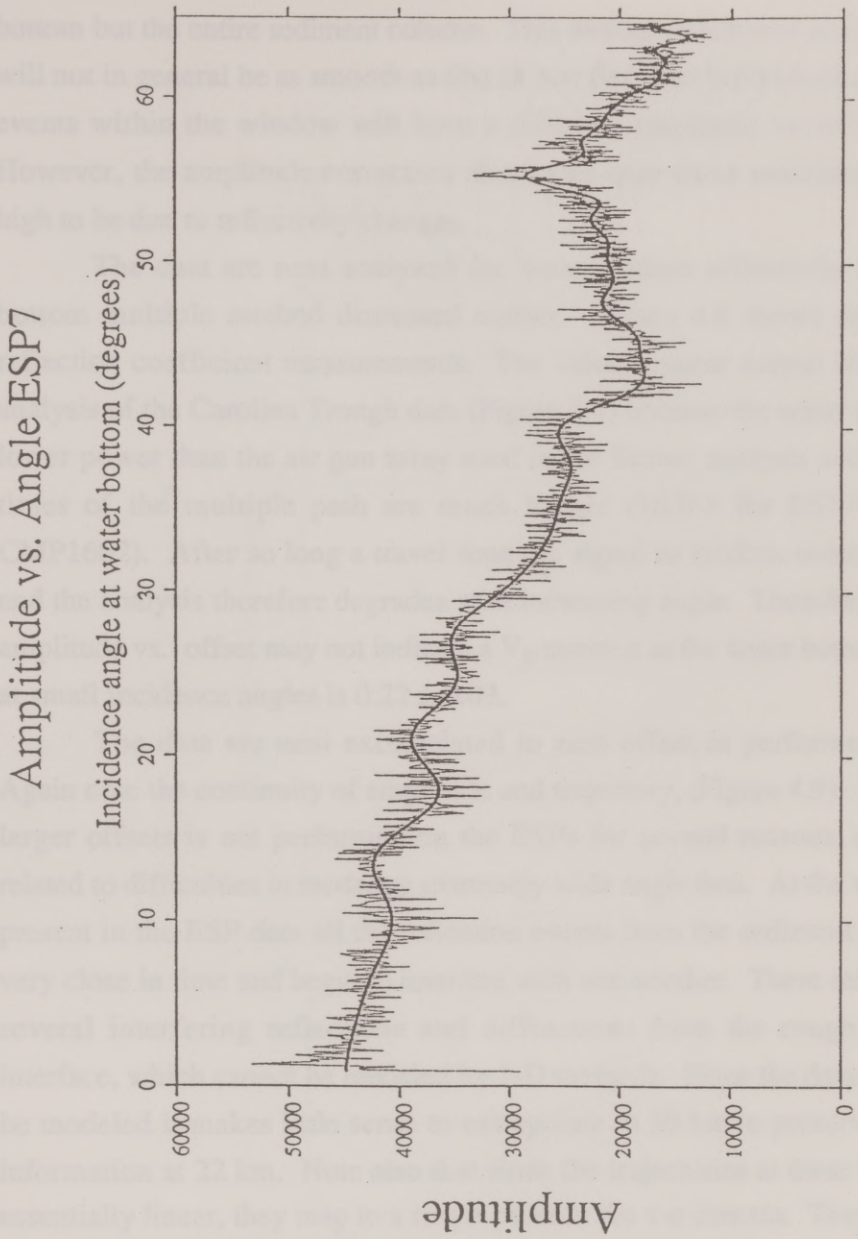

Figure 4.7. Average absolute amplitude of the sediment column reflection events before (fine) and after (bold) individual trace scaling to ensure a reasonably smooth reflectivity with offset.

bottom but the entire sediment column. This average windowed amplitude vs. offset will not in general be as smooth as that of just the water bottom since some different events within the window will have a different amplitude vs. offset dependence. However, the amplitude correction eliminates only those variations which are too high to be due to reflectivity changes.

The data are next analyzed for water bottom reflectivity using the water bottom multiple method discussed earlier. Figure 4.8 shows the water bottom reflection coefficient measurements. The values appear noisier than for the same analysis of the Carolina Trough data (Figure 3.4) because the water gun array was of lower power than the air gun array used in the former analysis and two way travel times of the multiple path are much longer (16.0 s for ESP7 vs. 8.0 s for CMP1602). After so long a travel time the signal to random noise level degrades, and the analysis therefore degrades with increasing angle. Therefore the increase in amplitude vs. offset may not indicate a V_p contrast at the water bottom. The average at small incidence angles is 0.22 ± 0.03.

The data are next extrapolated to zero offset as performed in Chapter 3. Again note the continuity of amplitude and trajectory, (Figure 4.9). Extrapolation to larger offsets is not performed on the ESPs for several reasons, all of which are related to difficulties in modeling extremely wide angle data. At the very large offsets present in the ESP data all the reflection events from the sediment column become very close in time and begin to interfere with one another. These reflections include several interfering reflections and diffractions from the rough sediment-crust interface, which cannot be modeled by 1-D methods. Since the data at 22 km cannot be modeled it makes little sense to extrapolate to 30 km to preserve the amplitude information at 22 km. Note also that since the trajectories at these large offsets are essentially linear, they map to a single point in the τ-p domain. Therefore amplitude errors from tapering these far offsets will be restricted to a very small area in τ-p at only the highest values of p.

For these same reasons the useful range of p in the inversion is limited to ~ 0.4 s/km. The τ-p data are therefore windowed and muted not just to eliminate reflections from outside the time window, but also to remove the crustal reflection,

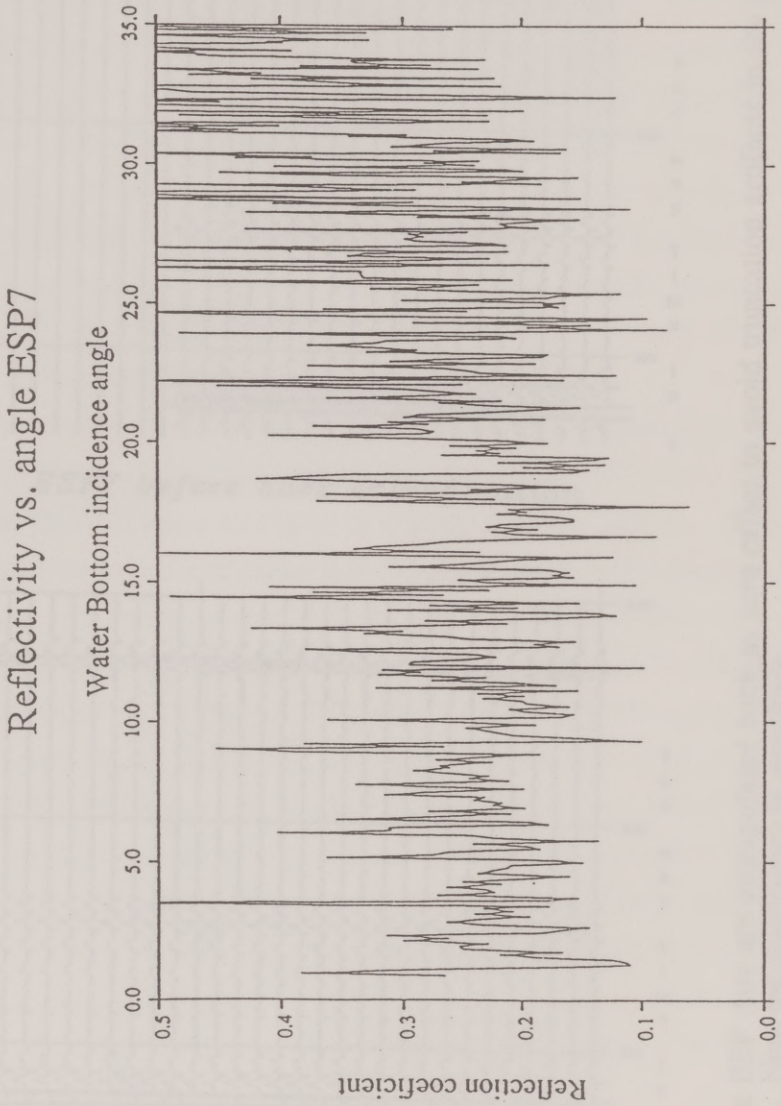

Figure 4.8. The somewhat noisy measurement of water bottom reflectivity at ESP7 show a normal incidence reflection coefficient of $0.22 \pm .2$ increasing slightly with angle.

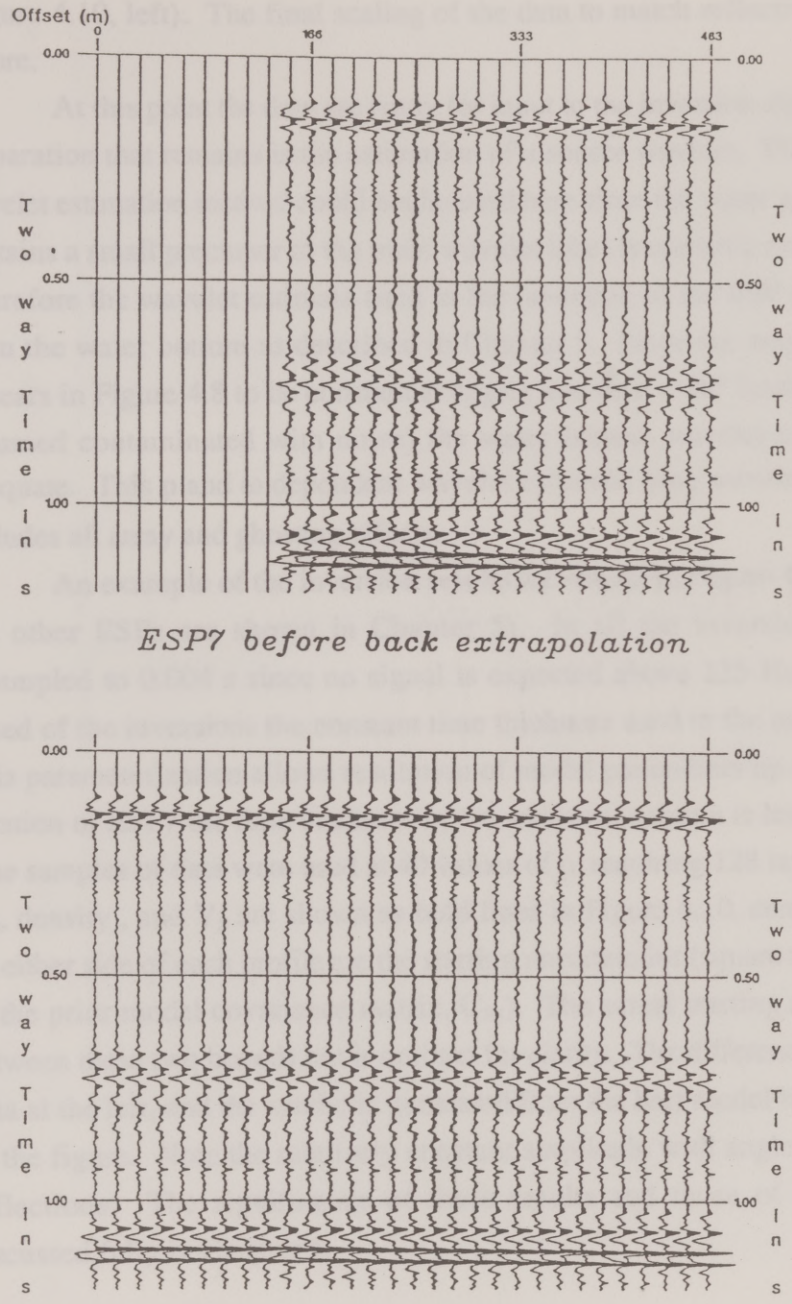

Figure 4.9 The ESP data are extrapolated back to zero offset to avoid truncation artifacts in the plane wave decomposition. Note the consistency in amplitude..

(Figure 4.10, left). The final scaling of the data to match reflectivities proceeds as before.

At this point the data are ready for input to the inversion algorithm and all the preparation that remains is the estimation of a source wavelet. The minimum phase wavelet estimation method could not be used here since the water gun wavelet (which contains a small precursor to the main wavelet lobe) is certainly not minimum phase. Therefore the wavelet estimate used in the inversion of the ESP data was obtained from the water bottom as described in Chapter 3. Since the amplitude with offset appears in Figure 4.8 to be constant at angles less than ~ 20° (and at larger angles is assumed contaminated with noise) the water bottom wavelet estimate should be adequate. This p and ω dependent wavelet estimate, (one wavelet for each p trace) includes all array and ghosting effects.

An example of the inversion results are shown in Figure 4.10, (the results of the other ESPs are shown in Chapter 5). In all the inversions the data were resampled to 0.004 s since no signal is expected above 125 Hz. To increase the speed of the inversions the constant time thickness used in the models was 0.008 s. This parameterization allows resolution of model parameters up to 62.5 Hz. At the location of ESP7 the time thickness of the sediment column is less than 1.0 s so 256 time samples of data were used at 40 values of p, requiring 128 layers. The resulting V_p, density , and V_s are shown as bold lines in Figure 4.10, center. The fine lines on either side of each profile are the starting uncertainties (square root of the diagonal of the prior model covariance matrix, C_m). The actual starting model lies midway between these two bounds but is omitted for clarity. The difference between the field data at the left, and the synthetic generated from the best model is shown at the right of the figure. Note the relatively constant amplitude with angle in all of the major reflections. The significance of these results and those of the other ESPs is discussed fully in Chapter 5.

Preparation of the MCS data for Inversion

The preparation of the MCS data proceeded in much the same manner as the ESPs and Carolina Trough data, although many more gathers were inverted. This necessitated automating the preparation and inversion of the MCS data, which

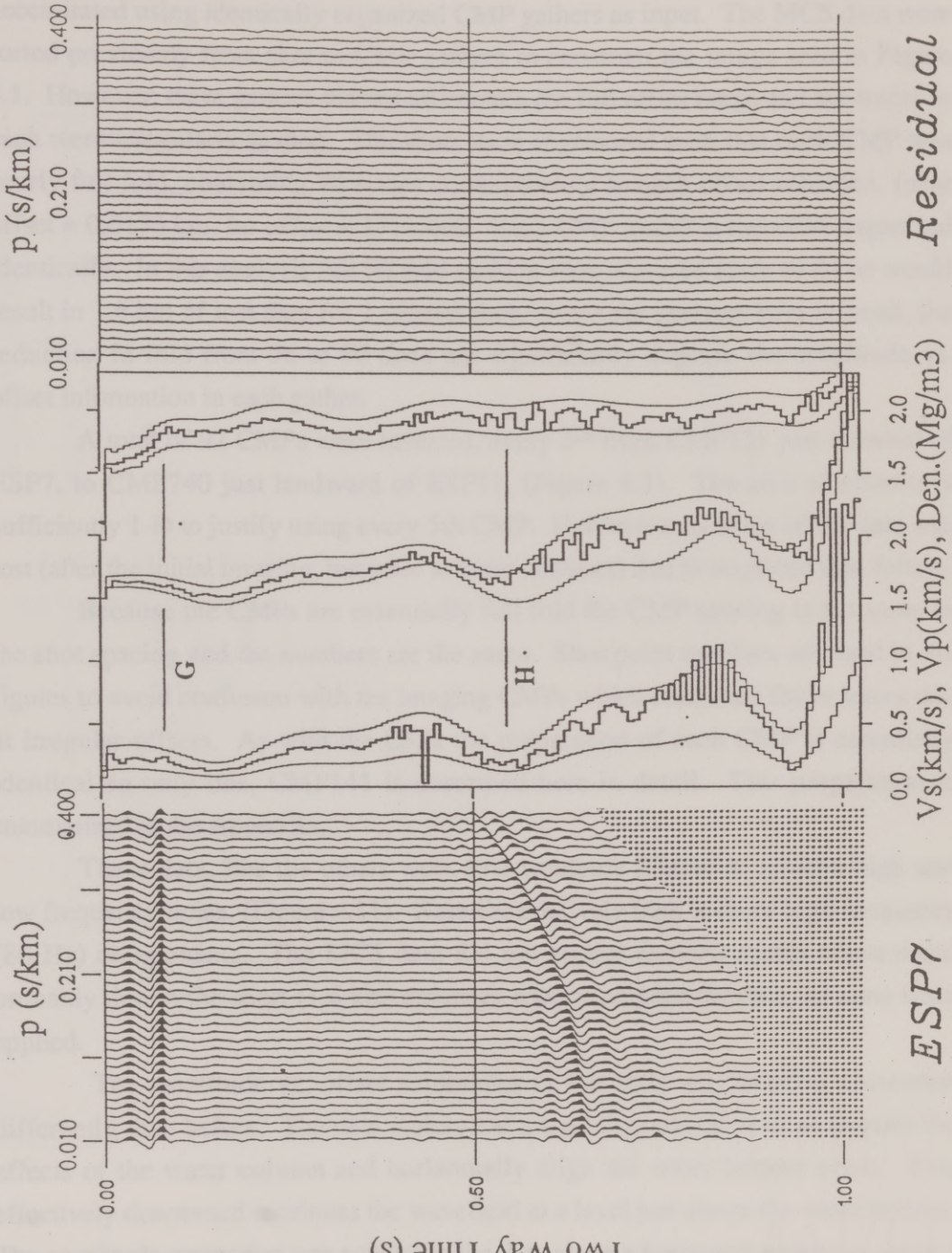

Figure 4.10 The data are ready for inversion after corrections for non ideal geometry, scaling, muting of the crustal reflection (stippled area) and wavelet estimation.

necessitated using identically organized CMP gathers as input. The MCS data were sorted previously from shot to CMP gathers to construct the image seen in Figure 4.1. However, these gathers did not all contain the full offset range and the traces in each were irregularly spaced. The shots were regathered such that each CMP was nearly full fold, containing 90 traces corresponding to each offset recorded, (near offset = 0.0133 km, far offset = 1716.666. Each CMP gather is therefore organized identically. In this analysis full 96 fold gathers were not used since to do so would result in 1.6 km of lost data for 1 missed shot. Since the aperture here is small, the reduction in fold from 96 to 90 does not significantly degrade the amplitude vs. offset information in each gather.

A total of 92 CMPs were inverted, every 5th from CMP131 just seaward of ESP7, to CMP740 just landward of ESP17, (Figure 4.1). The area of interest is sufficiently 1-D to justify using every 5th CMP. Unfortunately some of the data was lost (after the initial imaging, but prior to these analyses) due to magnetic tape failure.

Because the CMPs are essentially full fold the CMP spacing is the same as the shot spacing and the numbers are the same. Shot point numbers are used in the figures to avoid confusion with the imaging CMPs which contained fewer traces and at irregular offsets. As with the ESPs the preparation of each CMP is essentially identical so only one, CMP141 is described here in detail. This preparation is summarized in the Appendix.

These data, like the others were first bandpass filtered to remove high and low frequency noise, (Figure 4.11). Note the relatively high level of high frequency (80 Hz) components. The MCS data did not appear to need statics corrections, probably due to the short (1.6 km) streamer used to acquire the data, so none were applied.

The amplitude vs. offset smoothing of this data was handled somewhat differently than before. The data underwent a static hyperbolic shift to remove the effects of the water column and horizontally align the water bottom event. This effectively downward continues the wavefield to a level just above the water bottom. The amplitude correction was applied to the data along a horizontal trajectory using a window which included the entire sediment column. Traces whose amplitude had to be adjusted by more than 50% were removed. They were replaced by a linear,

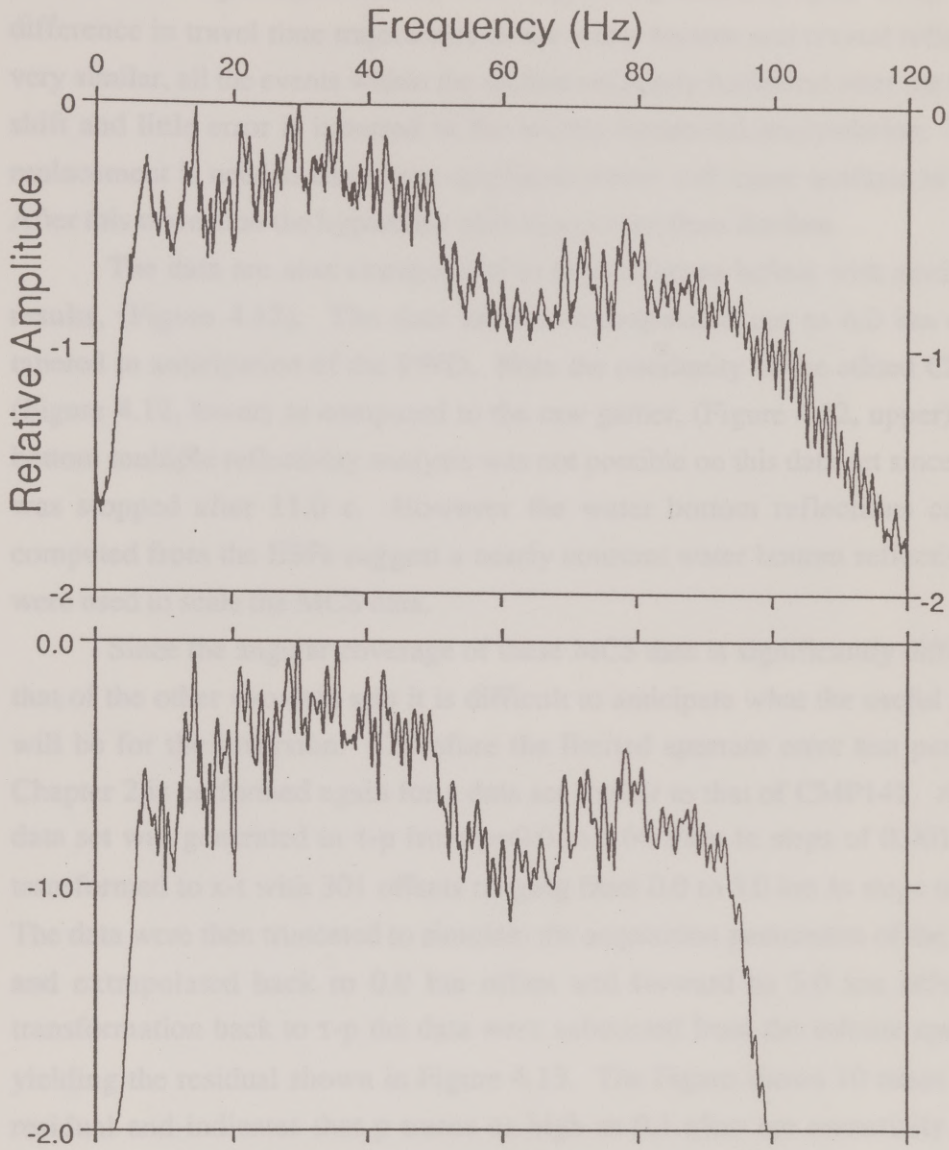

Figure 4.11 The amplitude spectrum of CMP141 before (upper) and after (lower) bandpass filtering. Note the significant amplitude at frequencies up to 80 Hz.

horizontal, interpolation from the two neighboring traces, (Figure 4.12). Since the difference in travel time trajectories of the water bottom and crustal reflections are very similar, all the events within the section are nearly horizontal after the hyperbolic shift and little error is incurred in the strictly horizontal interpolation. This trace replacement is needed since zero amplitude traces will cause artifacts in the PWD. After this correction the hyperbolic shift is removed from the data.

The data are next extrapolated to zero offset as before with similarly good results, (Figure 4.12). The data are also extrapolated out to 6.0 km offset and tapered in anticipation of the PWD. Note the continuity of the edited CMP gather (Figure 4.12, lower) as compared to the raw gather, (Figure 4.12, upper). A water bottom multiple reflectivity analysis was not possible on this data set since recording was stopped after 11.0 s. However the water bottom reflections coefficients computed from the ESPs suggest a nearly constant water bottom reflectivity which were used to scale the MCS data.

Since the angular coverage of these MCS data is significantly different from that of the other two data sets it is difficult to anticipate what the useful range of p will be for the inversion. Therefore the limited aperture error test performed in Chapter 2 is performed again for a data set similar to that of CMP141. A synthetic data set was generated in τ-p from p=0.0 to 0.66 s/km in steps of 0.001 s/km and transformed to x-t with 301 offsets ranging from 0.0 to 5.0 km in steps of 0.01666. The data were then truncated to simulate the acquisition parameters of the MCS data and extrapolated back to 0.0 km offset and forward to 5.0 km offset. After transformation back to τ-p the data were subtracted from the infinite aperture data yielding the residual shown in Figure 4.13. The Figure shows 10 times the actual residual and indicates that p traces as high as 0.1 s/km are essentially free from limited aperture artifacts. This is largely what is expected since an offset of 1.7 km located 4.8 km above a target gives a 10.0° incidence angle, corresponding to p = 0.11 s/km.

Since the MCS data were acquired using an air gun array (a minimum phase source) the wavelet used in the inversion of the MCS data was estimated by the minimum phase method discussed in Chapter 3. However, since the offset range for this data is narrow, no large changes in amplitude with offset are expected, and the

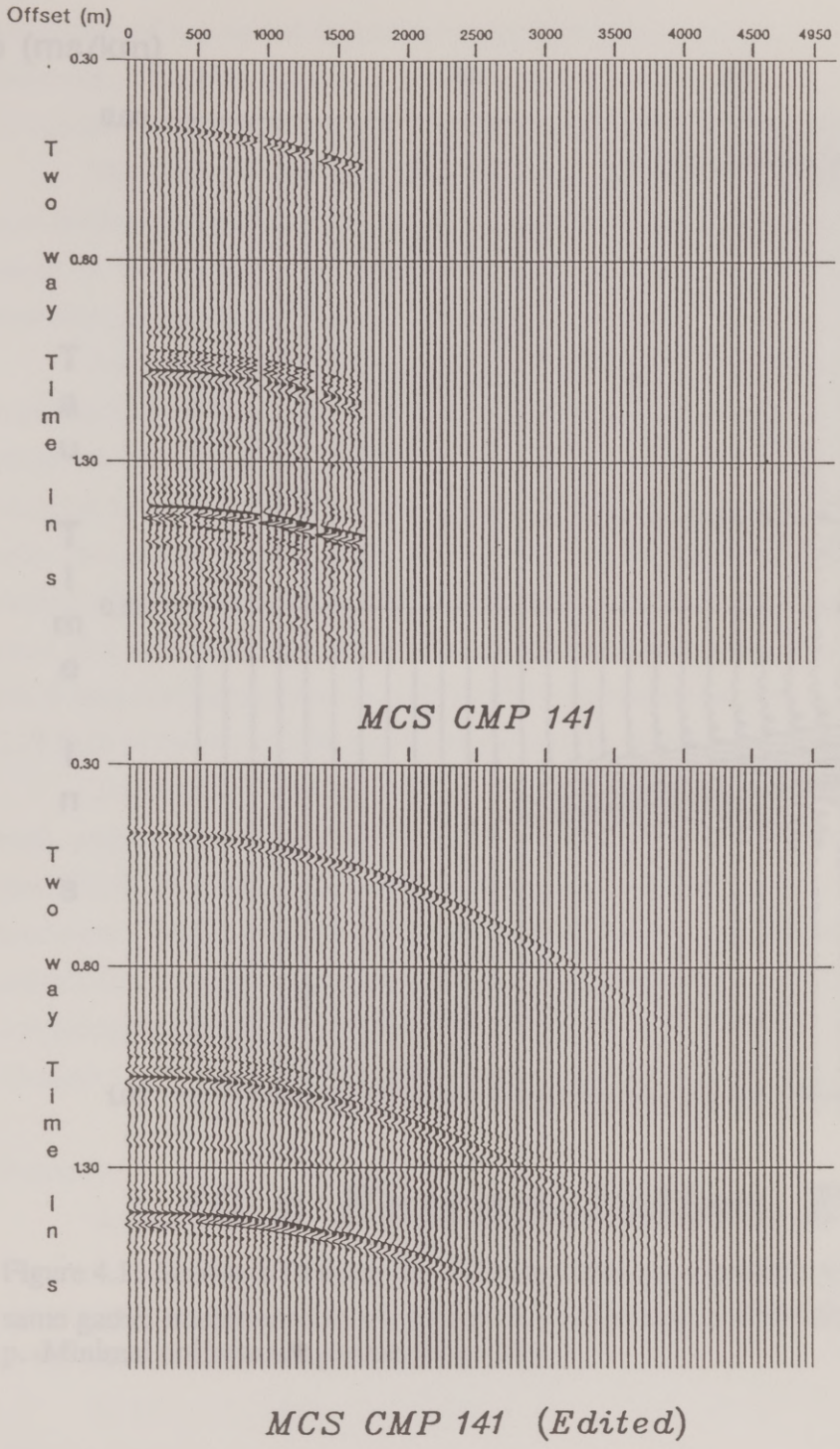

Figure 4.12 Every third trace of CMP141 is shown before (upper) and after (lower) amplitude equalization, bad trace replacement, extrapolation to smaller and larger offsets, and tapering of the far offsets to avoid PWD artifacts. Note the general improved appearance of the edited data.

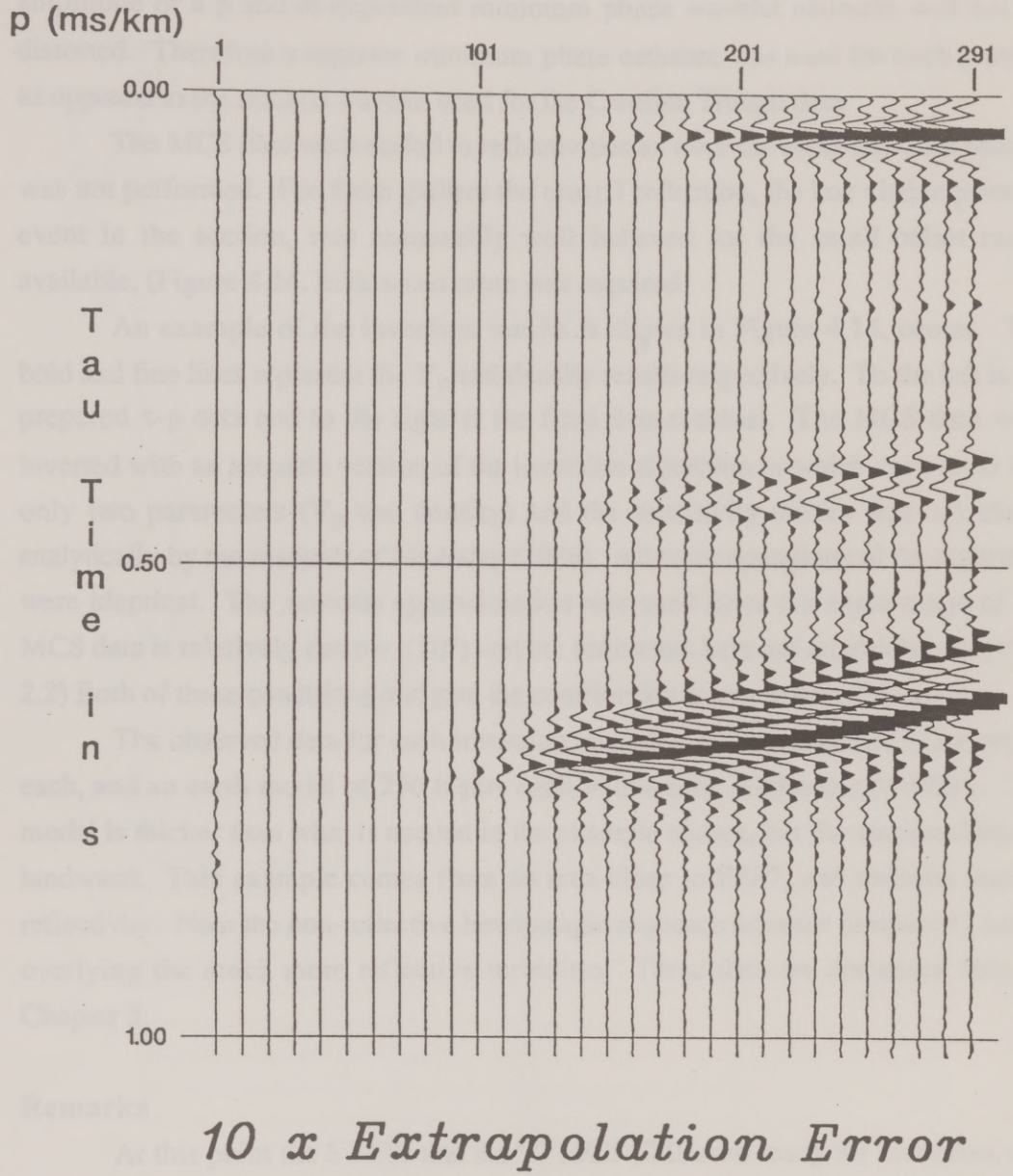

Figure 4.13 Shown is 10 times the difference between a synthetic τ-p gather and the same gather transformed to x-t, truncated, extrapolated, and transformed back to τ-p. Minimal artifacts are present for $p < 0.1$.

amplitude of a p and ω dependent minimum phase wavelet estimate will not be distorted. Therefore a separate minimum phase estimate was used for each p trace, as opposed to the stacked wavelet used for the Carolina Trough data.

The MCS data were scaled to reflectivities as were the other data, but muting was not performed. For these gathers the crustal reflection, the last visible primary event in the section, was reasonably well behaved for the small offset range available, (Figure 4.14, left), so no mute was required.

An example of the inversion results is shown in Figure 4.14, center. The bold and fine lines represent the V_p and density results respectively. To the left is the prepared τ-p data and to the right is the final data residual. The MCS data were inverted with an acoustic version of the inversion algorithm in which each layer had only two parameters (V_p and density) and the sensitivity matrix was calculated analytically by the methods of McAulay (1986). All other operations of the algorithm were identical. The acoustic approximation was used since the angle range of the MCS data is relatively narrow, (10°) and the sediments here are relatively soft ($V_p <$ 2.2) Both of these conditions mitigate the contribution from converted S waves.

The observed data for each inversion consisted of 10 p traces of 512 samples each, and an earth model of 256 layers each with a time thickness of 0.008 s. The model is thicker than what is needed in the example shown, but the section thickens landward. This example comes from an area close to ESP7, and exhibits similar reflectivity. Note the non-reflective hemipelagic sequence between horizons G and H overlying the much more reflective turbidites. These data are discussed fully in Chapter 5.

Remarks

At this point the 8 ESPs and the 92 MCS CMPs are ready for inversion, and the background model has been created. For each of these gathers there is a corresponding p and ω dependent wavelet obtained from the water bottom in the case of the ESPs or from the minimum phase estimate in the case of the MCS data.

In the next chapter the results of the inversion are discussed in detail. The ESP data were analyzed first providing the more accurate sediment property profiles at 5 locations along the toe of the wedge. Between these sites the MCS data provide

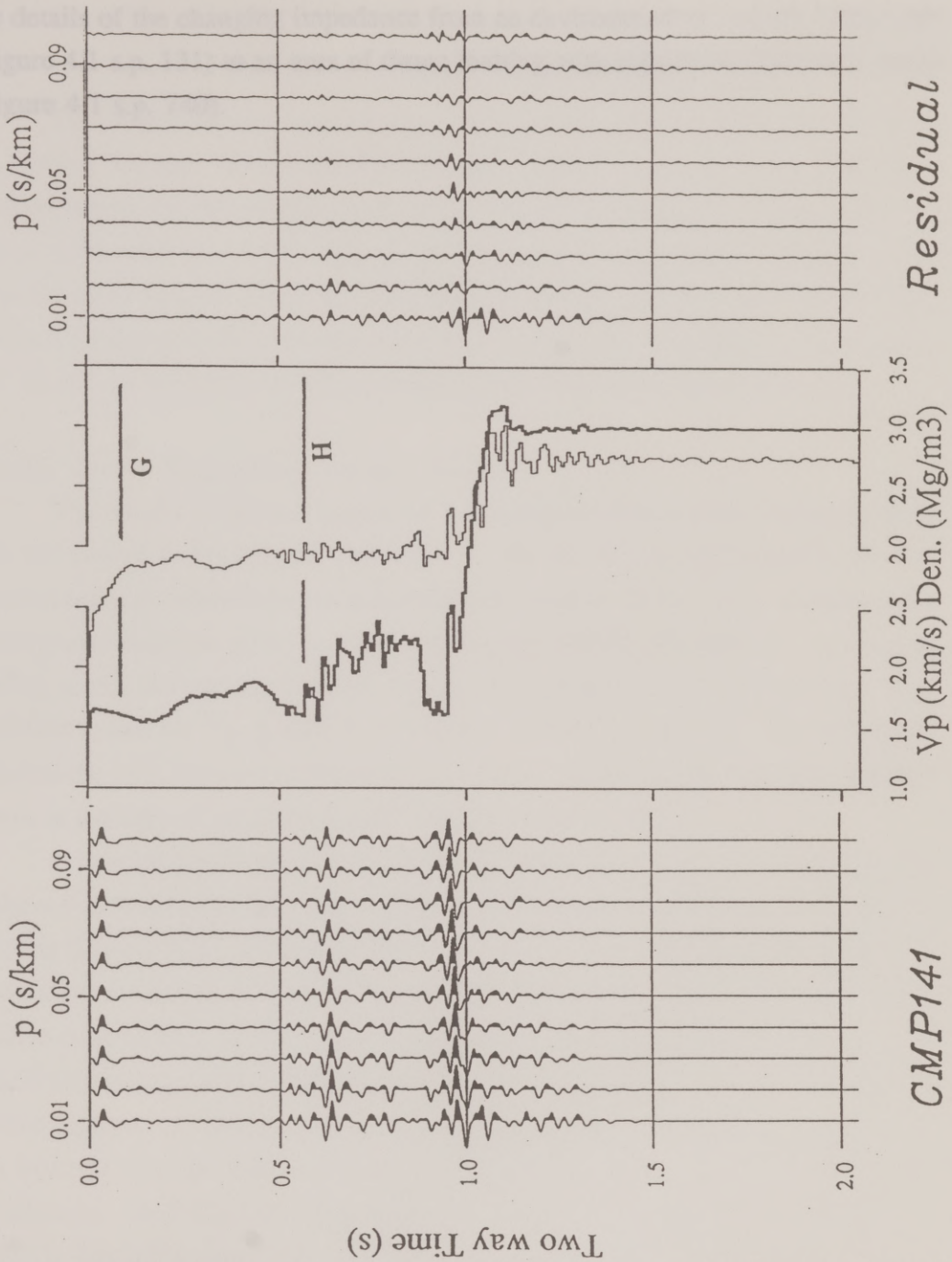

Figure 4.14 After scaling CMP141 is ready for inversion. muting is not performed since the small offset range does not allow strong 2 or 3-D character from the crustal reflection.

the details of the changing impedance from an environment of vertical stress only, (Figure 4.1 s.p. 131) to an area of thrust faulting with significant horizontal stress, (Figure 4.1 s.p. 740).

Chapter 5
Elastic Parameter Cross Sections

The waveform inversion was next applied to the prepared ESPs and CMPs of the Nankai Trough. These results form the basis of the elastic parameter cross sections across the deformation front of the Nankai accretionary wedge. Between and on either side of the ESP sites, inversion results from the MCS data are used to fill in the cross section. These small aperture data are not as useful for discriminating between different kinds of elastic parameter changes, but when constrained by the ESP results are useful in laterally correlating properties across the wedge toe.

Results From Expanding Spread Profiles

The results of the full waveform 1-D elastic inversion of the Nankai trough data are shown in Figures 5.1 through 5.7. On the left of each figure is the τ-p transformed and reduced data as described in Chapter 4. In the center are shown the starting uncertainties given as upper and lower bounds, (fine lines). The actual starting model lies midway between these two bounds but is omitted for clarity. The inversion result for V_p, ρ, and V_s is shown as the bold solid line. The difference between the field data at the left, and the synthetic generated from the best model is shown at the right of each figure (ESP7 is shown in Figure 4.10).

It is helpful to discuss these results and those of the MCS data in the context of the major features of the wedge toe seen in the seismic data (Figure 4.1) and line drawing (Figure 4.2). Seaward of ESP7, the sediment column consists mostly of a moderately reflective Pliocene turbidite sequence ~0.4 km thick deposited on the oceanic crust (Karig, 1987). The boundary between this sequence and an interval of seismically transparent Shikoku basin hemipelagic mudstone also ~0.4 km thick is labeled horizon "H" (horizon labels are consistent with Kagami et al., 1987) It is to this horizon that the first major thrust faults sole out making it the subduction decollement. Over this lies a seismically transparent hemipelagic sequence the top of which is labeled horizon "G". This horizon is marked by an unconformity rather than a reflection. It is the seaward section between G and H in which a large low V_p zone exists.

Landward of ESP7 Pleistocene trench fill sediments unconformably overlay the hemipelagic sequence. This sequence thickens landward and is divided in the seismic data by a strong reflector labeled horizon "C" shown in Figures 4.1 and 4.2.

ESP7

The data of this gather were modeled exceptionally well as indicated by the near absence of elliptical events in the data residual, (Figure 4.10). The model estimate shown in Figure 4.10 is rather smooth through the seismically transparent hemipelagic sediments between horizons G and H, (except for a spurious layer of low V_S). The more reflective Pliocene turbidites, below horizon H yield a model estimate consisting of several zones of alternating impedance. The impedance is divided among the three model parameters according to their relative values of C_m. The V_P difference between the zones is 0.3 km/s, the V_S difference is ~0.25 km/s and the density difference is ~0.2 Mg/m3. These values are all reasonable for sediment at this depth and each of these cycles may represent one turbidity flow. The high frequency oscillations in the model below ~ 0.8 s sub-bottom are not valid since the data beyond this time were muted. Note the ~ 0.3 km/s V_P reversal just above H and the slightly higher velocity of sediments below this horizon compared to those above.

ESP9

The data here are also modeled quite well (Figure 5.1), but because of some source problems the useful p range of ESP9 was limited to 0.26 s/km. Like ESP7 the model consisted of 128 elastic layers each 0.008 s thick, and the data consisted of 256 time samples each 0.004 s apart. Note the much lower reflectivity of the sediments below horizon H. Again H corresponds to the lower interface of a low V_P zone.

Higher in this section the trench fill sediments, especially those between horizons C and G show a similar oscillating elastic parameters exhibited in the turbidite sequence at ESP7. V_S data from this smaller angle range data is not reliable.

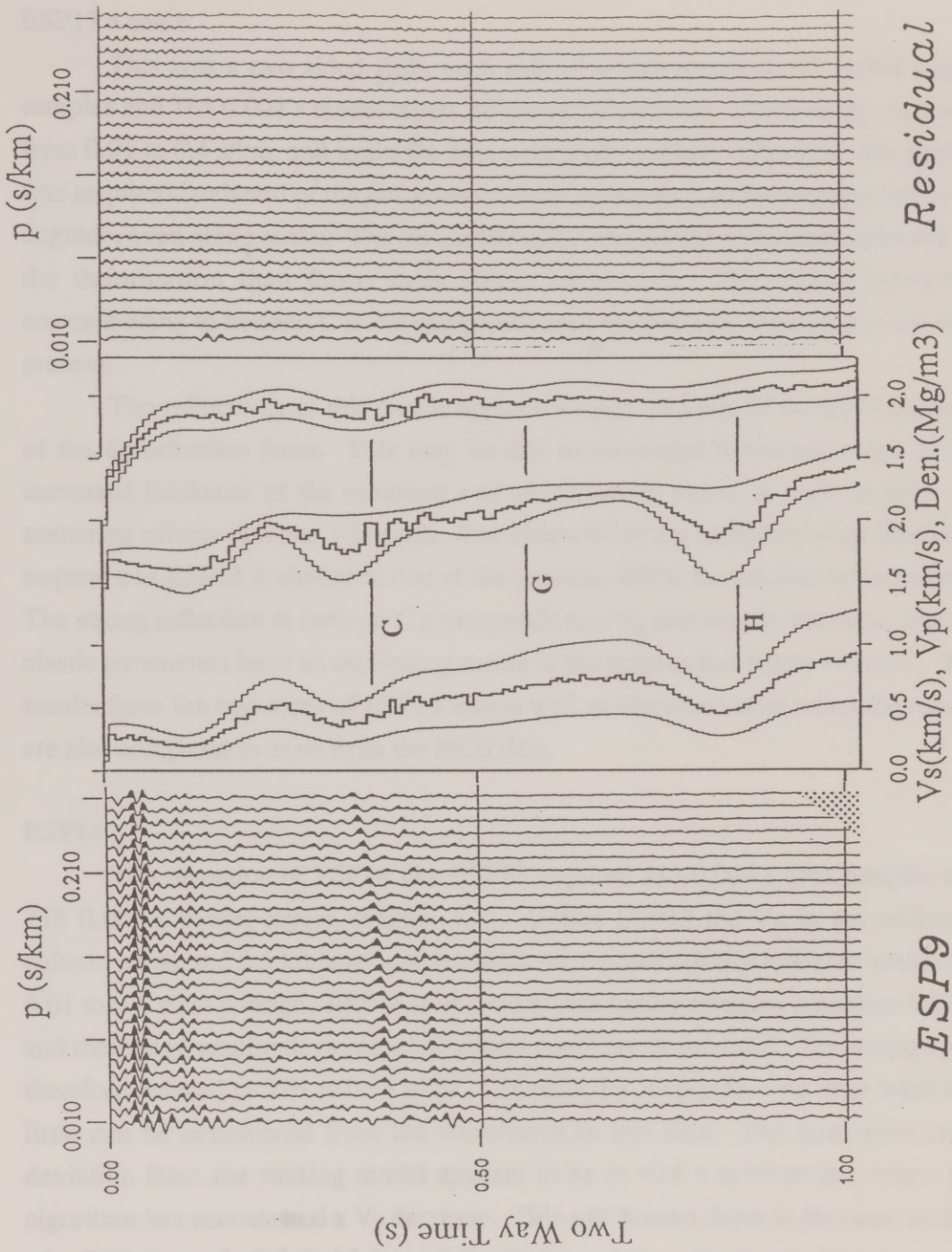

Figure 5.1. The inversion of ESP9 used 26 p traces with 256 samples each and 128 model layers. Note the V_p increase at horizons C and H, the correlated V_p and density between C and G and also below H.

ESP13 a and b

This was a two sided ESP, each side of which required 512 0.004 s data samples and 165 0.008 s model layers, (Figures 5.2 and 5.3). The p range used was from 0.01 to 0.4 s/km, and again the data were well matched. However, this profile was acquired landward of the deformation front where the 1-D assumption begins to degrade, even along strike. The trench fill sediments appear to be more affected by the deformation than those units below horizon G. The strong reflection corresponding to horizon C is not completely reproducible and some data residual is present.

The reflectivity of this profile appears weaker than that of the ESPs seaward of the deformation front. This may be due to increased lithification due to the increased thickness of the sediment and added lateral stress, as well as from the scattering effects of a non 1-D earth. The character of the model for each lithologic sequence in ESP13 is similar to that of the previous ESPs, but smaller in magnitude. The strong reflection at horizon C corresponds to a V_p and density increase, and the elastic parameters have an oscillating nature in the regions just below H and C. The results from the two sides of ESP13 match well as discussed later when the results are also compared to those from the MCS data.

ESP14

The inversion of ESP14 like ESP13 required 512 0.004 s data samples and 218 0.008 s model layers, (Figure 5.4). Unlike ESP13 the V_p in the sediment column surpassed 2.5 km/s and some events were post critically reflected within the 0.01 to 0.4 s/km p range. ESP14 is in a more structurally complex area than ESP13 and these high amplitude post critical events could not be modeled. The p range was therefore reduced to 0.01 to 0.35 s/km. The reflection events here are very weak and little can be determined from the waveforms in this data. The most prominent deviation from the starting model appears to be at ~0.6 s sub-bottom, where the algorithm has accentuated a V_p decrease. This sub-bottom depth is the same as that of a BSR located slightly higher on the wedge, where a V_p decrease is expected, (Figure 4.2). However, because of the low signal level the result is somewhat surprising.

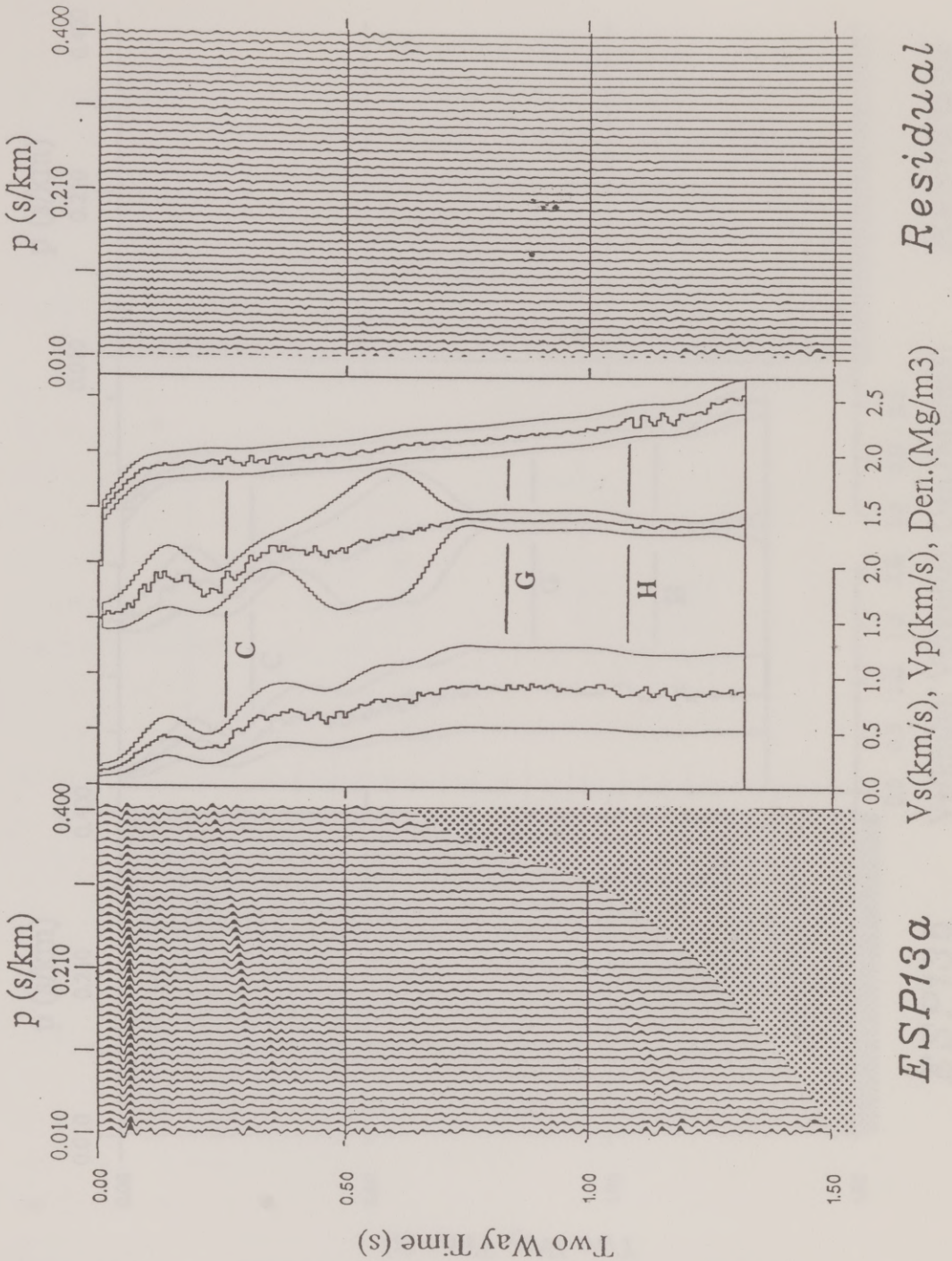

Figure 5.2. The inversion of ESP13 (both a and b) used 40 p traces of 512 samples each and 160 model layers. These results show a somewhat more pronounced Vs correlated than in ESP9.

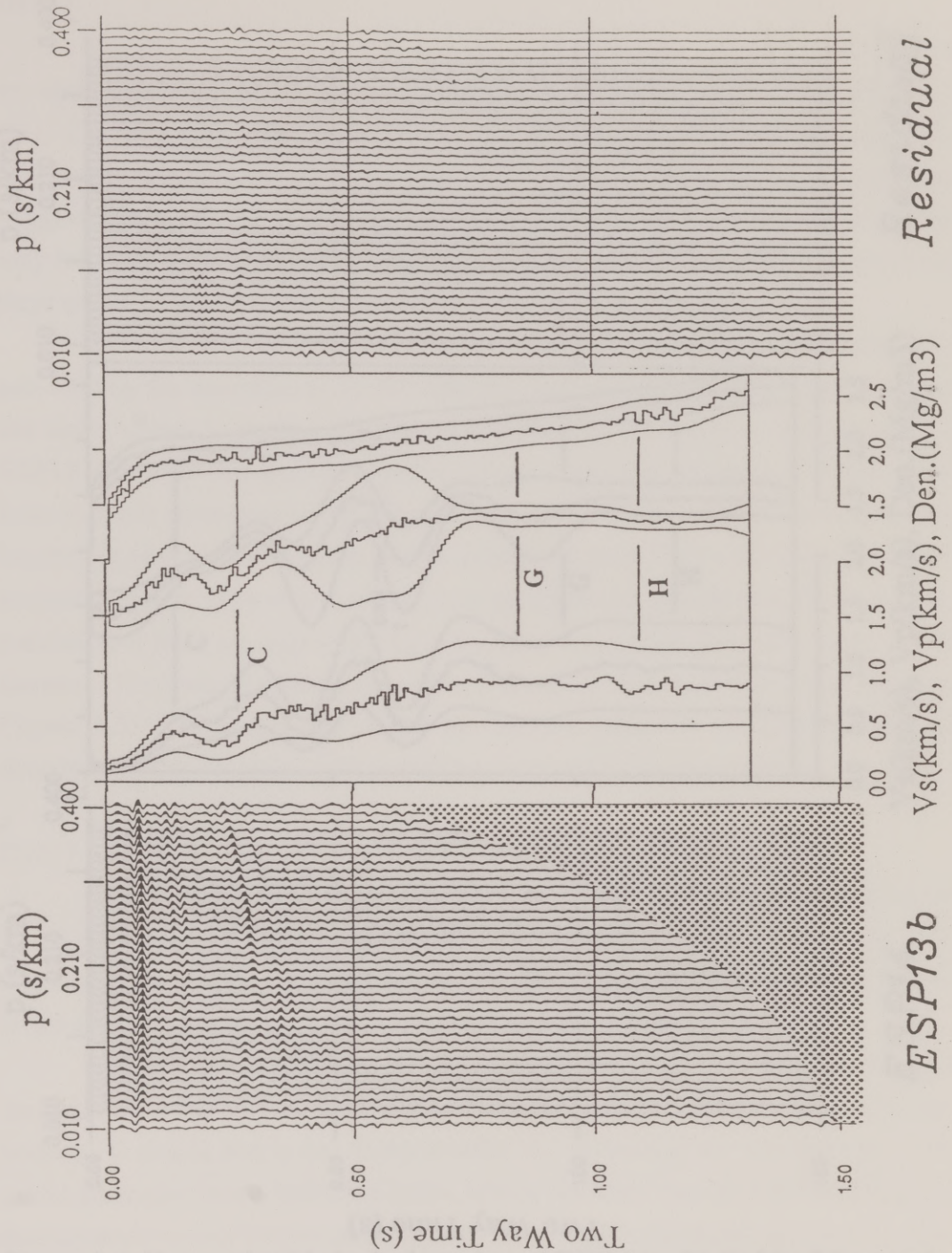

Figure 5.3. These results of ESP13b are consistent with those of ESP13a. The model result and the data residual are very similar.

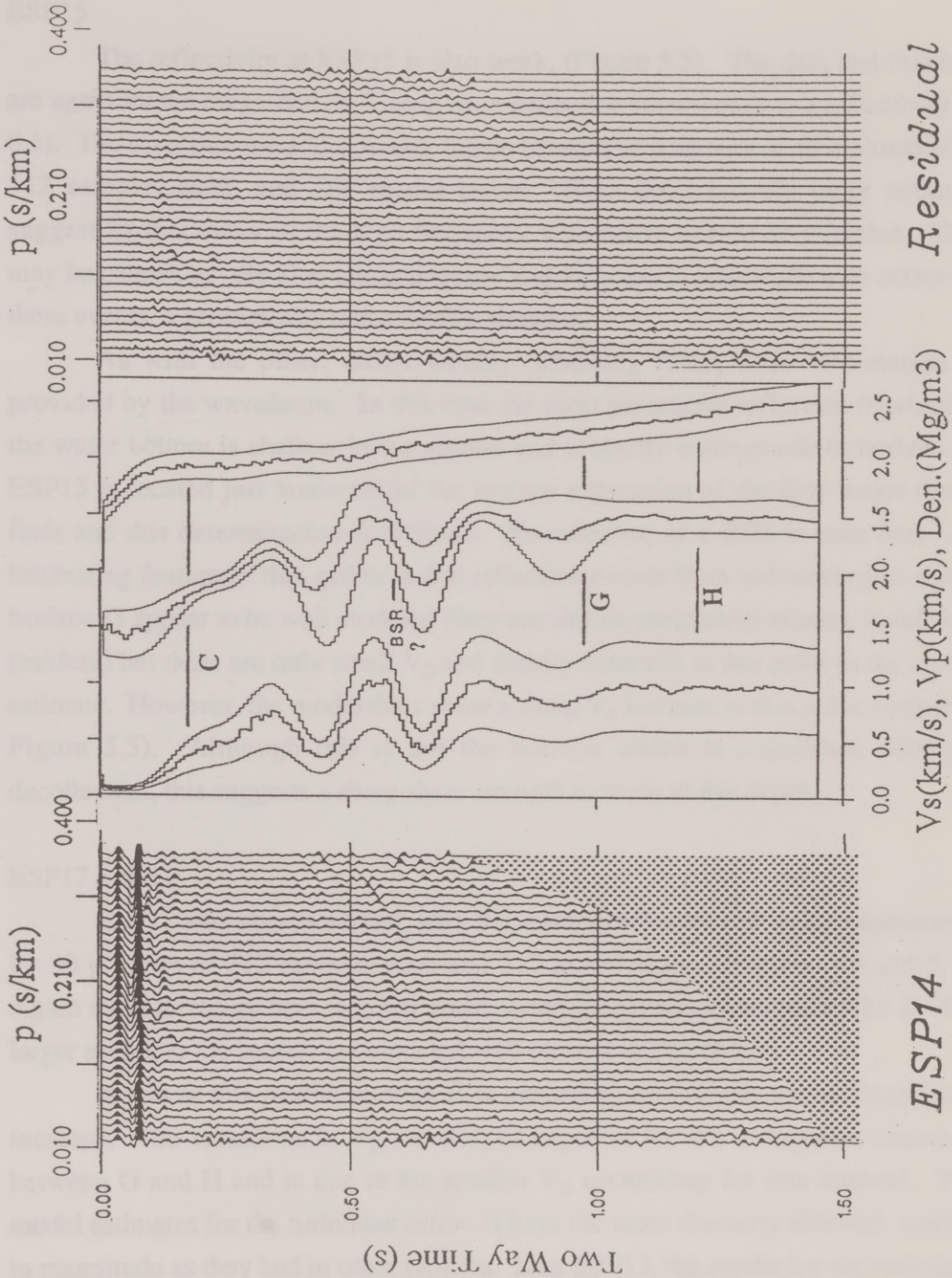

Figure 5.4. Very noticeable in the inversion of ESP14 (multiplied by 2 here so 1 trace deflection corresponds to a reflection coefficient of 0.1) is the lack of strong reflections, and subsequent lack of significant deviation in the result from the starting model.

ESP15

The reflectivity at ESP15 is also weak, (Figure 5.5). The data and residual are again shown magnified by 2, (one trace deflection corresponds to a reflectivity of 0.1). The inversion used 35 p traces, (again because of post critical reflections) with 512 samples each, and 190 model layers. Note the relatively large residual suggesting that many of the high frequency waveforms cannot be modeled. This may be caused by the alternating increase and decrease in amplitude with offset on these events, a geologically unreasonable situation.

As with the other, rather weakly reflecting ESPs, little information is provided by the waveforms. In this case the most prominent reflection (excluding the water bottom is shallow in the section and probably corresponds to horizon C. ESP15 is located just landward of the surface expression of the first major thrust fault and this determination is difficult. No evidence of a BSR is seen here. An interesting feature of this gather is that reflection events from sediments just above horizon G appear to be well modeled (they are almost completely missing in the data residual) but there are only small V_p and density contrasts at this point in the model estimate. However, the model does show a sharp V_s increase at this point, (arrow in Figure 5.5). Although this is not the horizon which is coincident with the decollement, this suggests a sharp shear strength increase at this depth.

ESP17 a and b

ESP17 was also two sided, with the inversion of each side being represented by 30 p traces of 512 samples each and 218 model layers, (Figures 5.6 and 5.7). Again the reflectivity here is rather weak so the data is shown magnified by 2. The larger events in the section are modeled well (arrows in Figure 5.6).

Again in this profile horizon C is located by a relatively strong impedance increase. The variations in V_p are low, as expected for the transparent sequence between G and H and is due to the smaller V_p uncertainty for this interval. The model estimates for the turbidites below H have the same character although smaller in magnitude as they had in other profiles. Like ESP13, the results for the two sides of ESP17 match quite closely.

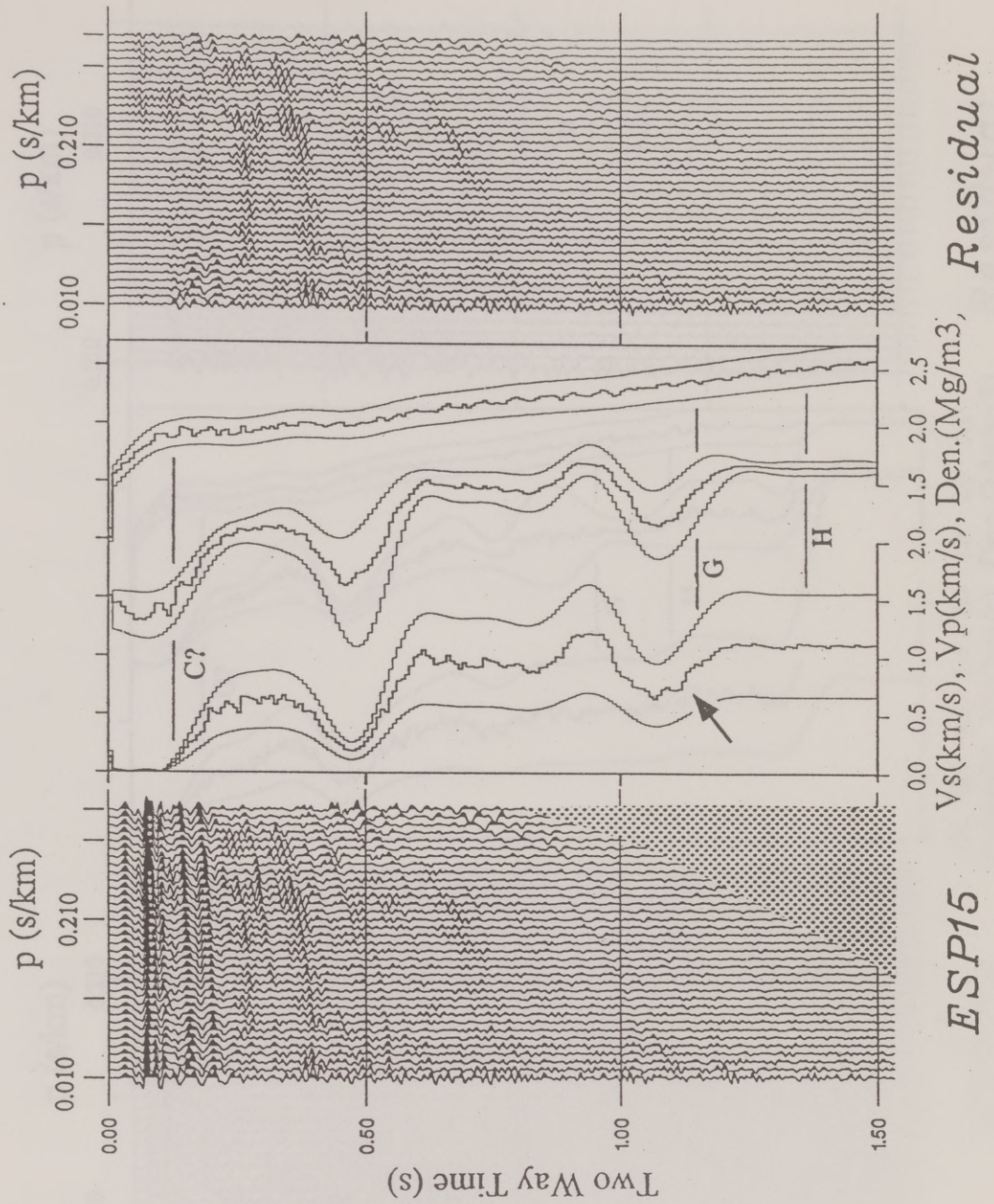

Figure 5.5. Again multiplied by 2, ESP15 is similarly weakly reflective. The arrow shows an example of one of the few V_S contrasts.

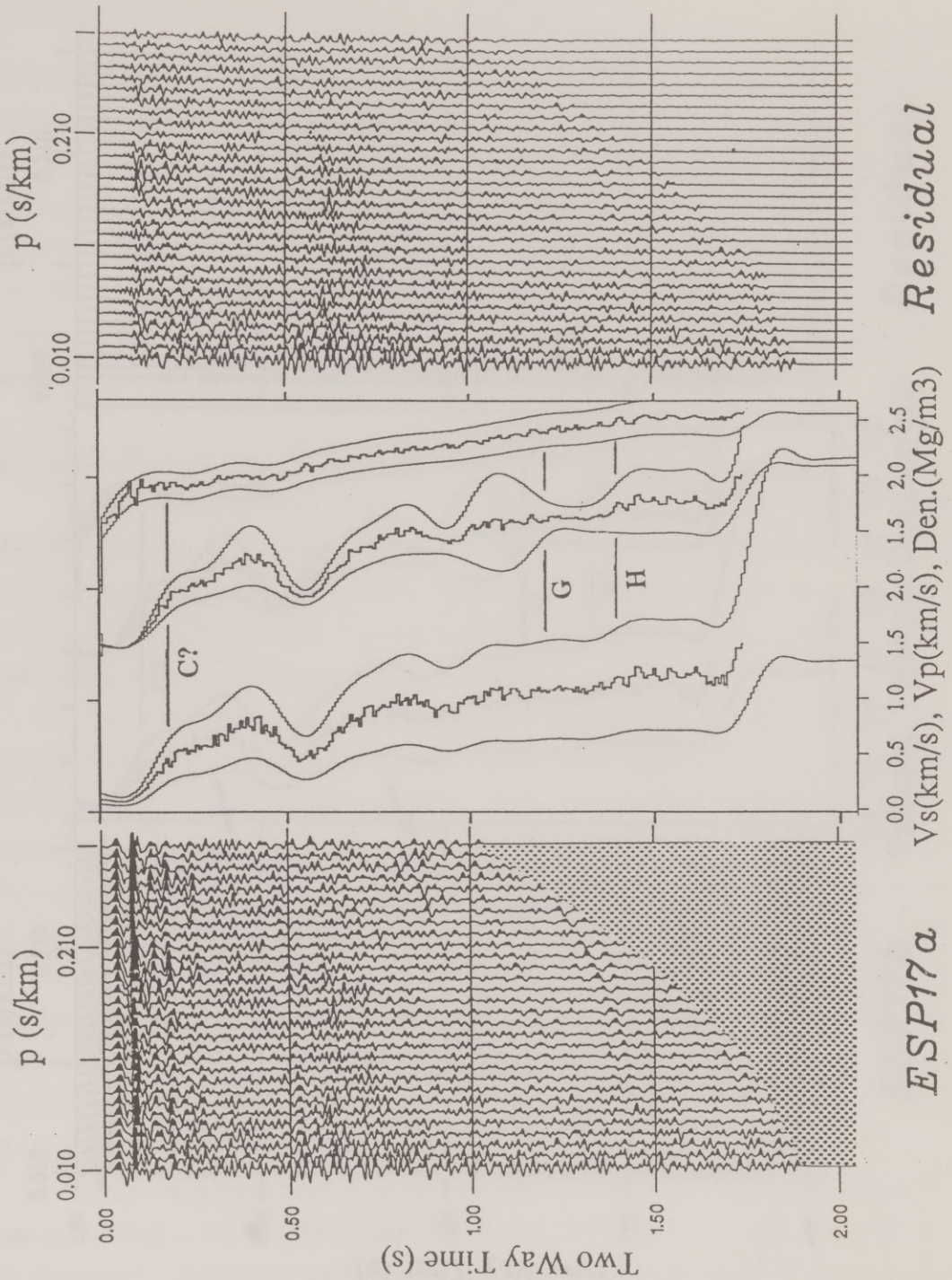

Figure 5.6. At ESP17, (shown here x 2) the signal to noise ratio is ~ 1.0 , and model results are correspondingly uncertain.

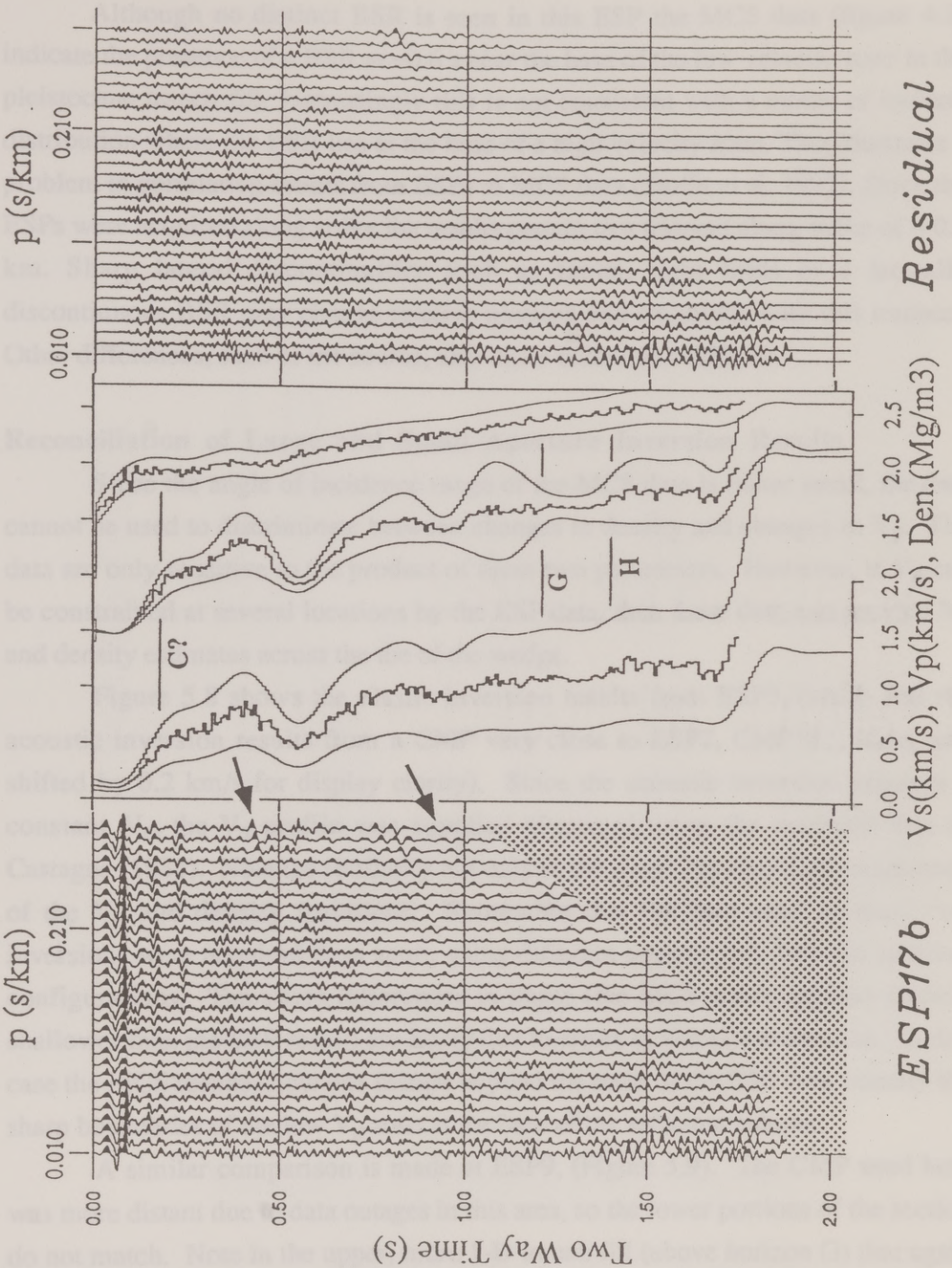

Figure 5.7 Some events in ESP17a and b were modeled much better than others. The arrows show events for which no remnants are seen in the data residual.

Although no distinct BSR is seen in this ESP the MCS data (figure 4.2) indicate the presence of a BSR at ~0.6 s near the base of the low velocity zone in the pleistocene trench fill. Interestingly this is not consistent with a model of hydrate distribution where the BSR lies at the base of a high velocity zone. This illustrates a problem in correlating events from ESPs to MCS data (Stoffa et al. 1992). Since the ESPs were acquired along strike the results pertain to a transect along strike of ~ 0.8 km. Sharp lateral discontinuities such as faults, tight folds or a laterally discontinuous BSR may change relative position and amplitude over this transect. Other differences, such as the source, also make correlation difficult.

Reconciliation of Large and Small Aperture Inversion Results

Since the angle of incidence range of the MCS data is rather small, the data cannot be used to discriminate between changes in density and changes in V_p. The data are only sensitive to the product of these two parameters. However, if V_p can be constrained at several locations by the ESP data, then these data can provide V_p and density estimates across the toe of the wedge.

Figure 5.8 shows the elastic inversion results from ESP7, (bold) and the acoustic inversion results from a CMP very close to ESP7, CMP151, (fine, and shifted by 0.2 km/s for display clarity). Since the acoustic inversion assumes a constant V_S, the V_S profile was supplied afterward using the mudrock line of Castagna (1985). Note the similarity not only in the shape but also in the magnitude of the V_p and density variations. Remember that the data used in these two inversions were acquired days apart, using different sources and different receiver configurations. The slight differences in phase (the MCS result appears slightly shallower than the ESP result) are likely due to errors in wavelet estimation. In this case the MCS results show one feature beyond the mute of the ESP data, namely the sharp boundaries of the low V_p zone at the base of the sediment column.

A similar comparison is made at ESP9, (Figure 5.9). The CMP used here was more distant due to data outages in this area, so the lower portions of the section do not match. Note in the upper, more 1-D trench fill (above horizon G) that again the shape and magnitude of the ESP and MCS results are very similar, particularly in the area of strongest reflectivity, i.e. above horizon G.

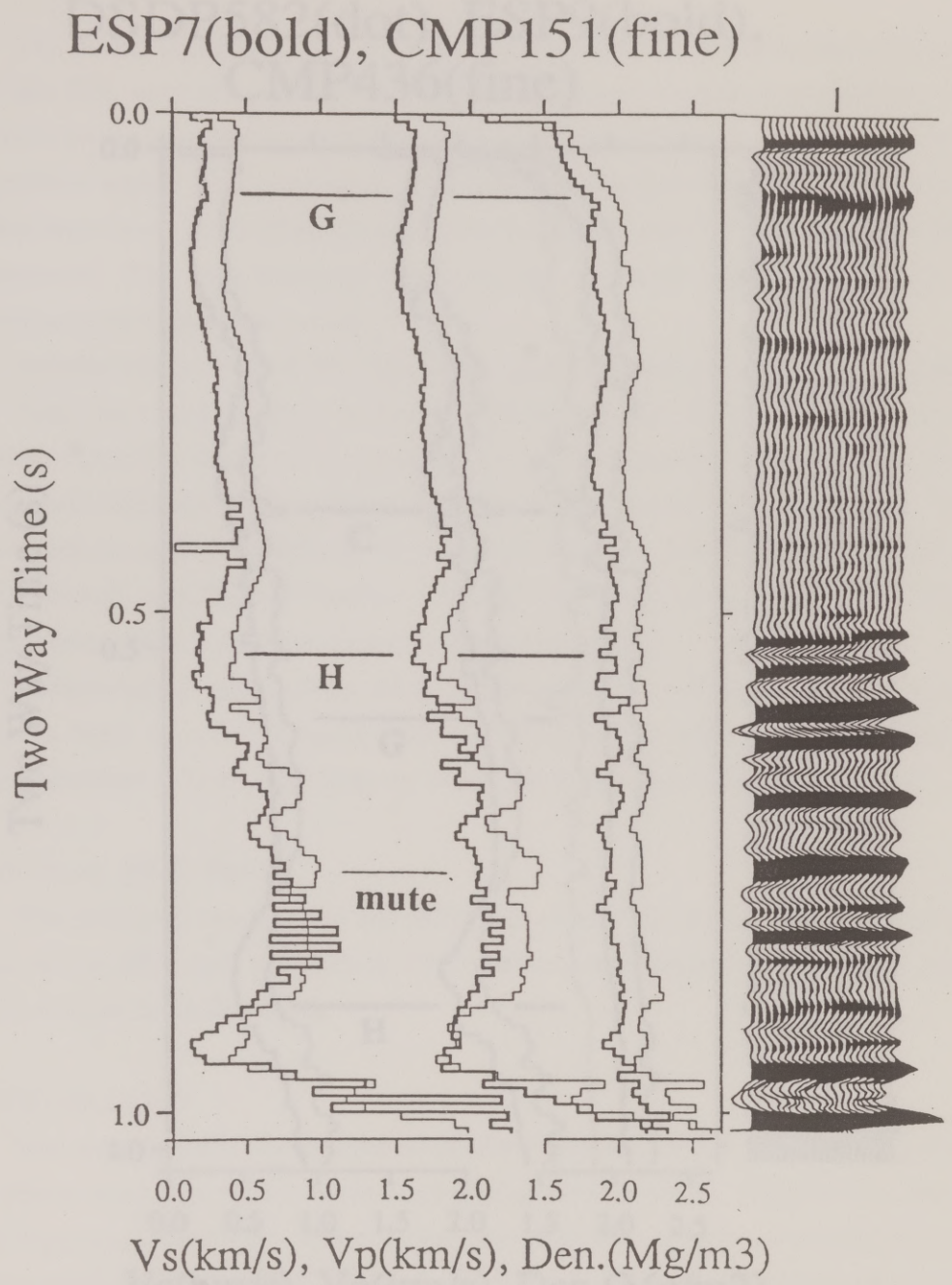

Figure 5.8. Results from the MCS data (fine, shifted) compare favorably with those from ESP7, (bold). At the right of figures 5.8 through 5.10 is a portion of the migrated MCS data from the location of the ESP. Note here the large change in reflectivity at horizon H.

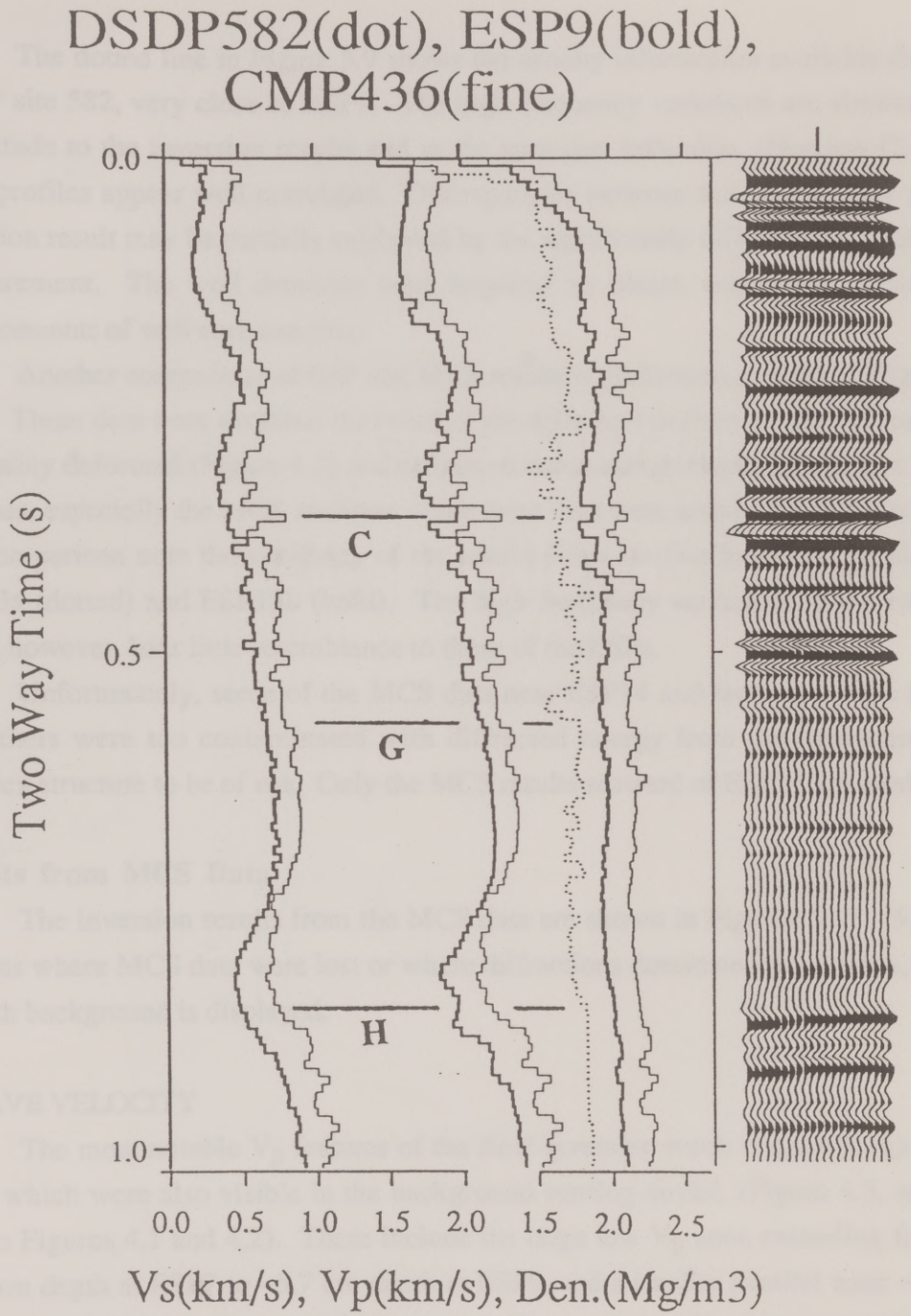

Figure 5.9. ESP9 results, (bold) and MCS results, (fine, shifted right) from several km down dip, (due to data loss) are very consistent above horizon G. The well core density measurements from DSDP 582 (dot, shifted left) are not as consistent.

The dotted line in Figure 5.9 shows the density information available from DSDP site 582, very close to ESP9. The high frequency variations are similar in magnitude to the inversion results and at the strongest reflection, (Horizon C) all three profiles appear well correlated. Discrepancies between the well density and inversion result may be partially explained by the significantly different methods of measurement. The well densities were acquired by direct, weight and volume measurements of well core samples.

Another comparison of ESP and MCS results is performed at ESP13, (Figure 5.10). These data were acquired landward of the deformation front where sediments are visibly deformed (Figure 4.1) and diffracted wave energy begins to degrade the analyses, especially the MCS analyses, since these data were acquired along dip. In this comparison note the similarity of the results from the two halves of the ESP, ESP13a (dotted) and ESP13b (bold). The high frequency variations in the MCS result, however, bear little resemblance to those of the ESPs.

Unfortunately, some of the MCS data near ESP14 and landward were lost and others were too contaminated with diffracted energy from the increasingly complex structure to be of use. Only the MCS results seaward of ESP14 are used.

Results from MCS Data

The inversion results from the MCS data are shown in Figures 5.11 - 5.12. In areas where MCS data were lost or where diffractions dominated the section, the smooth background is displayed.

P-WAVE VELOCITY

The most notable V_p features of the final inversion result (Figure 5.11) are those which were also visible in the background starting model, (Figure 4.3, refer also to Figures 4.1 and 4.2). These include the large low V_p zone extending from ~5.4 km depth at ESP7 to ~5.7 km depth at ESP9, and a smaller parallel zone ~0.4 km deeper at the base of the sediment column. The upper low V_p zone is coincident with the seismically transparent Shikoku basin hemipelagic sequence, the bottom of which (horizon H) is coincident with the subduction decollement landward of s.p.

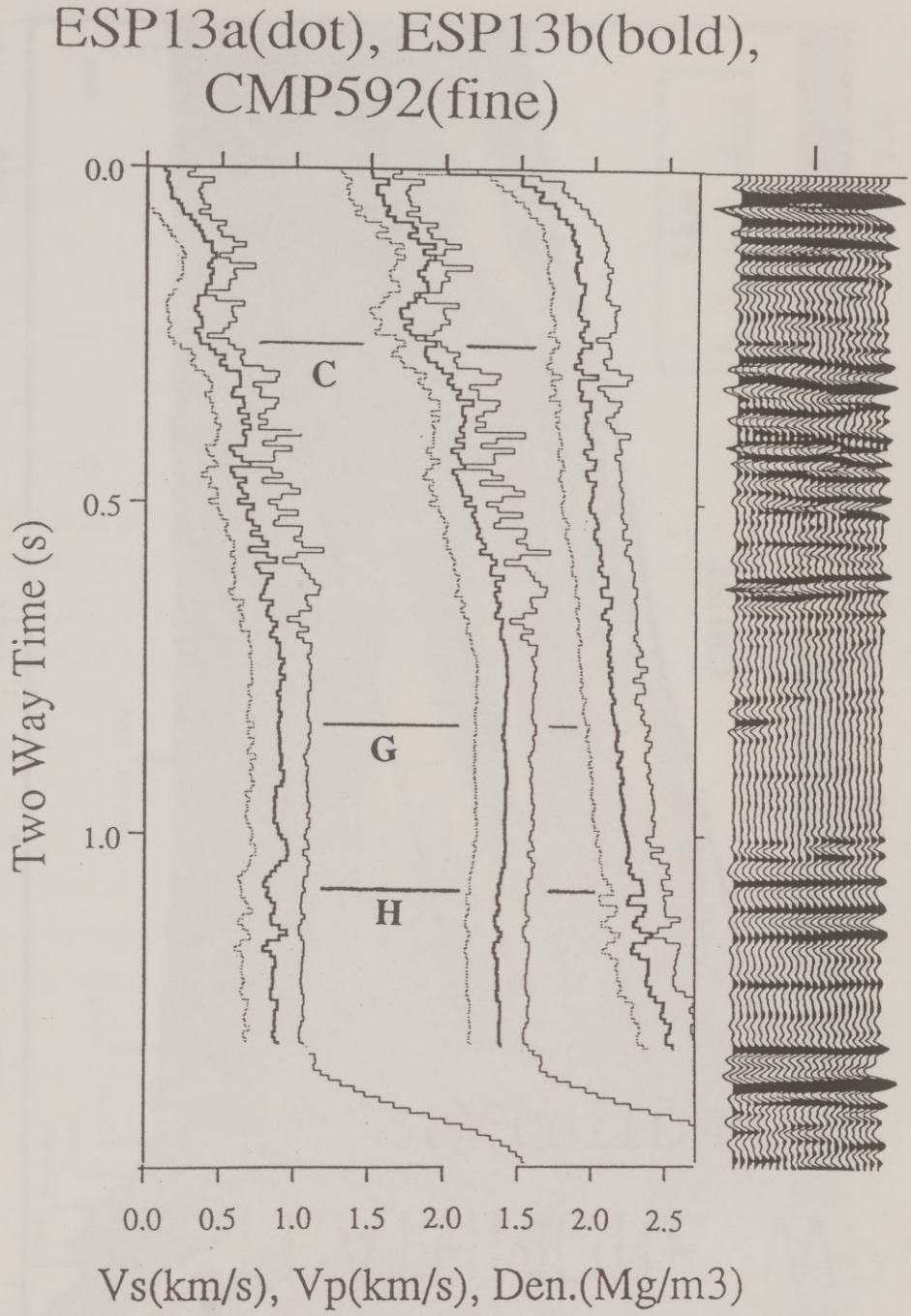

Figure 5.10. The results for ESP13a (dot, shifted left) and ESP13b (bold) are quite consistent. They both indicate a weaker reflectivity than do the results of the MCS data (fine, shifted right).

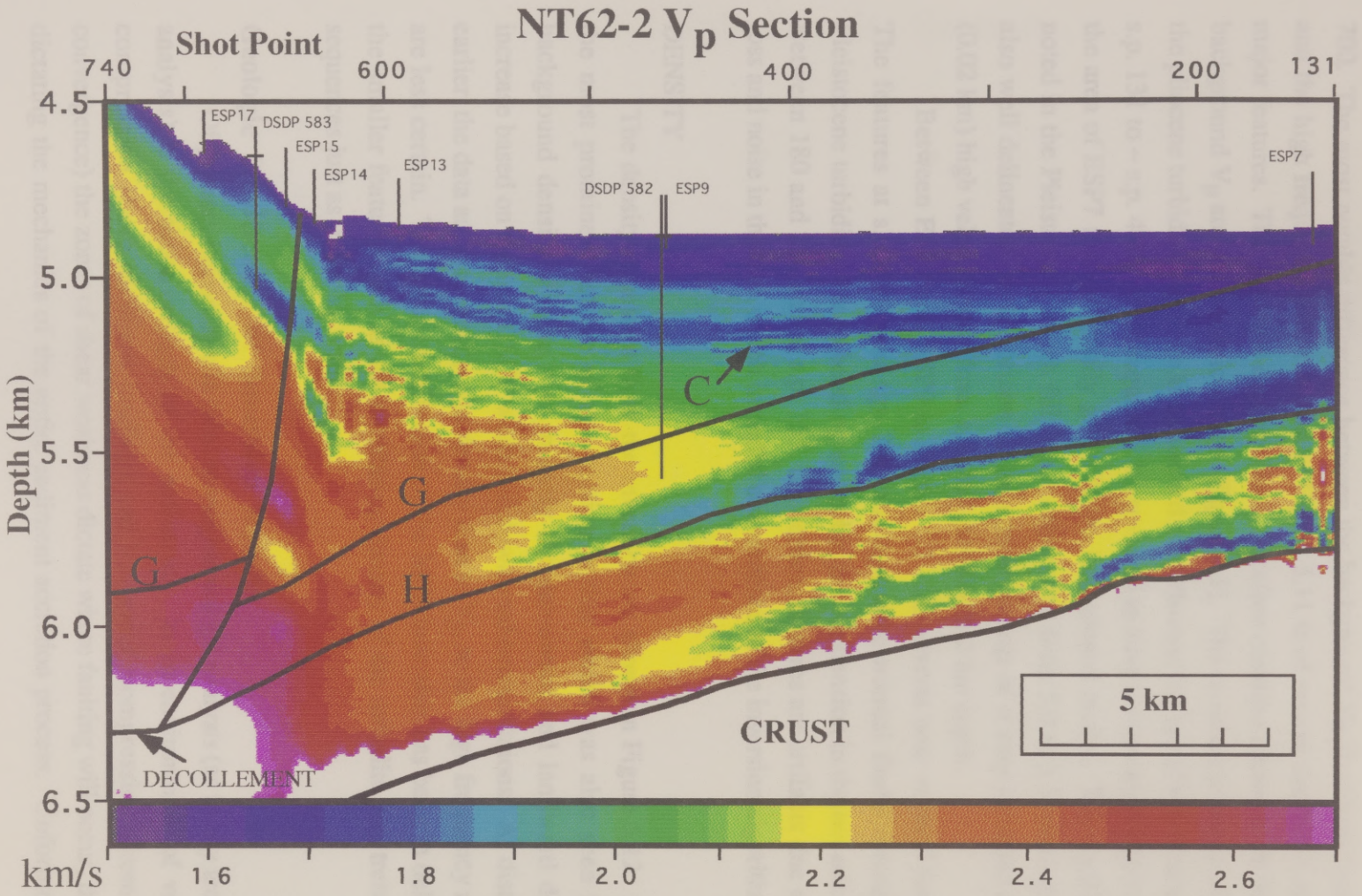

Figure 5.11. The V_p section compiled from inversion of every 5th full fold CMP shows much of the character of both the seismic data, (Figure 4.1) and background model, (Figure 4.3). Note the low V_p zone just above horizon H.

700. The most notable difference between the background V_p shown in Figure 4.3 and the high frequency result shown in Figure 5.11 is of course the detail of these major features. The structure depicted here therefore contains elements of both the background V_p and the seismic image (Figure 4.1). The oscillating nature of V_p in the pliocene turbidite sequence is delineated well, (lowest 0.5 km of the section from s.p. 131 to ~ s.p. 400). This sequence is estimated to have a somewhat higher V_p in the area of ESP7 than originally given in the background model. The oscillations noted in the Pleistocene trench fill (s.p. ~480 to 600 from 5.0 to 5.5 km depth) are also well delineated, as is horizon C, located at the top of a very continuous thin (0.02 km) high velocity zone from s.p. 260 to 600 at 5.2 km depth.

Between ESP7 and ESP9 in Figure 5.11 are several near vertical features. The features at s.p. 360 and s.p. 260 correspond to normal faults through the Pleistocene turbidites due to bending and subsequent extension in the oceanic crust. Between 180 and 230 and at s.p. 155, the vertical features are artifacts due to data loss and noise in the data which impeded convergence of the inversion algorithm.

DENSITY

The density estimates from the inversion are shown in Figure 5.12. Again the most prominent feature of this section is that which was also seen in the background density (Figure 4.4), namely the downward and landward density increase based on the two DSDP wells and downward extrapolations. As discussed earlier, the data are less sensitive to density than to V_p, so the high frequency results are less certain. The main contribution of the MCS inversion has been to delineate the smaller features such as the oscillating density of the turbidite and trench fill sequences just as in the V_p result.

Geologic Significance of Inversion Results

Of primary importance in this convergent margin analysis (as in any tectonic) analysis) is the shear strength of the sediments. In an environment of vertical compression (from sediment loading) and horizontal compression (from plate convergence) the zones of shear weakness dictate where faulting will occur, thereby dictating the mechanics of the entire sediment accretion process. Unfortunately,

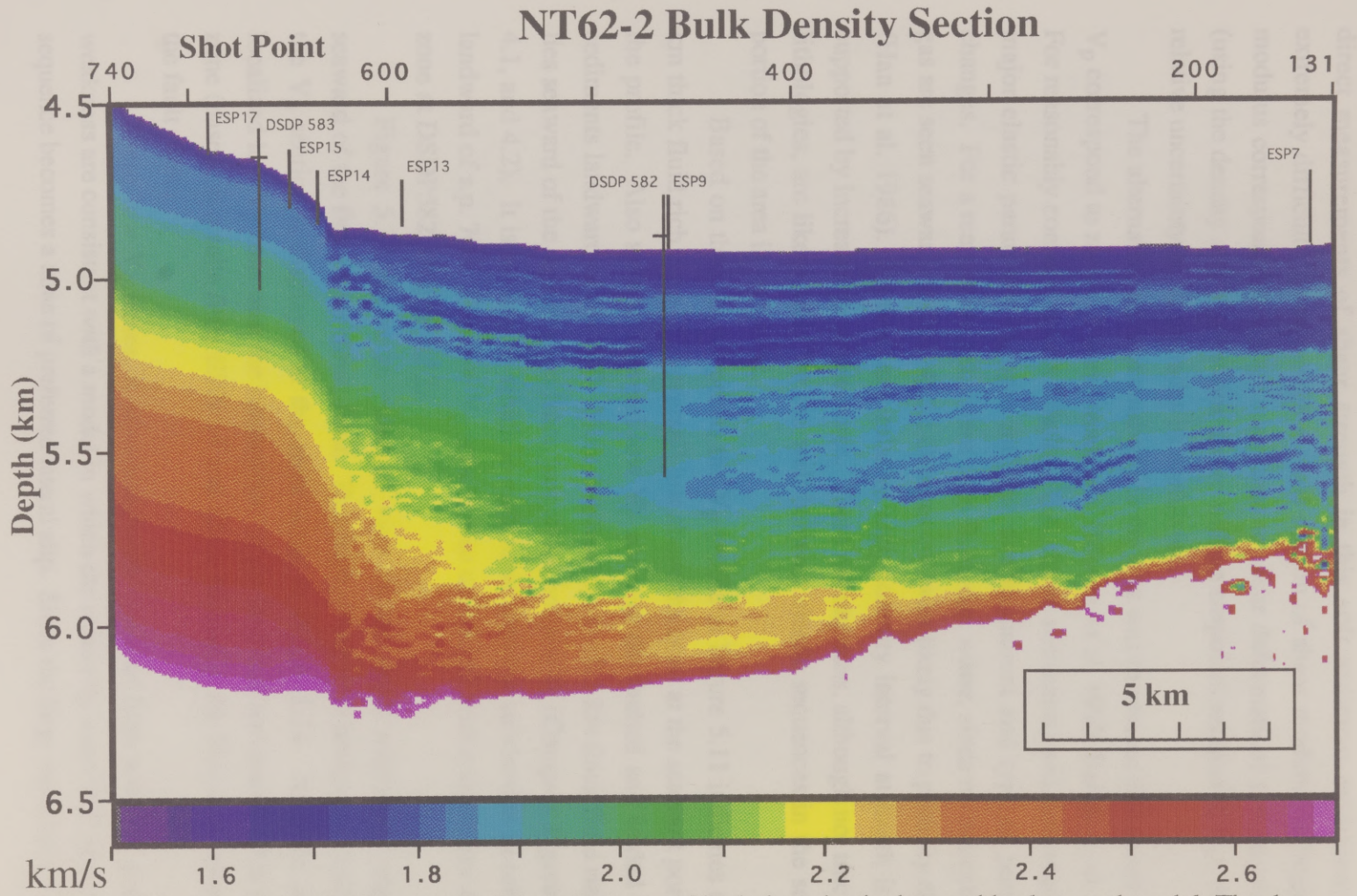

Figure 5.12. As with V_p the density result has character of both the seismic data and background model. The data are less sensitive to high frequency variations in density than to V_p so the result is not as certain.

direct measurements of shear strength in this soft sediment environment are extremely difficult. Even though a cross section of shear modulus (a large shear modulus corresponds to a large resistance to shear deformation) can be produced (using the density and V_p sections above with an empirical relation to V_s), the high relative uncertainty in V_s degrades its usefulness.

The alternative used extensively in the past was to assume that zones of low V_p correspond to zones of shear weakness, (Moore, et al. 1990, Bangs, et al. 1990). For reasonably constant matrix lithology (i.e. clastic sediments) and cementation the major elastic parameter changes must be due to amount and type of pore fluid changes. For a reasonably consistent pore fluid, (i.e. water, since no indications of gas are seen seaward of ESP14) the changes are most likely due to porosity changes (Han et al. 1986). Further, any relative high porosity interval at depth is likely supported by increased pore pressures. These assumptions, although not true for all lithologies, are likely valid for the well behaved clastic sequences in the seaward portion of the area investigated.

Based on these assumptions the V_p profile in Figure 5.11 indicates a ~ 0.1 km thick fluid rich zone (V_p reversal) just above the crust at the seaward portion of the profile. Also seen are several low Vp zones in the faulted and folded wedge sediments landward of s.p. 600. More importantly, a ~ 0.1 km thick fluid rich zone lies seaward of the deformation front, just above horizon H, (Compare Figures 5.11, 4.1, and 4.2). It is horizon H which is coincident with the subduction decollement landward of s.p. 700. This low V_p zone is also coincident with a slight low density zone at DSDP582, (Figure 5.12).

Figure 5.13 shows an enlarged view of the depth migrated image just seaward of the first major thrust fault. This fault, along with horizons G and H and the V_p section is displayed at the same scale in Figure 5.14. Note the intense, localized low V_p zone near the intersection of the fault and horizon G. This low V_p zone (based on results from ESPs 14 and 15) is located in the foot wall, seaward of the fault plane.

These low V_p zones, if associated with zones of high porosity and shear weakness are consistent with a model in which the relatively water rich hemipelagic sequence becomes a zone of preferred lateral slip. Since the large velocity reversal

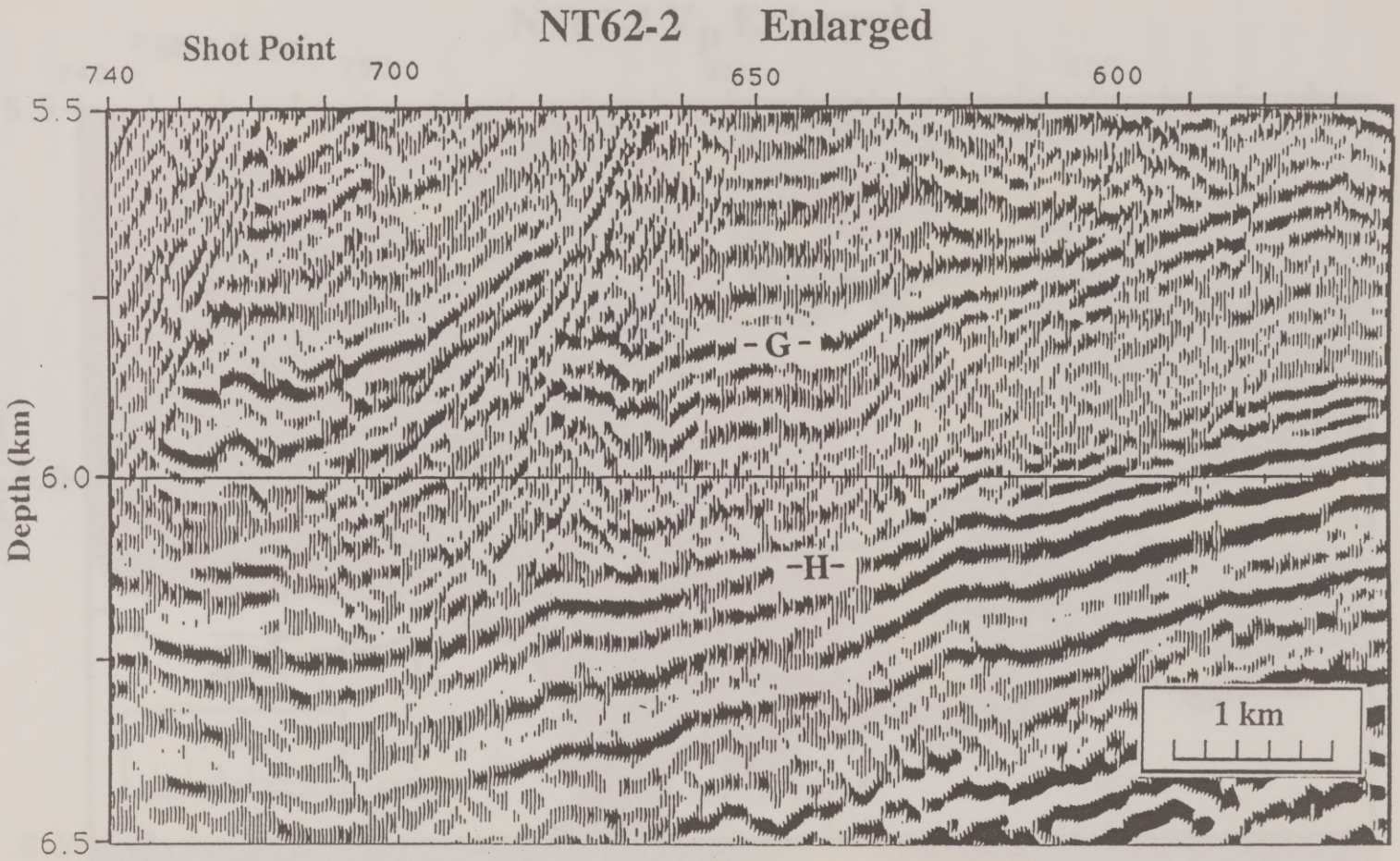

Figure 5.13. The portion of data between the deformation front and the first major thrust fault shows the continuity of reflections below, but not above horizon H.

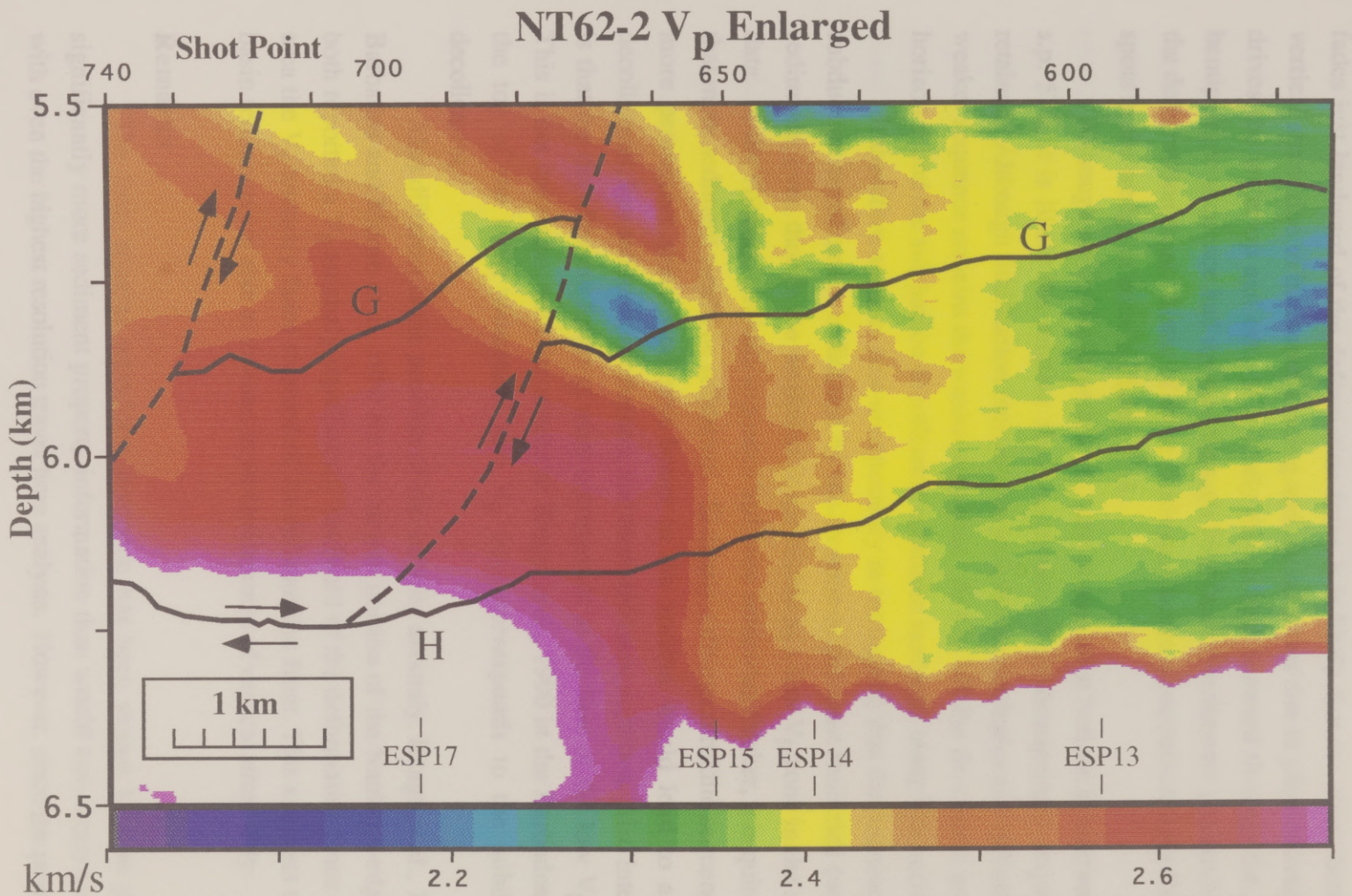

Figure 5.14. The enlarged V_p section shows the region just seaward of the first major thrust fault. Note the large increase in V_p from s.p. 600 to s.p. 660. Faults are shown as dashed lines.

fades just landward of the deformation front, it is likely that the stress here (both vertical stress due to increased loading and lateral stress due to plate convergence) drives the water up and out. It is likely driven both seaward through the porous hemipelagic sequence and upward through kink faulted sediments just landward of the deformation front. Some of these fluids may become trapped creating fluid rich spots in the wedge as seen in Figure 5.14.

Although no visible large low V_p zone is present at horizon H landward of ~ s.p. 570, it is likely the relative shear weakness of the hemipelagic sequence is retained. Although lithification increases in both the hemipelagics and turbidites, the weaker sequence remains the weaker sequence. At s.p. 700 the first thrust intersects horizon H and the subduction decollement continues landward along this horizon.

It therefore appears (not unexpectedly in retrospect) that the location of the subduction decollement is dictated by the location of the most fluid rich (weakest) sediments, even though the weakness is not visible as a low V_p zone in the seismic data. If the Pliocene turbidite sequence had been somewhat thicker, it is quite likely that more sediment would be subducted. Similarly a thinner turbidite sequence, or a more prominent shear weakness lower in the section would lead to a lower decollement, less sediment subduction, and more sediment accretion. Also interesting is that the decollement forms at what corresponds to the base of the low V_p zone. This is not consistent with the results of Bangs et al., 1990 in the Barbados where the top of the most prominent low V_p zone corresponds to the subduction decollement.

Also different is the position of the velocity anomaly. Bangs et al., 1990 in Barbados and Moore et al. 1990 for the eastern portion of the Nankai wedge have both reported a V_p anomaly significantly landward of the deformation front. In this area the V_p anomaly fades seaward of the deformation front. This suggests that the basin sediments are able to dewater in an enviornment of vertical stress only.

Remarks

The least squares waveform inversion has been shown here to provide significantly more sediment property information than would have been available with even the highest resolution travel time analysis. However, since the portions of

this study that were suitable for application of the 1-D inversion involved large features, (i.e. the 0.15 km thick low V_p zone), much of the information obtained was not directly applicable. Still, the inversion was helpful in delineating these features. Also, although the comparisons of the MCS and ESP data in Figures 5.9-5.11 showed similar results, the MCS data add to the analysis by providing continuity between the ESPs. The high impedance zone corresponding to horizon C for example, is faint in some ESPs and may have been disregarded as a spurious event.

In this particular study it was the ESPs which provided most of the useful sediment property information and most of that was in the form of the background V_p. It is unfortunate that the sediment shear strength here cannot be estimated directly, instead of relying on a chain of assumptions (albeit good assumptions) based on studies in other parts of the world. However the least squares algorithm described here provides a method by which future data sets may be analyzed for shear strength directly. Possibilities include the execution of a surface seismic experiment with extraordinary care, in which the far field source signature is known with at least an order of magnitude more certainty than is conventionally practiced, or an ocean bottom experiment in which shear waves are created and measured directly without relying on mode conversion.

Chapter 6
Conclusions

Effectiveness of the Least Squares Algorithm

As shown for several examples of synthetic and field data the least squares waveform inversion yields models which can effectively reproduce the seismic data. However as shown in Figure 2.9 even when the "observed" data are virtually noise free, and matched nearly perfectly, the correct model may not be recovered. Seismic data are simply less sensitive to some model parameters than to others. Although there is no simple, general way to represent this sensitivity (sensitivity will depend on the model) it can be estimated by analysis of the resolution matrix if the approximate model is known. Since this analysis can be performed prior to the acquisition of any data, it may be helpful in quantitatively determining the resolution of the experiment.

Other attributes of waveform inversion include a band limited sensitivity. The data are sensitive to changes in very low frequency changes in V_p (0.0 to 3 Hz when model parameters are parameterized as a function of travel time) which affect the arrival times of the reflection events. They are also sensitive to changes in all elastic parameters whose variation lies within the pass band of the data. Localized variations in time smaller than the shortest wavelength cannot be resolved in the presence of noise.

One important feature of the waveform inversion used in this study is the flexibility offered in data and model parameter weighting. For the Carolina Trough CMP1602 the signal to noise (both random and coherent) ratio was high compared to the Nankai Trough ESPs. The corresponding values for diag[C_D], (4.0 for CMP1602, and 4.0 to 16.0 for the ESPs) showed this difference. The quality of the background models (particularly Vp) were also different since the ESPs covered a significantly larger angle range, ~65° compared with ~55° for CMP1602. The values of the prior model covariance matrix (C_m) showed this difference. Therefore the inversion of the ESPs was influenced less by the data and more by the prior model than was the inversion of CMP1602. This feature ensures good performance of the algorithm on poor data with good prior models, or good data with poor prior models.

This balancing of model and data error not only offers flexibility but has a significant advantage over simply matching the data. As mentioned earlier the data may be very insensitive to some model parameters. With no model error these parameters are not constrained to take on geologically reasonable values.

Also important here is the fact that the problem is nearly linear, and the field data used here could have been modeled well with a single iterate. Although strictly linear elastic inversions may be much simpler than the iterative inverse Hessian scheme used here, it is important to have a more general capability which can accomodate a strictly non linear elastic problem. Failure to model the nonlinear effects may severely distort the inversion result.

Problems with Inversion of Field Data

Inherent in the acquisition of field seismic data are several effects which are typically ignored when computing synthetic seismograms. These effects can either be applied in the modeling or removed from the data. For example if the data contain static time shifts due to irregularities in the acquisition, these shifts can either be removed from the data or modeled as part of the forward problem. In this study I have tried to remove the irregularities in data acquisition from the data, making the modeling simpler and faster.

These irregularities include static time shifts from a slightly crooked, non horizontal streamer, and amplitude variations due to varying receiver sensitivity. There was also a directional dependence in the waveform amplitudes due to the source and receiver arrays. Using the water bottom multiple, the data were scaled so that reflection amplitudes matched reflectivity.

Since the data were decomposed into plane wave seismograms an additional data preparation effort was required. For this procedure the input x-t wavefield is assumed known over an infinite extent at the surface, (the PWD contains an infinite range offset integration). Since field data are always acquired with a finite aperture they must be smoothly tapered to avoid truncation artifacts in the integral transform. In order to accomplish this without losing data the wavefield is extrapolated to large offsets and only the extrapolated data are tapered. The x-t wavefield is also assumed

to have been acquired with point sources and receivers, but for the arrays used in this study this effect did not significantly alter the PWD.

Also removed from the data is the time delay of the water column. Applying a static elliptical shift to the data to make the water bottom reflection horizontal allows the analysis to work only on the target zone, improving the efficiency. Muting the data so that events from outside the zone of interest did not interfere was the last step in altering the form of the data to match the form of the synthetic seismograms used in the inversion algorithm.

Relevance of Results to Geology of Carolina and Nankai Troughs

The waveform inversion was applied actual field data from the Carolina and Nankai troughs and was able to accurately match the waveforms, but limitations of the data did kept the algorithm from recovering accurate estimates of all three independent elastic parameters. Still, the results were of significant use in answering some geologic questions. The results from the Carolina trough indicated the presence of a significant V_p decrease which creates the BSR in that area. The low V_p zone was very thin, (~0.025 km) and would have been missed by a travel time velocity analysis.

The results of from the large aperture ESPs showed many details that could not be otherwise seen and the MCS results provided a continuity to those details between the ESPs. These details include accurate delineation of a low V_p zone which represents an lithological sequence of low shear strength. Further landward the subduction decollement forms along this sequence.

Possibilities for Continuing Research

WAVELET ESTIMATION

Clearly the largest source of error, and therefore the limiting factor in the inversion of waveform data is error in estimating the source wavelet. Significant improvement in the resolution of elastic parameters will only be achieved when this error is reduced. Whether this is best achieved through deterministic methods (Ziolkowski et al. 1991), measurement of the far field wavelet with a dedicated

hydrophone, by the primary-multiple method of Stark (1986), or some other means is unknown.

Given this, there may be an easier way of determining C_D than the trial and error method used in this study. Including the source time function in the model vector would yield a least squares estimate of the wavelet consistent with the data and model. While this would not necessarily improve the resolution, it would ease the analysis and separate the wavelet error from other sources of error in the data.

COMPUTATIONAL SPEED

Assuming that a multi-iterate inversion is required, the computational speed of the algorithm may be increased substantially. The speed is limited partially by the calculation of the sensitivities but mostly by the $n_{mod} \times n_{mod}$ matrix (Hessian) inverse. In the time domain the Hessian matrix is sparse and the possibility exists of devising a fast matrix inverse which is an accurate approximation to the true inverse. Also, minimizing the number of model parameters would be helpful. This might be done using a different earth parameterization in which layer interfaces are placed only at reflection events above some prescribed amplitude.

These improvements could make some form of real time inversion practical. Although determining the parameters of the x-t preparation, (e.g. time window lengths, extrapolation distances, etc.) may be time consuming, once it is complete the actual preparation proceeds quickly. As presently coded, the acoustic inversion (faster due to one third fewer model parameters) can perform one Nankai MCS analysis from full fold x-t CMP gather to final inversion iteration in ~25 minutes on a SPARC 10™ workstation. A factor of ~60 improvement in either the hardware or software would enable on board acoustic inversion as the data are acquired. The advantage in performing the non linear inversion at each CMP is that one need not examine the data to ensure that it is linear before applying the algorithm.

NON-LINEAR PROBLEMS

The algorithm discussed in this study solves a linear or near linear problem quite well, and almost any problem is linear if one is close enough to the solution. However, getting this close is in general a non-linear problem. Combining the

linearized method described here with a fully non-linear method would negate the need for an accurate background trend prior to the inversion.

For the Carolina trough CMP1602 and the Nankai trough ESPs this non linear portion of the inversion was performed manually in the τ-p domain using an interactive travel time curve modeling. The τ-p trajectories of major events were modeled yielding an interval velocity between each pair of adjacent events. These were then smoothed and used as the starting V_p in the inversions, guaranteeing an accurate travel time match.

Another example of non-linear behavior occurs at large angles of incidence where reflection events are post critically reflected. These high amplitude events are prominent in any amplitude based error function and are very sensitive to the model parameters. A non-linear method applied here may converge better than a linear method.

MORE EXTENSIVE MODELING

A complete model of even a 1-D earth should certainly include anisotropy, and attenuation. These effects become more significant with increasing angle of incidence and are necessary if wide angle data are to be properly analyzed. Also, since interesting geology is rarely 1-D, an inversion using a multi-dimensional earth model would be a significant advance.

Remarks

The inversion algorithm discussed in this study performs exceptionally well, and is capable of recovering significant portions of V_p, density and V_s given a large enough signal to noise ratio. When applied to the data in this study the waveforms were well matched even though full model recovery was not achieved. Still, the results have enabled non invasive geologic analyses at extraordinarily high resolution compared to previous analyses in these areas.

APPENDIX

Data Processing sequences

The processing of each of the three data types was somewhat different. Figures A.1 through A.3 summarize in flow chart form the processing sequence described in the text. To the right of some steps is a reference to the pertinent Figure in the text.

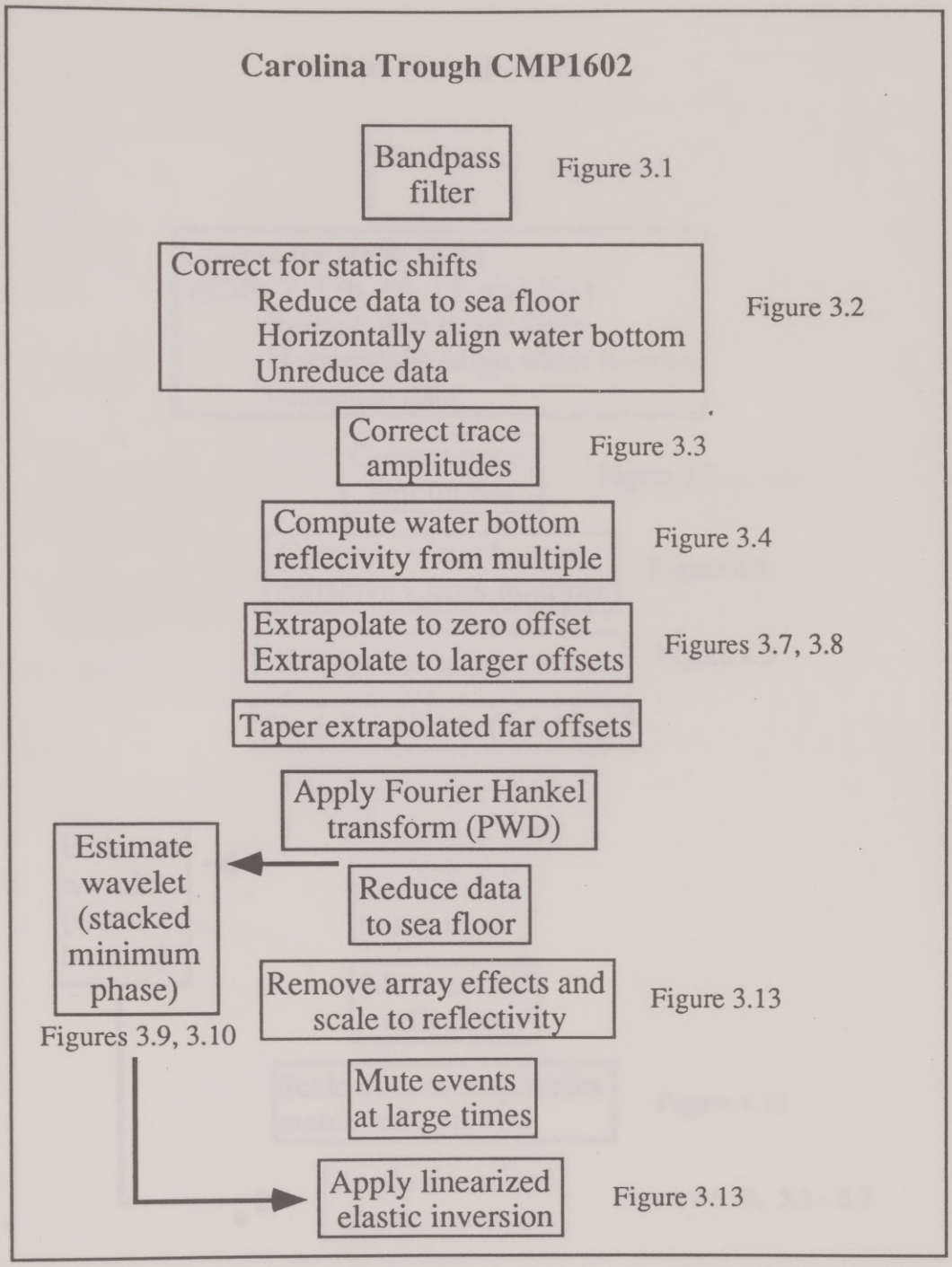

Figure A.1. The inversion algorithm described in this study requires as input plane wave data. Since data cannot be acquired in this domain they must be transformed after some corrections to compensate for non ideal acquisition geometry.

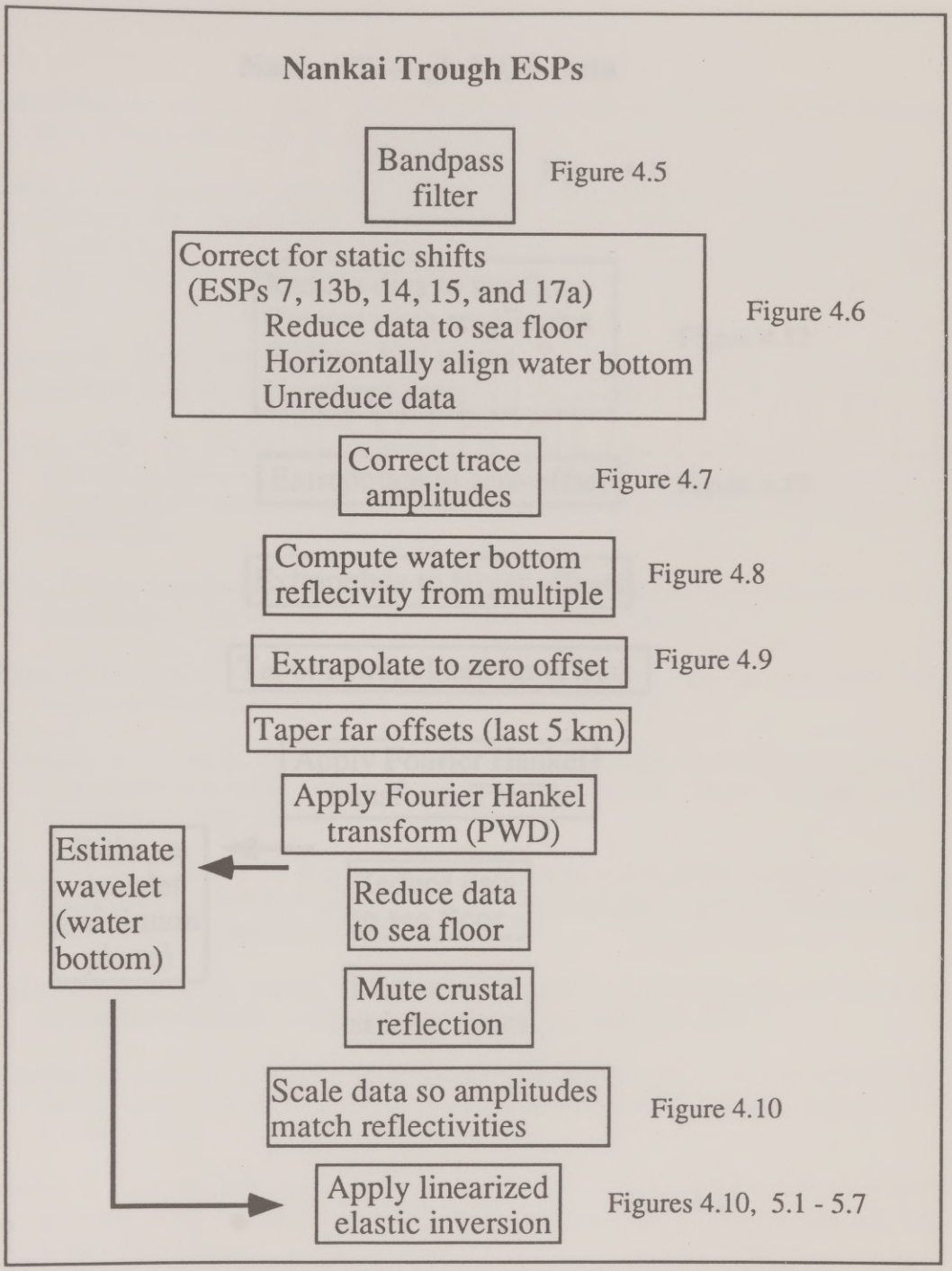

Figure A.2. The preparation of the ESPs was slightly different. No extrapolation to far offsets was performed and on ESPs 13a and 17b no statics corrections were applied.

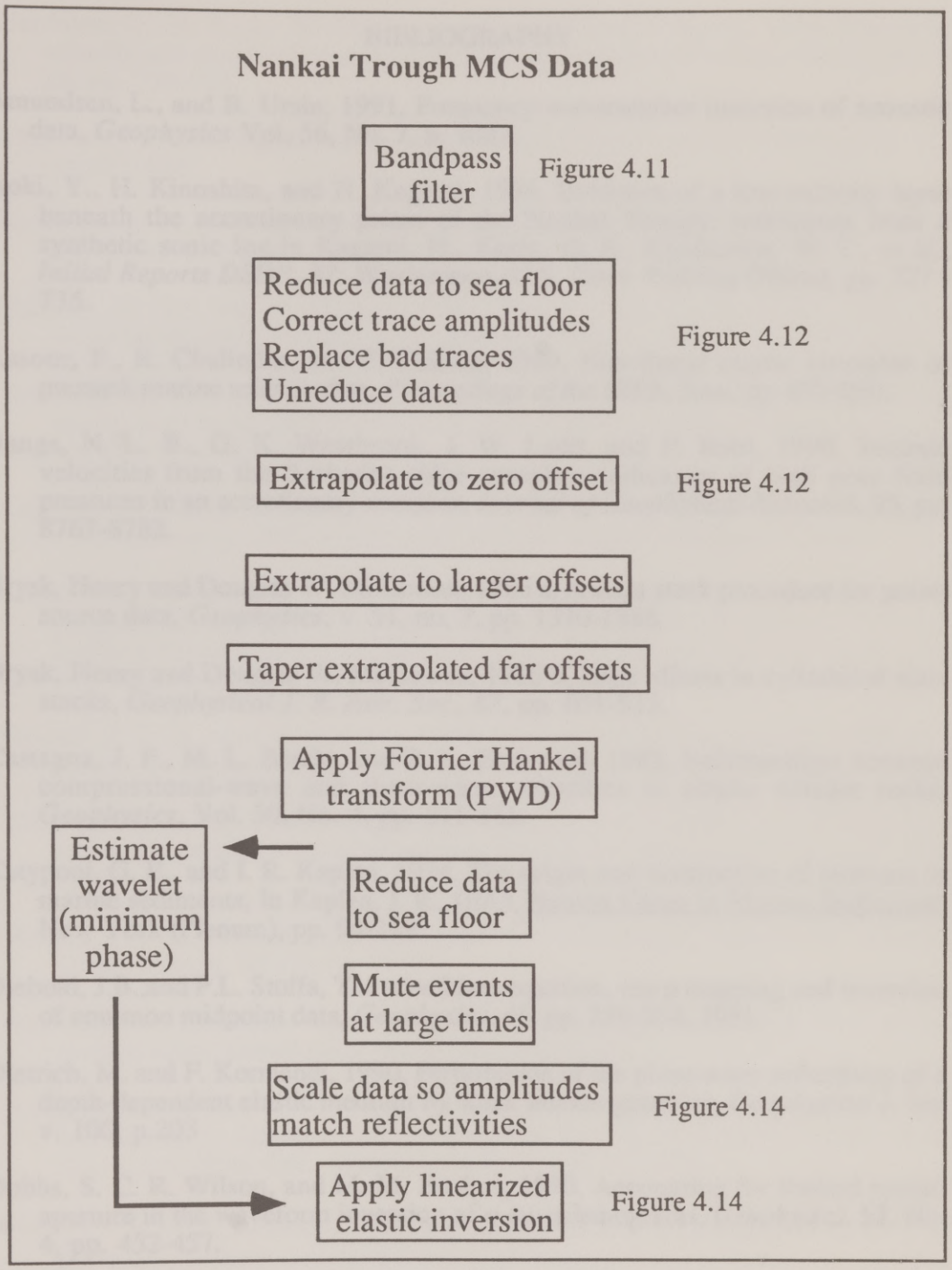

Figure A.3. The preparation of the Nankai MCS data were again slightly different. Statics corrections are not needed, and bad traces are replaced to insure continuous events.

BIBLIOGRAPHY

Amundsen, L., and B. Ursin, 1991, Frequency-wavenumber inversion of acoustic data, *Geophysics* Vol. 56, No. 7, p. 1027.

Aoki, Y., H. Kinoshita, and H. Kagami, 1986, Evidence of a low-velocity layer beneath the accretionary prism of the Nankai Trough: Inferences from a synthetic sonic log.In Kagami, H., Karig, D. E., Coulbourn, W. T., et al., *Initial Reports DSDP, 87*: Washington (U.S. Govt. Printing Office), pp. 727 - 735.

Assous, F., B. Chalindar, and F. Collino, 1989, Non-linear elastic inversion of prestack marine seismic data, *Proceedings of the IEEE*, June, pp. 877-890.

Bangs, N. L. B., G. K. Westbrook, J. W. Ladd, and P. Buhl, 1990, Seismic velocities from the Barbados ridge complex: indicators of high pore fluid pressures in an accretionary complex, *Journal of Geophysical Research*, 95, pp. 8767-8782.

Brysk, Henry and Douglas W. McCowan, 1986 a, A slant stack procedure for point-source data, *Geophysics*, v. 51, no. 7, pp. 1370-1386.

Brysk, Henry and Douglas W. McCowan, 1986 b, Edge effects in cylindrical slant stacks, *Geophysical J. R. Astr. Soc., 87*, pp. 801-813.

Castagna, J. P., M. L. Batzle, and R. L. Eastwood, 1985, Relationships between compressional-wave and shear-wave velocities in clastic silicate rocks, *Geophysics*, Vol. 50, No. 4, pp. 571-581.

Claypool, G. E., and I. R. Kaplan, 1974, The origin and distribution of methane in marine sediments, In Kaplan, I. R., (Ed.), Natural Gases in Marine Sediments: New York (Plenum), pp. 94-129.

Diebold, J.B.,and P.L. Stoffa, The traveltime equation, tau-p mapping and inversion of common midpoint data, *Geophysics*, *46*, pp. 239-254, 1981.

Dietrich, M. and F. Kormendi, 1990, Perturbation of the plane-wave reflectivity of a depth-dependent elastic medium by weak inhomogeneities, *Geophysical J. Int.* v. 100, p.203

Dobbs, S. C. R. Wilson, and M. M. Backus, 1990, Accounting for limited spatial aperture in the waveform inversion of p-tau seismograms, *Geophysics*, 55, No. 4, pp. 452-457.

Domenico, S. N., 1976, Effect of Brine gas mixture on velocity in an unconsolidated sand reservoir, *Geophysics* Vol. 41., No. 5, pp. 882-894

Gardener, G. H. F., L. W. Gardner, and A. R. and Gregory, 1974, Formation velocity and density-The diagnostic basis for stratigraphic traps, *Geophysics* V. 29, pp. 770-780.

Gassman, F., 1951, Elastic waves through a packing of spheres, *Geophysics*, v.15, pp.673-685.

Hamilton, E. L., 1976, Variations of density and porosity with depth in deep sea sediments. , J. *Sedimentary Petrology*, Vol. 46, No. 2, pp. 280-300.

Han, D., A. Nur, and D. Morgan, 1986, Effects of porosity and clay content on wave velocities in sandstones, *Geophysics*, Vol. 51, No. 11, pp. 2093-2107.

Hyndman, R. D., and G. D. Spence, 1992, Aseismic study of methane Hydrate marine bottom simulating reflectors, Journal of Geophysical Research, Vol. 97, No. B5, pp. 6683-6698.

Kagami, H., Karig, D. E., Coulbourn, W. T., et al., Initial Reports, Deep Sea Drilling Project, 1987, Washington (U.S. Government Printing Office)

Karig, D. E. 1987, The framework of deformation in the Nankai Trough, In Kagami, H., Karig, D. E., Coulbourn, W. T., et al., Initial Reports, Deep Sea Drilling Project, 1987, Washington (U.S. Government Printing Office), pp. 927-940.

Kennet, B. L. N., and N. J. Kerry, 1979, Seismic waves in a stratified half-space, *Geoph. J. Roy. Astr. Soc.*, V. 57, pp. 557-583.

Kvenvolden, K. A., 1984, Comparison of marine gas hydrates in sediments of an active and passive continental margin, *Marine and Petroleum Geology*, V. 2, pp. 65-71.

McAulay, A. D., 1985, Pre-stack inversion with plane-layer point source modeling, *Geophysics*, v. 50 (1), pp. 77-89.

McAulay, A. D., 1986, Plane layer prestack inversion in the presence of surface reverberation, *Geophysics*, V. 51, pp. 1789-1800.

Mathews, M. A. and R. von Huene, 1985, Site 570 methane hydrate zone, In R. von Huene, J. Aubouin et al., (Ed.s), Init. Rep. Deep Sea Drill. Proj., V. 84, U.S. Govt. Print. Off., Washington, D.C., pp. 773-790.

Menke, W., 1989, Geophysical data analysis: discrete inverse theory, Acedemic Press Inc.

Moore, G. F., T. H. Shipley, P.L. Stoffa, D. E. Karig, A. Taira, S. Kuramoto, H. Tokuyama, and K. Suyehiro, 1990, Structure of the Nankai Trough

accretionary zone from multichannel seismic reflection data, *Journal of Geophysical Research* 95, pp. 8753-8765.

Mora P.,1988, Elastic wave-field inversion of reflection and transmission data, *Geophysics*, v. 53, no. 6, pp.750-759.

Mora P.,1986, Elastic inversion of seismic data for P-wave velocity, S-wave velocity and density, in Shear Wave Exploration, Society of Exploration Geophysicists monograph series.

Porsani, Milton J., 1992, Efficient solution of covariance equations with applications to seismic trace extrapolation and predictive deconvolution, Proc. 62nd Annual Int. Society of Exploration Geophysicists Meeting, Atlanta, GA., pp. 1191-1194.

Sheriff, R. E. and L. P. Geldart, 1986, Exploration seismology Volume 1: History, theory, and data acquisition, Cambridge University Press.

Shipley, T. H., and B. M. Didyk, 1982, Occurrence of methane hydrates offshore southern Mexico, In J. S. Watkins, J.C. Moore, et al. (Ed.s), Init. Rep. Deep Sea Drill. Proj., V. 66, U.S. Govt. Print. Off., Washington, D.C., pp. 547-555.

Smith, G. C., and P. M. Gidlow, 1987, Weighted stacking for rock property estimation and detection of gas, Geophysical Prospecting, Vol. 35, pp. 993-1014.

Stark, T. J., 1986, Information from Deep Water Seismic Reflection Data: LASE Line 2, Ph.D. Dissertation, The University of Texas at Austin.

Stoffa, P. L. and M. K. Sen, 1991, Nonlinear multiparameter optimization using genetic algorithms: inversion of plane wave seismograms, *Geophysics*, Vol. 56, No. 11, p. 1794.

Stoffa, P. L., W. T. Wood, T. H. Shipley, G. F. Moore, E. Nishiyama, M. A. B. Botelho, A. Taira, H. Tokuyama, and K. Suyehiro, 1992, Deep water high resolution expanding spread and split spread marine seismic profiles in the Nankai Trough, *Journal of Geophysical Research* Vol. 97, No. B2, p.1687.

Taira, A., I.A. Hill, J. Firth et al., Proceedings ODP, *Initial Reports*, *131*, College Station, TX.

Tarantola, A., 1987, Inverse problem theory: methods for data fitting and model parameter estimation, Elsevier, New York.

Wang, David Y., 1990, Analysis of factors controlling the resolution of P-wave velocity and density in linearized least squares inversion, Ph.D. Dissertation, The University of Texas at Austin.

Wood, W. T., 1989, One and two dimensional seismic velocity inversion in the domain of intercept time and ray parameter: an example in the Nankai Trough, Master Thesis University of Texas.

Wylie, M. R. M., Gregory, A. R., and Gardner, L. W., 1956, Elastic wave velocities in heterogeneous and porous media, *Geophysics*, Vol. 21, pp 41-70.

Yilmaz, O., 1987, Seismic data processing, Society of Exploration Geophysics Investigations in Geophysics No. 2.

Ziolkowski, A., G. Parkes, L. Hatton, and T. Haugland, 1982, The signature of an air gun array: Computation from near-field measurement including interactions, *Geophysics*, Vol. 47, No. 10.

Ziolkowski, A., Why don't we measure seismic signatures ?, *Geophysics*, Vol. 56, No. 2, pp. 190-201.

The vita has been removed from the digitized version of this document.